International Journal of Rock Mechanics & Mining Sciences 151 (2022) 105007



Contents lists available at ScienceDirect

International Journal of Rock Mechanics and Mining Sciences

journal homepage: www.elsevier.com/locate/ijrmms





A reinvestigation into Munson's model for room closure in bedded rock salt

Benjamin Reedlunn [a,*], J. Guadalupe Argüello [b], Frank D. Hansen [c]

[a] Sandia National Laboratories, P.O. Box 5800, Albuquerque, NM, 87185, USA
[b] 8328 S. Sandoval Ct. NE, Albuquerque, NM, 87122, USA
[c] 3005 La Villita Pl. NE, Albuquerque, NM, 87111, USA

ARTICLE INFO

Keywords:
Bedded rock salt
Creep
Viscoplasticity
Room closure
Waste Isolation Pilot Plant

ABSTRACT

Accurate predictions of room closure are important for hazardous waste repositories in rock salt formations, such as the Waste Isolation Pilot Plant (WIPP). When Munson and co-workers simulated several room closure experiments conducted at the WIPP during the 1980's and 1990's, their simulated closure curves closely agreed with the closure measurements. A careful review of their work, however, raised concerns and prompted the reinvestigation in this paper. To begin the reinvestigation, Munson's legacy Room D closure simulation was reasonably recreated in a current-day finite element code. Next, special care was taken to obtain numerically converged results, re-introduce the anhydrite strata intermittently ignored by Munson, and calibrate the Munson–Dawson (M–D) constitutive model for salt as much as possible from laboratory test measurements. When this new model was used to simulate Room D's closure, it under-predicted the horizontal and vertical closure rates by 2.34× and 3.10×, respectively, at 5.7 years after room excavation. As a result, the M–D model was extended to capture the newly established creep behavior at low equivalent stresses (< 8 MPa) and replace the Tresca with the Hosford equivalent stress. Simulations using the new M–D model over-predicted the horizontal closure rate by 1.15× and under-predicted the vertical closure rate by 1.08× at 5.7 years, averaged over three room closure experiments. Although further improvements could be made, the new model has a stronger scientific foundation than Munson's legacy model and appears ready for careful engineering use.

1. Introduction

Geomechanical simulations are essential for the long-term assessment, operation, and design of nuclear or hazardous waste repositories in rock salt formations, such as the Waste Isolation Pilot Plant (WIPP) in southeastern New Mexico, USA. The mining of the repository, coupled with the weight of the overburden, causes deviatoric stresses in the salt surrounding drifts within the repository. These deviatoric stresses lead to cracks in the excavation damaged zone (EDZ) near drifts, where the confining pressure is low, but the deviatoric stresses also lead to viscoplasticity (creep) near *and* far away from drifts. The viscoplasticity causes drifts to gradually close over the course of several decades, which compacts any nuclear or hazardous waste stored in the drift until the waste supplies sufficient back pressure to resist the weight of the overburden. The back pressure can also cause the EDZ cracks to close and heal, helping to further isolate the waste from the biosphere. Simulations of these processes can help predict the long-term performance of the repository. Simulations also provide short-term predictions that are valuable to the operation and design of salt repositories. For example, operations personnel need to know how long they can operate in an area before it becomes unsafe. Models that include a damage and/or fracture criterion can help predict when a slab of salt might detach from the roof and fall to the floor. As another example, repository operators may wish to seal off a section of the repository. Many seal designs rely on drift closure to compress the seal, so simulations can help predict the seal maturation time. As one further example, engineers must consider operational efficiency, worker safety, environmental impact, costs, and many other factors when they lay out a repository design. Simulations of the underground evolution can be quite helpful to select between various design concepts. For these reasons, it is important to develop and validate geomechanical modeling tools.

Sandia National Laboratories, a contractor for the United States government, recognized the value of geomechanical modeling in the early days of the WIPP project. In the 1970's and 1980's, Sandia developed geomechanical models of drift closure and compared their model predictions against underground experiments at the WIPP, such as the Room D, B, G, and Q closure experiments. The initial room closure models produced unsatisfactory predictions,[1–5] so Munson et al.[6] substantially altered their model to resolve discrepancies between the simulated and measured Room D closure histories. Munson and co-workers later used variations of their Room D model to simulate

* Corresponding author.
E-mail address: breedlu@sandia.gov (B. Reedlunn).

https://doi.org/10.1016/j.ijrmms.2021.105007
Received 23 June 2021; Received in revised form 30 September 2021; Accepted 29 November 2021
Available online 21 January 2022
1365-1609/© 2022 Elsevier Ltd. All rights reserved.

several other WIPP room closure experiments (see Ref. 7 and references therein).

Interest in the Room D and B experiments was recently rekindled by two independent studies. (Room B was nearly identical to Room D, except heaters were installed in the floor to simulate heat generating waste.) The first study was part of a German and American (United States) collaboration titled, Joint Project III on the Comparison of Constitutive Models for the Mechanical Behavior of Rock Salt.[8] The second study was performed by the Southwest Research Institute (SwRI) under contract with the United States Nuclear Regulatory Commission (NRC).[9–11] Sandia was intimately involved in Joint Project III, but did not directly contribute to the SwRI study.

The Joint Project III Room D and B study was a model benchmarking exercise that included an extensive set of new laboratory experiments on WIPP salt, calibration of eight constitutive models against these experiments, and comparisons of closure predictions against Room D and B's measured closure.[8,12] The Joint Project III model of Room D and B was similar to Munson's model, but it was not identical. For example, the Joint Project III model did not include sliding at the clay seams between the bedded salt strata. Sandia began this benchmarking exercise by re-creating the legacy simulations of Room D and B[13,14] using the Munson–Dawson salt constitutive model calibration laid out in Ref. 6. (The Munson–Dawson model is also known as the M–D or Multi-mechanism Deformation model.) Once Sandia recalibrated the M–D model against the new laboratory experiments, however, inconsistencies were discovered, prompting a review of the modeling approach reported in Refs. 6, 7. As will be discussed in Sections 2.2.3 and 2.2.4, the review raised significant concerns and motivated the in-depth reinvestigation in this paper.

The SwRI study was primarily aimed at implementing and extending the FZK-INE constitutive model for salt[15] in order to investigate the geomechanical behavior of generic salt repositories. The Room D and B simulations were utilized as a way to demonstrate and validate the model. Once implemented, Ofoegbu and Dasgupta[9] calibrated the FZK-INE creep response against a selection of older tests on WIPP salt.[16] This calibration, rather unconventionally, set the steady-state creep rates to very low, almost negligible, values and captured the laboratory measured creep behavior almost exclusively with the model's transient creep response. When they simulated Room D with this model, the predicted horizontal and vertical closures stopped evolving after about 1 yr[9, Fig. 3–5]. By contrast, the measured Room D horizontal and vertical closures continued to evolve after 1 yr at substantial rates of 45 mm/yr and 59 mm/yr, respectively (see Fig. 5). The follow-up report[10] used these discrepancies to motivate adding damage (micro-fracturing) to the FZK-INE model with a dilatational, time-independent, plasticity formulation. Finally, Ofoegbu and Dasgupta[10,11] varied the transient creep, plasticity, and other parameters to match the closure of Room D.

The approach pursued herein differs from the Joint Project III and SwRI studies in several ways.

1. Rather than start with a completely new model setup, this paper starts with the historical Munson et al.[6] model setup and gradually improves upon it.
2. This study pays special attention to characterizing and minimizing numerical approximations, as one cannot accurately assess prediction error if it is polluted by numerical error.
3. The M–D model calibration does not neglect steady-state creep, in accordance with the other constitutive model calibrations in Joint Project III and much of the salt mechanics community.
4. Unlike the other constitutive models, the M–D model does not include damage. An extension of the M–D model, the Munson–Dawson–Chan–Fossum (M–D–C–F) model[17] includes damage, but the goal of this paper is to reinvestigate the simulations in Refs. 6, 7, which utilized the M–D model, not the M–D–C–F model. Furthermore, it seems prudent to make the best model prediction possible before adding the complexities that go along with damage.
5. Rather than vary model parameters to match underground test measurements, this study and the Joint Project III study attempts to predict room closure as much as possible from laboratory test measurements. Constitutive modelers usually have greater insight about which parameters should be adjusted to capture laboratory tests, as laboratory tests are typically simpler, more tightly controlled, and more precisely measured than large-scale underground tests.

Thus, the study pursued herein diverges somewhat from the Joint Project III study and more significantly from the SwRI study.

The remainder of this paper is organized as follows. Section 2 presents background on Munson's room closure model, Section 3 covers the reinvestigation of the room closure model, and Section 4 summarizes the findings.

2. Background

Sandia expended significant resources to simulate WIPP room closure during the 1970's, 1980's, and 1990's. A comprehensive review is beyond the scope of this paper, but the interested reader is referred to Refs. 18–20 for summaries of the work performed during those decades. Instead, we focus on the M–D constitutive model in Section 2.1 and the development of Munson's room closure model in Section 2.2.

2.1. Munson–Dawson constitutive model

The M–D model is a hypoelastic, isotropic, viscoplastic (creep) constitutive model for the damage-free, thermomechanical, behavior of rock salt.[6,21–23] It is relatively well known in the salt mechanics community, and fairly simple to calibrate against damage-free creep (constant stress) experiments. The model does not include a (static) yield surface and viscoplastic strain accumulates, albeit slowly, even at very low stresses.

2.1.1. Formulation

This section presents the M–D model mathematical formulation discussed in Ref. 23. As is common in the geomechanics literature, compressive strains and stresses are treated as positive.

The M–D model decomposes the total strain rate $\dot{\boldsymbol{\varepsilon}}$ into an elastic strain rate $\dot{\boldsymbol{\varepsilon}}^{\mathrm{el}}$, a thermal strain rate $\dot{\boldsymbol{\varepsilon}}^{\mathrm{th}}$, and a viscoplastic strain rate $\dot{\boldsymbol{\varepsilon}}^{\mathrm{vp}}$:

$$\dot{\boldsymbol{\varepsilon}} = \dot{\boldsymbol{\varepsilon}}^{\mathrm{el}} + \dot{\boldsymbol{\varepsilon}}^{\mathrm{th}} + \dot{\boldsymbol{\varepsilon}}^{\mathrm{vp}}. \tag{1}$$

The elastic behavior utilizes generalized Hooke's law in rate form to relate the elastic strain rate $\dot{\boldsymbol{\varepsilon}}^{\mathrm{el}}$ and the stress rate $\dot{\boldsymbol{\sigma}}$,

$$\dot{\boldsymbol{\sigma}} = \boldsymbol{C} : \dot{\boldsymbol{\varepsilon}}^{\mathrm{el}} = \boldsymbol{C} : \left(\dot{\boldsymbol{\varepsilon}} - \dot{\boldsymbol{\varepsilon}}^{\mathrm{th}} - \dot{\boldsymbol{\varepsilon}}^{\mathrm{vp}}\right) \tag{2}$$

$$\boldsymbol{C} = (B - 2/3\,G)\,\boldsymbol{I} \otimes \boldsymbol{I} + 2\,G\,\boldsymbol{\mathcal{I}}, \tag{3}$$

where $\boldsymbol{C}$ is the fourth-order elastic stiffness tensor composed of the bulk modulus B, the shear modulus G, the second-order identity tensor $\boldsymbol{I}$, and the fourth-order symmetric identity tensor $\boldsymbol{\mathcal{I}}$. The thermal strain portion of the model is simply

$$\dot{\boldsymbol{\varepsilon}}^{\mathrm{th}} = -\alpha\,\dot{T}\,\boldsymbol{I} \tag{4}$$

where α is the coefficient of thermal expansion, and T is the absolute temperature.

Viscoplastic deformation of damage-free salt is isochoric and only occurs in the presence of shear stress. Originally, the MD model utilized the von Mises stress as its equivalent shear stress measure $\bar{\sigma}$, but Munson et al.[6] switched $\bar{\sigma}$ to the Tresca stress. Reedlunn[23] changed it again to an equivalent stress measure proposed by Hosford[24]:

$$\bar{\sigma} = \left\{ \frac{1}{2} \left[|\sigma_1 - \sigma_2|^a + |\sigma_2 - \sigma_3|^a + |\sigma_1 - \sigma_3|^a \right] \right\}^{1/a}, \tag{5}$$

where σ_i are the principal stresses and a is a material parameter. As shown in Appendix A of Reedlunn[23], Eq. (5) encompasses the Tresca stress $\bar{\sigma}_{\text{tc}}$ when $a = 1$, the von Mises stress $\bar{\sigma}_{\text{vm}}$ when $a = 2$, and a range of behaviors in-between ($1 < a < 2$). One can also reproduce $\bar{\sigma}_{\text{tc}}$ with $a = \infty$, $\bar{\sigma}_{\text{vm}}$ with $a = 4$, and behaviors in-between with $4 < a < \infty$. This second range avoids a potential singularity in the second derivative of Eq. (5) (see Section 2.1 in Ref. 25 or Appendix B.1.2 of Ref. 23), which is required for implicit (backward Euler) numerical integration schemes, so the exponent is restricted to $a \geq 4$ herein. Besides the added flexibility of the exponent a, the continuous nature of $\partial\bar{\sigma}/\partial\boldsymbol{\sigma}$, compared to $\partial\bar{\sigma}_{\text{tc}}/\partial\boldsymbol{\sigma}$, makes the model's numerical implementation simpler and probably more robust.

The viscoplastic strain evolves according to an associated flow rule

$$\dot{\boldsymbol{\varepsilon}}^{\text{vp}} = \dot{\bar{\varepsilon}}^{\text{vp}} \frac{\partial\bar{\sigma}}{\partial\boldsymbol{\sigma}}, \tag{6}$$

where the equivalent stress $\bar{\sigma}$ is also the flow potential, $\partial\bar{\sigma}/\partial\boldsymbol{\sigma} = \boldsymbol{n}$ is the normal to the flow potential, and $\dot{\bar{\varepsilon}}^{\text{vp}}$ is the equivalent viscoplastic strain rate. The flow potential normal in the principal frame is

$$\boldsymbol{n} = \sum_{i=1}^{3} \frac{\partial\bar{\sigma}}{\partial\sigma_i} \tilde{\boldsymbol{e}}_i \otimes \tilde{\boldsymbol{e}}_i \tag{7}$$

where $\tilde{\boldsymbol{e}}_i$ are the principal stress directions.[1] See Appendix B.1.1 of Ref. 23 for numerically tractable expressions for $\partial\bar{\sigma}/\partial\sigma_i$ when $a \gg 1$. The equivalent viscoplastic strain rate can be decomposed into two components

$$\dot{\bar{\varepsilon}}^{\text{vp}} = \dot{\bar{\varepsilon}}^{\text{tr}} + \dot{\bar{\varepsilon}}^{\text{ss}}, \tag{8}$$

where $\dot{\bar{\varepsilon}}^{\text{tr}}$ is the transient equivalent viscoplastic strain rate and $\dot{\bar{\varepsilon}}^{\text{ss}}$ is the steady state equivalent viscoplastic strain rate.

The original MD model additively decomposed the steady state behavior into three mechanisms. Recent investigations on WIPP rock salt, however, have reported greater steady-state creep rates at $\bar{\sigma} < 8$ MPa than would be expected from extrapolating rates from higher stresses.[26–28] Thus, Reedlunn[23] added a fourth mechanism, Mechanism 0, to capture the steady-state creep at low equivalent stresses. The new expression for steady state creep is

$$\dot{\bar{\varepsilon}}^{\text{ss}} = \sum_{i=0}^{3} \dot{\bar{\varepsilon}}_i^{\text{ss}} \tag{9}$$

$$\dot{\bar{\varepsilon}}_i^{\text{ss}} = A_i \exp\left(-\frac{Q_i}{RT}\right) \left(\frac{\bar{\sigma}}{G}\right)^{n_i} \quad \text{for } i = 0,\ 1,\ \text{and } 2 \tag{10}$$

$$\dot{\bar{\varepsilon}}_3^{\text{ss}} = H(\bar{\sigma} - \bar{\sigma}_{\text{g}}) \sum_{i=0}^{2} B_i \exp\left(-\frac{Q_i}{RT}\right) \sinh\left[q\frac{(\bar{\sigma} - \bar{\sigma}_{\text{g}})}{G}\right], \tag{11}$$

where the variables A_i, B_i, Q_i, n_i, $\bar{\sigma}_{\text{g}}$, and q are all model parameters. All four mechanisms have an Arrhenius temperature dependence, where each Q_i is an activation energy and $R = 8.314$ J/(K mol) is the universal gas constant. Mechanism 0 is given the same mathematical form as Mechanisms 1 and 2, a Norton–Hoff creep relation, since it captures the low stress creep behavior observed in Refs. 26–28. The actual micro-mechanical mechanism behind the Mechanism 0 behavior is likely pressure solution redeposition along grain boundaries, based on an observed stress exponent of ≈ 1, an inverse correlation with grain size, and an absence of these effects in extremely dry samples (< 5 ppm water content) of synthetic and natural rock salt.[29–33] Mechanism 1, on the other hand, dominates at high temperatures and low equivalent stresses, where the creep strain rate is limited by the time required for dislocations to climb over microstructural obstacles. Mechanism 2 dominates at low temperatures and medium equivalent stresses. The micro-mechanical cause for mechanism 2 is uncertain, but cross-slip is a likely candidate.[34] Regardless of the cause, the macroscopic behavior corresponding to the second mechanism has been well characterized. Mechanism 3 models dislocation glide, which is only activated when $\bar{\sigma}$ exceeds $\bar{\sigma}_{\text{g}}$, as reflected in the heaviside function $H(\bar{\sigma} - \bar{\sigma}_{\text{g}})$. Typically, the parameters B_i are chosen to produce a smooth transition from mechanisms 0, 1, and 2 to mechanism 3 at $\bar{\sigma}_{\text{g}}$.

The simple functional forms of Eqs. (10) and (11) suffice for the steady-state behavior, but the transient behavior is more complex. During work hardening under constant stress, $\bar{\varepsilon}^{\text{tr}}$ approaches the transient equivalent strain limit $\bar{\varepsilon}^{\text{tr}^*}$ from below, and the total viscoplastic strain rate slows down over time. During recovery under constant stress, $\bar{\varepsilon}^{\text{tr}}$ approaches $\bar{\varepsilon}^{\text{tr}^*}$ from above, and the total viscoplastic strain rate speeds up over time. The rate that $\bar{\varepsilon}^{\text{tr}}$ approaches $\bar{\varepsilon}^{\text{tr}^*}$ is governed by

$$\dot{\bar{\varepsilon}}^{\text{tr}} = (F - 1)\ \dot{\bar{\varepsilon}}^{\text{ss}}, \tag{12}$$

where

$$F = \exp\left[\text{sign}(\bar{\varepsilon}^{\text{tr}^*} - \bar{\varepsilon}^{\text{tr}})\,\kappa \left(1 - \frac{\bar{\varepsilon}^{\text{tr}}}{\bar{\varepsilon}^{\text{tr}^*}}\right)^2\right]. \tag{13}$$

The quantity κ depends on whether the material is work hardening or recovering:

$$\kappa = \begin{cases} \kappa_{\text{h}} = \alpha_{\text{h}} + \beta_{\text{h}} \log_{10}\left(\dfrac{\bar{\sigma}}{G}\right) & \text{for} \quad \bar{\varepsilon}^{\text{tr}} \leq \bar{\varepsilon}^{\text{tr}^*} \\ \kappa_{\text{r}} = \alpha_{\text{r}} + \beta_{\text{r}} \log_{10}\left(\dfrac{\bar{\sigma}}{G}\right) & \text{for} \quad \bar{\varepsilon}^{\text{tr}} > \bar{\varepsilon}^{\text{tr}^*}, \end{cases} \tag{14}$$

where α_j and β_j are model parameters. Note that κ must be non-negative, otherwise Eq. (12) produces a negative/positive $\dot{\bar{\varepsilon}}^{\text{tr}}$ when $\bar{\varepsilon}^{\text{tr}}$ is below/above $\bar{\varepsilon}^{\text{tr}^*}$. (Such behavior occurs during reverse creep, but the MD model is only designed to model forward creep.[22]) To enforce this, Eq. (14) is calculated first, and then

$$\kappa \leftarrow \max(\kappa, 0) \tag{15}$$

is applied.

The legacy MD model used a single mechanism to endow $\bar{\varepsilon}^{\text{tr}^*}$ with stress and temperature dependence. Reedlunn,[35] however, analyzed the WIPP salt data from Salzer et al.,[26] Düsterloh et al.,[27] Günther et al.[28] and discovered larger $\bar{\varepsilon}^{\text{tr}^*}$ values for $\bar{\sigma} < 8$ MPa than would be expected from extrapolating $\bar{\varepsilon}^{\text{tr}^*}$ values from higher stresses. (Bérest et al.[33] later found greater than expected transient creep limits as well.) Consequently, Reedlunn[23] added a second mechanism to capture the transient creep at low equivalent stresses:

$$\bar{\varepsilon}^{\text{tr}^*} = \sum_{i=0}^{1} \bar{\varepsilon}_i^{\text{tr}^*} \tag{16}$$

$$\bar{\varepsilon}_i^{\text{tr}^*} = K_i \exp(c_i\, T) \left(\frac{\bar{\sigma}}{G}\right)^{m_i} \tag{17}$$

where K_i, c_i, and m_i are parameters to be calibrated against experimental results. As before, the new transient strain limit mechanism, Mechanism 0, is given the same mathematical form as the original mechanism. This may be revisited if new information comes to light.

To summarize, the Reedlunn[23] enhancements to the legacy M–D model formulation are:

1. The equivalent stress (and flow potential) was generalized from Tresca to Hosford in Eq. (5)
2. Steady-state mechanism 0 was added in Eq. (9)
3. Transient strain limit mechanism 0 was added in Eq. (16).

Five calibrations of the M–D model are listed in Table 1. The legacy clean salt and legacy argillaceous salt calibrations were established in Ref. 6, while Calibration 1B, 2B, and 3B will be discussed in Section 3.2.

Note that all calibrations, except Calibration 3B, utilize $a = 1000$ as an approximation to the Tresca stress ($a = \infty$). Although special care was taken to make the Hosford stress less susceptible to numerical under and over-flow errors with large exponents (see Section 2.1

[1] Although repeated indices are usually summed from 1 to 3 in indicial notation, the summation in Eq. (7) is explicitly stated because the index is repeated more than twice.

Table 1
Munson–Dawson Calibrations. (Colors designate where a calibration deviated from both the legacy clean salt and the preceding calibration.)

Parameter	Units	Legacy Clean Salt	Legacy Arg. Salt	Cal 1B	Cal 2B	Cal 3B
G	GPa	12.4	12.4	12.4	12.4	12.4
B	GPa	20.7	20.7	20.7	20.7	20.7
a	–	1000	1000	1000	1000	16.0
A_0	s^{-1}	0	0	0	5.617×10^{1}	5.617×10^{1}
Q_0/R	K	0	0	0	5123	5123
n_0	–	0	0	0	1.595	1.595
A_1	s^{-1}	8.386×10^{22}	1.407×10^{23}	8.386×10^{22}	8.386×10^{22}	8.386×10^{22}
Q_1/R	K	12580.5	12580.5	12580.5	12580.5	12580.5
n_1	–	5.5	5.5	5.5	5.5	5.5
A_2	s^{-1}	9.672×10^{12}	1.314×10^{13}	1.074×10^{14}	4.415×10^{16}	4.415×10^{16}
Q_2/R	K	5032.2	5032.2	5177	5123	5123
n_2	–	5.0	5.0	5.353	6.279	6.279
$\bar{\sigma}_g$	MPa	20.57	20.57	20.57	20.57	20.57
B_0	s^{-1}	0	0	0	0	0
B_1	s^{-1}	6.086×10^{6}	8.998×10^{6}	6.086×10^{6}	6.086×10^{6}	6.086×10^{6}
B_2	s^{-1}	3.034×10^{-2}	4.289×10^{-2}	3.034×10^{-2}	3.034×10^{-2}	3.034×10^{-2}
q	–	5335	5335	5335	5335	5335
K_0	–	0	0	0	5.277×10^{-2}	5.277×10^{-2}
c_0	K^{-1}	0	0	0	8.882×10^{-3}	8.882×10^{-3}
m_0	–	0	0	0	0.9201	0.9201
K_1	–	6.275×10^{5}	2.470×10^{6}	3.918×10^{8}	3.052×10^{12}	3.052×10^{12}
c_1	K^{-1}	9.198×10^{-3}	9.198×10^{-3}	1.093×10^{-2}	8.882×10^{-3}	8.882×10^{-3}
m_1	–	3.0	3.0	4.041	5.282	5.282
α_h	–	−17.37	−14.96	3.367	3.367	3.367
β_h	–	−7.738	−7.738	−0.6838	−0.6838	−0.6838
α_r	–	0.58	0.58	0.58	0.58	0.58
β_r	–	0.0	0.0	0.0	0.0	0.0
α	K^{-1}	45.0×10^{-6}	45.0×10^{-6}	45×10^{-6}	45×10^{-6}	45×10^{-6}

in Ref. 25 or Section 3.1 and Appendix B.1 in Ref. 23), setting a much larger than 1000 still causes such errors. Fortunately, the largest difference between the exact Tresca stress and the Hosford stress with $a = 1000$ is only 0.07%. Using this approximation, instead of an exact expression for the Tresca stress, permitted all new simulations presented herein to be run with the latest M–D model implementation in Ref. 23.

2.1.2. A simple analysis of an axisymmetric compression creep test

This section analyzes an axisymmetric compression creep test to make $\dot{\bar{\varepsilon}}^{ss}$, $\bar{\varepsilon}^{tr}$, $\bar{\varepsilon}^{tr^*}$, and κ more concrete. The purpose of an axisymmetric creep test is to apply a known stress difference (a shear stress upon coordinate transformation) and monitor the amount of creep strain. Tests specimens are placed in an axisymmetric cell that allows the test operator to independently control the specimen temperature T, the axial Cauchy stress σ_{zz}, and the radial Cauchy stress σ_{rr}, while monitoring the axial strain ε_{zz}. The hoop stress $\sigma_{\theta\theta}$ is equal to σ_{rr}. Usually, the axial log strain (positive in compression) is calculated from the axial compressive displacement of the platens u as $\varepsilon_{zz} = \ln(1+u/L)$. Although axisymmetric compression specimens can barrel outwards due to friction at the top and bottom platens, the deformation and stresses are assumed to be spatially uniform herein.

The following sequence occurs in Fig. 1. First, T is raised to the test temperature and the hydrostatic pressure is raised to $\sigma_{rr} = \sigma_{\theta\theta} = \sigma_{zz} = 20$ MPa, causing a strain $\varepsilon_{zz}(t_{-1})$. At $t = t_0 = 0$, the axial stress is quickly raised to $\sigma_{zz} = 32$ MPa, changing $\bar{\sigma}$ from 0 to 12 MPa. This causes a rapid increase in the axial strain ε_{zz}. As the stress difference $\bar{\sigma}$ is held fixed for $t_0 < t < t_1 = 53$ days, the axial strain rate $\dot{\varepsilon}_{zz}$ slows down and eventually approaches a steady state rate $\dot{\bar{\varepsilon}}^{ss}$.

The quantities $\dot{\bar{\varepsilon}}^{ss}$, $\bar{\varepsilon}^{tr}$, $\bar{\varepsilon}^{tr^*}$, and κ can now be identified. Presuming $\dot{\varepsilon}_{zz}$ is sufficiently close the steady-state creep rate, $\dot{\bar{\varepsilon}}^{ss}$ is simply the slope of the dashed blue line labeled "SS fit". This dashed blue line can be shifted and extended, such that it passes through the point $\{t,\ \varepsilon_{zz}\} = \{0,\ \varepsilon_{zz}(t_{-1})\}$. The difference between the shifted, extended, dashed, blue line and the ε_{zz} vs. t curve is $\bar{\varepsilon}^{tr}$, plus a small amount of elastic strain $\Delta\bar{\sigma}(t_0)/E$, where $\Delta\bar{\sigma}(t_0) = 12$ MPa (in this instance) and $E = 9BG/(3B+G)$ is Young's modulus. The transient strain history is plotted in the bottom of Fig. 1, where $\bar{\varepsilon}^{tr}$ reaches a limiting value,

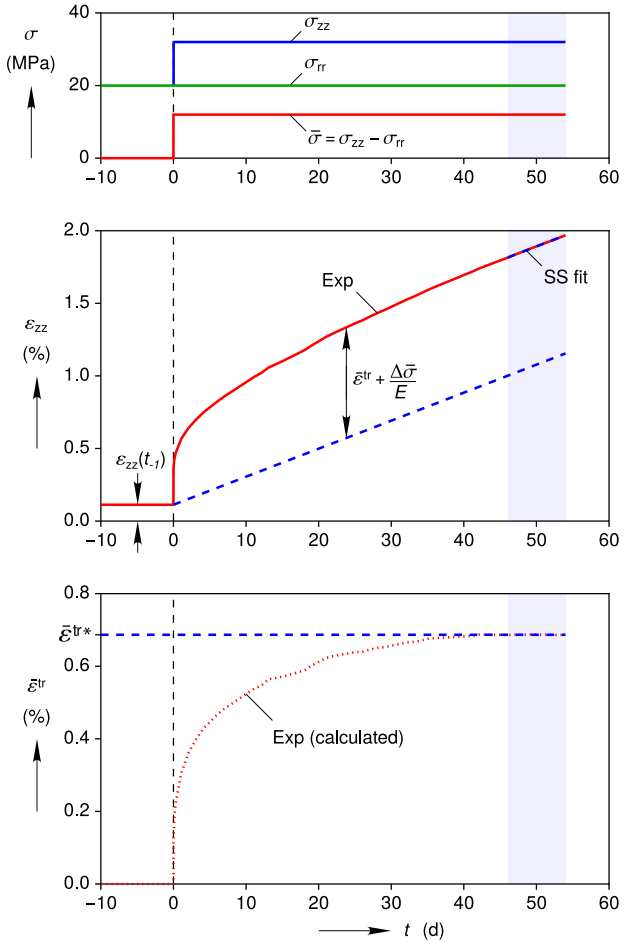


Fig. 1. Analysis of a simple axisymmetric compression creep tests.

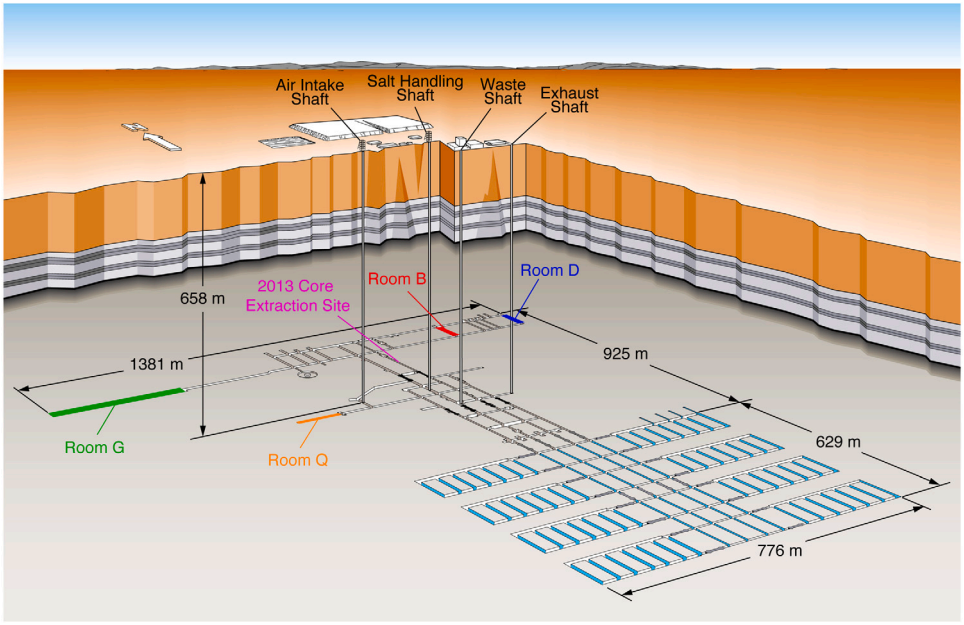


Fig. 2. Locations of Rooms D, B, G, and Q at the WIPP.

labeled $\bar{\varepsilon}^{\mathrm{tr}^*}$, once the creep rate reaches steady-state. Let t_i^- be the instant in time immediately before t_i, and t_i^+ be the instant in time immediately after t_i. The value of κ can be extracted by measuring $\dot{\epsilon}_{zz}(t_0^+) = \dot{\bar{\varepsilon}}^{\mathrm{vp}}(t_0^+)$ and substituting the result into

$$\kappa = \ln\left(\frac{\dot{\bar{\varepsilon}}^{\mathrm{vp}}(t_0^+)}{\dot{\bar{\varepsilon}}^{\mathrm{ss}}}\right), \tag{18}$$

which is obtained by combining Eqs. (8), (12) and (13), recognizing $\bar{\varepsilon}^{\mathrm{tr}}(t_0^+) = 0$, and taking the natural logarithm of both sides. In this manner, one can extract $\dot{\bar{\varepsilon}}^{\mathrm{ss}}$, $\bar{\varepsilon}^{\mathrm{tr}^*}$, and κ from each creep test and use those values to calibrate the material parameters in Eqs. (10), (11), (14) and (17).

2.1.3. Implementation, verification, and performance

The M–D model was implemented in Sierra/SolidMechanics[36] using an implicit (backward Euler) time integration scheme coupled to a line search routine, following the work of Scherzinger.[25] The new implementation was verified against analytical solutions for creep at a material point and against a previous implementation. Notably, the new implementation simulated Room D's closure 16.5× faster than the previous implementation. Further details of the new implementation, verification, and performance are provided in Chapter 3, Chapter 4, and Appendix C of Ref. 23.

2.2. Munson room closure model development

This sub-section presents the room closure model developed by Munson and co-workers during the 1980's and 1990's. Section 2.2.1 reviews the Room D, B, G, and Q experiments, Section 2.2.2 discusses early efforts to model the closure of Room D; Section 2.2.3 covers the Munson et al.[6] model changes to capture the Room D experiment; Section 2.2.4 details further changes to capture other room closure experiments; and Section 2.2.5 briefly describes how Munson and co-workers' room closure research was incorporated into the WIPP "porosity response surface" model.

2.2.1. The Room D, B, G, and Q experiments

Rooms D, B, G, and Q are drifts located in the northern experimental area at the WIPP (see Fig. 2). As shown in Fig. 3, Rooms D, B and G have square and rectangular initial cross sections with rounded corners, while Room Q has a circular initial cross-section. Rooms G and Q are also lower within the WIPP stratigraphy than Rooms D and B. Although Rooms D and B run north–south and Rooms G and Q run east–west, a local coordinate system is defined for each room, where the nominal initial width L_x, length L_y, and height L_z of the room are aligned with the x, y, and z directions, respectively. These nominal initial dimensions, as well as the nominal distance from Clay G L_g and the corner radius L_r, are listed in Table 2. The sources for these dimensions were Ref. 6, Fig. 3–3 for Rooms D and B, Ref. 37, Fig. 8 for Room G, Ref. 38, Fig. 5–4 for Room Q, and Ref. 39 for L_r in Rooms D, B, and G. After each room was excavated, an extensive effort confirmed that the actual, as-mined, dimensions of a given room met the design tolerances.[40] All rooms are long and slender (see Fig. 4) so analysts could assume that a cross-section midway along the length of the room deforms only in the x-z plane (a plane strain analysis).

Table 2
Nominal initial room dimensions.

Room	L_x (m)	L_y (m)	L_z (m)	L_r (m)	L_g (m)
D	5.5	93.3	5.5	0.46	4.42
B	5.5	93.3	5.5	0.46	4.42
G	6.1	359.7	3.05	0.46	−2.44
Q	2.9	108.6	2.9	1.45	−2.43

These four closure experiments were chosen for study herein, as opposed to the other experiments studied in Ref. 7, because the rooms are each relatively isolated, their geometries are simple, they are horizontally oriented, and they were unheated, at least for some of their histories. Room D was instrumental in developing the Munson et al.[6] room closure model, as will be discussed below. Room B was heated 0.95 yr after it was excavated, but Rooms D and B were nominally identical prior to heating, so it is useful to compare the closure measurements during the first 0.95 yr. Rooms G and Q are useful for further model validation due to their differing cross-sectional shapes and positions within the stratigraphy. Room G is particularly relevant, because its L_x/L_z aspect ratio and location within the stratigraphy are similar to many of the waste disposal rooms in the foreground of Fig. 2.

All four rooms were carefully instrumented to capture the closure immediately after excavation and for years afterward. The horizontal closure $\delta_x = \delta_x^{\mathrm{left}} + \delta_x^{\mathrm{right}}$ and vertical closure $\delta_z = \delta_z^{\mathrm{roof}} + \delta_z^{\mathrm{floor}}$

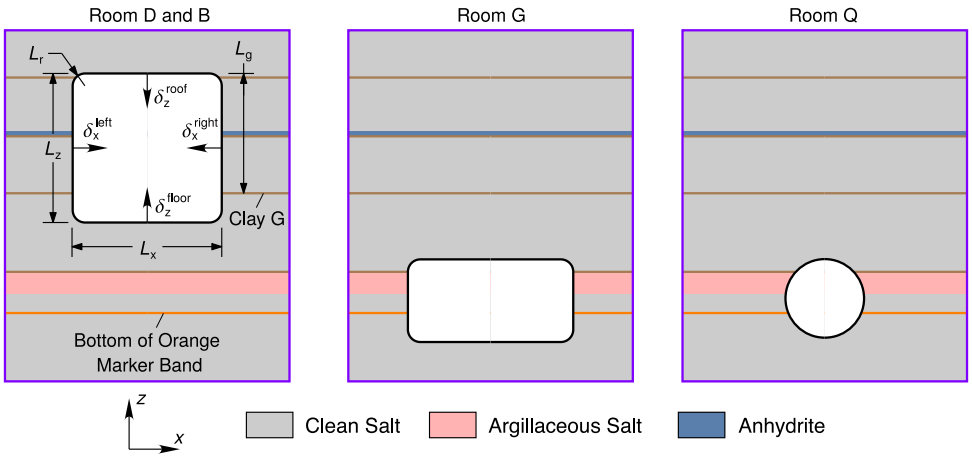


Fig. 3. Room D, B, G, and Q nominal initial cross-sectional geometries and locations within the 1983 reference stratigraphy.[41, Fig. 5] The stratigraphy shown also includes the bottom of a distinct orange marker band at 4.42 m below Clay G[38, Appendix B] for reference. (For interpretation of the references to color in this figure legend, the reader is referred to the web version of this article.)

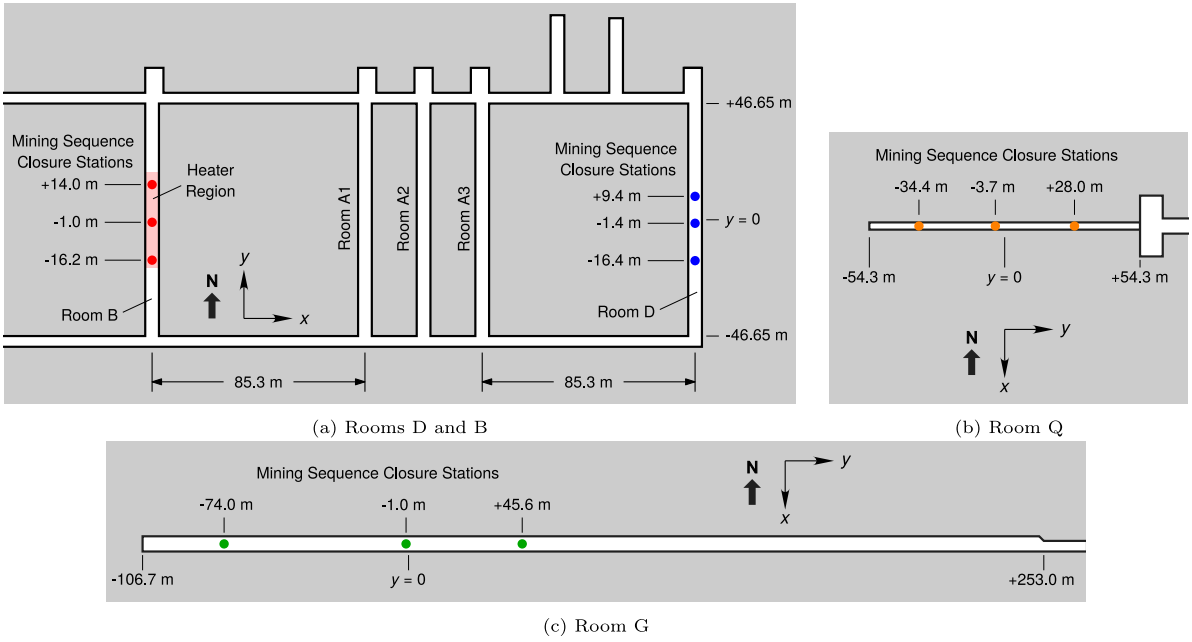


Fig. 4. Room D, B, G, and Q plan views.

were measured at room mid-height and room mid-width, respectively (see Fig. 3), at three closure stations along each room's length (see Fig. 4). The mining sequence measurements of room closure were started within a few hours after the mining face passed a closure station in order to capture the high closure rates $\dot{\delta}_x$ and $\dot{\delta}_z$ directly after a pass.[42] The rooms were mined in one to four passes, so the mining sequence gages were often destroyed and replaced several times. After each room was excavated, the mining sequence gages were augmented with temporary manual gages, and then by remotely read gages.[38,43–47]

Unfortunately, digital copies of the raw closure data from these experiments were inadvertently destroyed after the aforementioned reports were completed.[48,49] In addition, Munson et al.[45] did not clearly document the process of zeroing and shifting the mining sequence closure segments after each mining pass, and they did not directly compare the various closure measurements within the same room. As a result, Reedlunn and Williams[42] located the hand-written mining sequence closure measurement data sheets in the WIPP archives, digitized them, reconstructed the closure histories, and documented the process in detail. Most reconstructed closure histories were consistent with previously published results, but two deviations should be noted. First, the reconstructed Room Q central station closure histories after 30 d were about 45% lower than those reported in Ref. 7. (Reedlunn and Williams[42] presumed that Munson and co-workers shifted the measured Room Q closure histories upward to agree better with their simulation predictions.) Second, the hand-written data sheets found in the WIPP archives extended the Room D and G closure histories by 1.9× and 2.8× beyond those reported in Ref. 7, respectively.

Each room's three closure histories, as reconstructed, smoothed, and interpolated by Reedlunn and Williams[42], are compared in Fig. 5. The horizontal axis is the time t since each mining sequence closure station was excavated. It is encouraging to see that Room D and B both have almost the same δ_x and δ_z for $0 \leq t \leq 0.95$ yr, before the heaters were turned on in Room B. Station −74.0 m in Room G, on the other hand, exhibits less closure than the other two Room G stations. One potential cause is the Room G mining face was only ≈ 4 m from Station −74.0 m for several days after the station was first excavated, thereby subjecting Station −74.0 m to severe "end-effects" during its most rapid closure period.[42, see Fig. 3–11a] Nonetheless, the

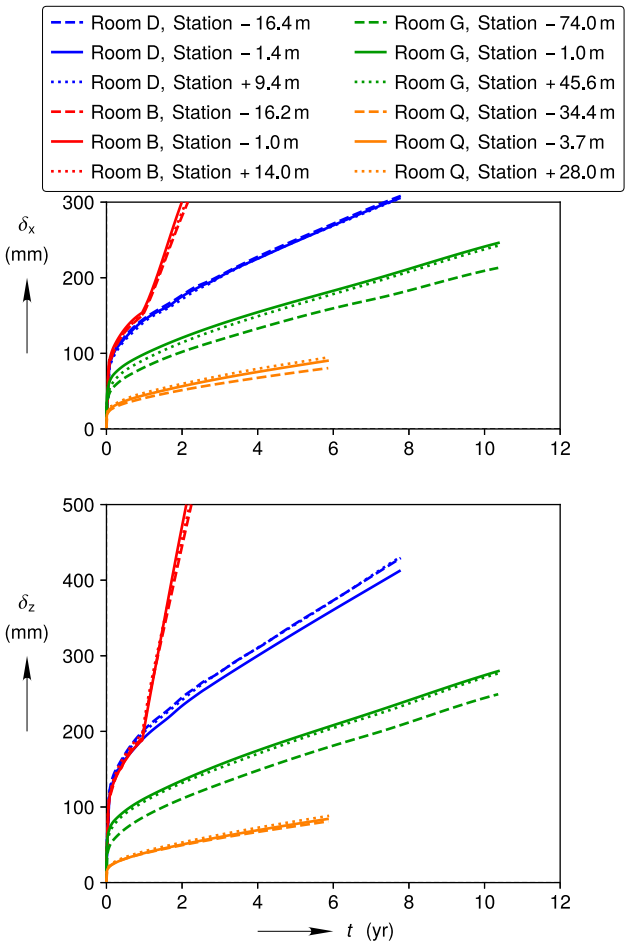


Fig. 5. Room closure histories for Room D, B, G and Q.[42] (For interpretation of the references to color in this figure legend, the reader is referred to the web version of this article.)

other closure histories for a given room agree reasonably well, which builds confidence in the quality of these experiments and suggests that one can treat the room closure along each room's mid-section as a plane strain boundary value problem.

2.2.2. *Early simulations of Room D*

Early in the WIPP project, thermal and structural analysts would each build their own model. Between 1979 and 1983, a series of meetings were held between the Department of Energy, Bechtel, TSC/D'Appolonia, and Sandia to establish a common model setup. This culminated in the 1983 reference,[41] which specified a reference stratigraphy, and a group of reference material models. The agreed-upon idealization of the actual stratigraphy at the WIPP is shown in Fig. 6. Layers are color coded as to whether they are clean salt, argillaceous salt, anhydrite, or polyhalite. The anhydrite and polyhalite layers have names, such as marker bed (MB) 139. Some layers have clay seams between them, marked with brown lines. All elevations are referenced off of Clay G, which is about 648 m beneath the earth's surface.[43] The material models and material parameters in the 1983 reference were not expected to be the final values, but analysts were expected to provide justifications for changing them. For instance, soon after the 1983 reference was established, a memorandum[50] updated the Drucker–Prager constants for the anhydrite and polyhalite based on a collection of experimental data.

The first several published simulations of Room D[3,5] were faithful to the 1983 reference. The calculations were performed using SANCHO,[51]

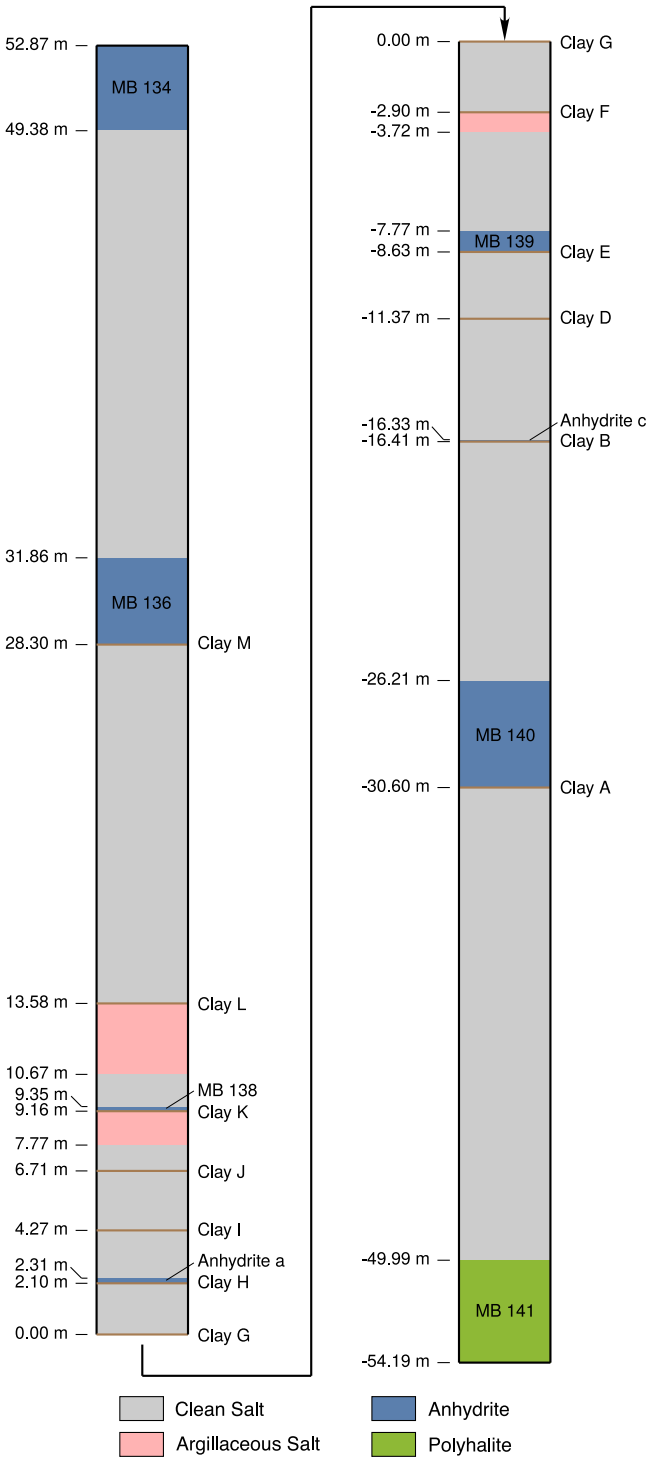


Fig. 6. 1983 reference stratigraphy. (For interpretation of the references to color in this figure legend, the reader is referred to the web version of this article.)
Source: Recreated from Fig. 5 in Ref. 41.

a two-dimensional, large deformation, finite element code. A schematic of the boundary conditions is shown in Fig. 7. The room was assumed to be sufficiently long in the y-direction (into the page) to assume deformations remain in x–z plane. A mirror boundary condition was assumed on the left side, while the right side was deemed far enough away from Room D to place rollers on most of the right boundary. The displacement of the upper anhydrite layer's right side (the upper

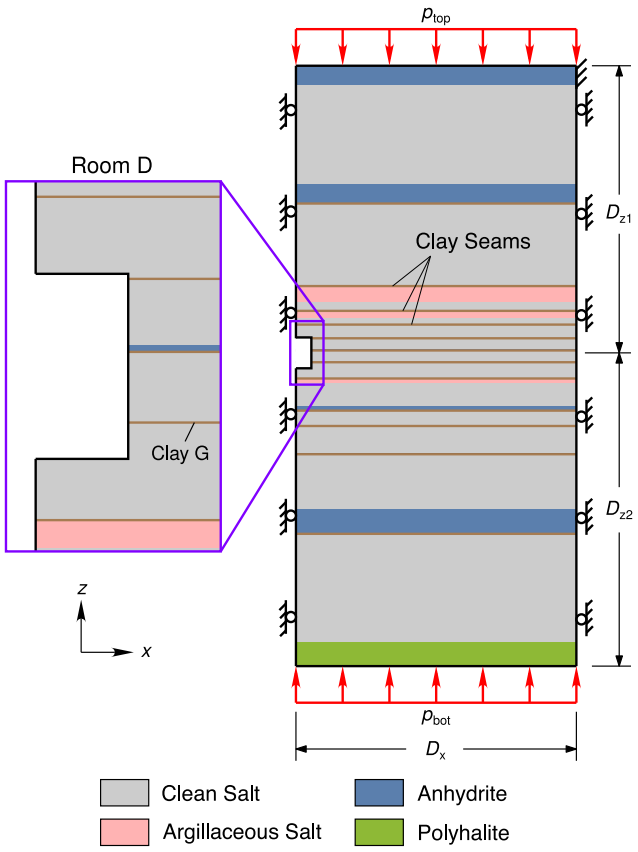


Fig. 7. Original boundary conditions. (For interpretation of the references to color in this figure legend, the reader is referred to the web version of this article.)
Source: Recreated from Fig. 9 in Ref. 3.

right corner in Fig. 7) was fully fixed to constrain translation in the z-direction. The pressure applied to the top surface was $p_{top} = 13.57$ MPa. The pressure applied to the bottom surface $p_{bot} = 15.97$ MPa represented the overburden minus the missing rock from Room D. The domain boundaries in Fig. 7 were $D_x = 50$ m, $D_{z1} = 51.2$ m, and $D_{z1} = 55.86$ m away from the center of Room D. The room corners were sharp, as shown in Fig. 7, instead of the rounded corners shown in Fig. 3. The density of the clean salt, argillaceous salt, anhydrite, and polyhalite was taken as $\rho = 2300$ kg/m^3, and the acceleration due to gravity was set to $g = 9.79$ m/s^2. Non-zero deviatoric stresses in rock salt relax to zero due to creep relatively quickly compared to typical geologic time scales, so the deviatoric stress prior to room excavation was assumed to be zero throughout the domain, and all material points were initialized with a lithostatic stress state that varied linearly from p_{top} at the top of the model to p_{bot} at the bottom of the model. The room was assumed to appear instantaneously as a void at time $t = 0$, rather than modeling the excavation process. For simplicity, the rock mass temperature was assumed to be spatially constant at 300 K. The lateral sliding of the layers on either side of a clay seam were modeled using Coulomb friction, with a friction coefficient of $\mu_c = 0.4$. The salt was modeled using the secondary creep law and parameter set specified in the 1983 reference. Both the argillaceous and clean salt used the same set of parameters. The anhydrite and polyhalite were modeled with a hypoelastic, perfectly plastic, Drucker–Prager model with a non-associated flow rule (see Appendix B.1 for further details).

These first simulations that utilized the 1983 reference compared quite poorly against the experimental Room D measurements. In Fig. 8, the initial horizontal and vertical closure predictions are labeled as

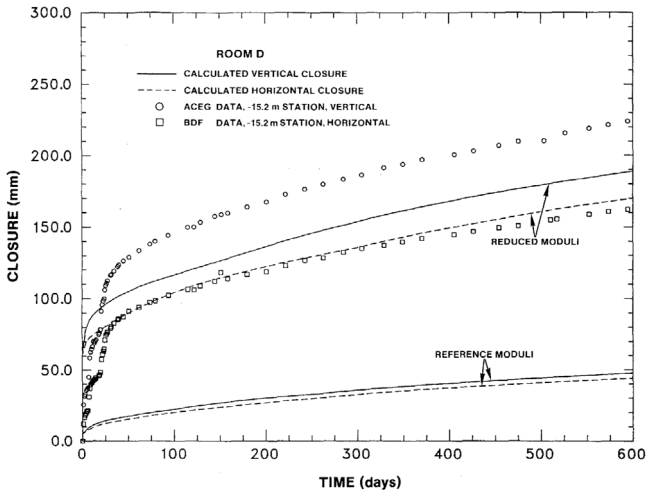


Fig. 8. Initial predictions of Room D's closure (solid and dashed lines) compared against closure measurements (markers).
Source: Reprinted with permission from Ref. 5.

"Reference Moduli", while the measured closure[2] is denoted using markers. The lack of agreement appears due to a significant under-prediction of the early closure rate and a lesser under-prediction of the later closure rate. After 50 days, the simulation under-predicts the vertical closure by 7.4×. After 600 days, as the room closure transitions toward more steady behavior, the discrepancy reduces to 4.0×.

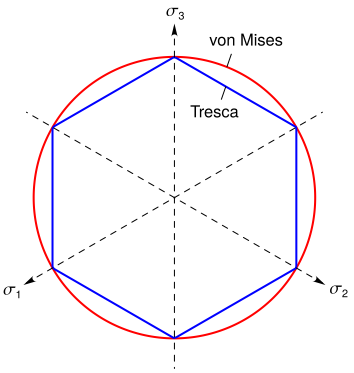
The inability to predict underground test results, such as those in Fig. 8, caused much consternation in the WIPP Thermal/Structural Interactions program. Similar disparities were found when comparing the South Drift closure measurements against simulations using the 1983 reference salt model[1,2] and the M–D model.[4] Morgan et al.[1,2] showed through a parametric study that the discrepancy could not be due to known uncertainties in the salt material parameters, the anhydrite material parameters, the clay seam friction coefficient μ_c, and several other items. Consequently, some analysts resorted to reducing the, laboratory measured, salt elastic moduli by a factor of 12.5 to match the horizontal closure of the South Drift. Using these decreased moduli, Munson et al.[5] calculated Room D closures that were in reasonable agreement with the measurements (see "Reduced Moduli" predictions in Fig. 8). Munson et al.[6], however, deemed this approach "not acceptable from the standpoint of obtaining a predictive capability since the reduced moduli values cannot be substantiated by laboratory tests".

2.2.3. Changes made by Munson et al.[6]

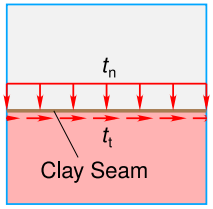
In order to improve the match between the simulation predictions and the measured closure of Room D, without reducing the elastic moduli by 12.5×, Munson et al.[6] elected to make the following six significant changes to the room closure model.

1. Munson et al.[6] switched the M–D model's equivalent stress measure from the von Mises stress to the Tresca stress. As shown in the π-plane plot in Fig. 9(a), the maximum difference between these two equivalent stress measures is only 15.5%, so one might not expect a large impact on the room closure. This difference, however, gets amplified by the exponents in Eqs. (10), (11) and (17). For example, typically $n_2 \approx 5$, so a 15.5% increase in $\bar{\sigma}$ causes a 2.05× increase in $\dot{\bar{\varepsilon}}_2^{ss}$. Munson

[2] Fig. 8 plots the closure measurements from Station −15.2 m, but Munson et al.[43,45] do not mention a Station −15.2 m. Station −15.2 m was probably renamed to Station −16.4 m after Ref. 5 was published.



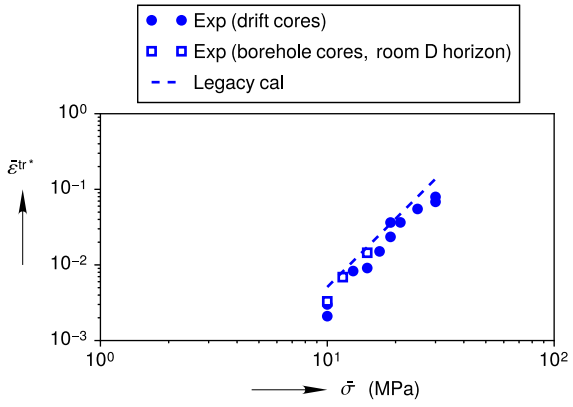
(a) Replaced von Mises with Tresca equivalent stress



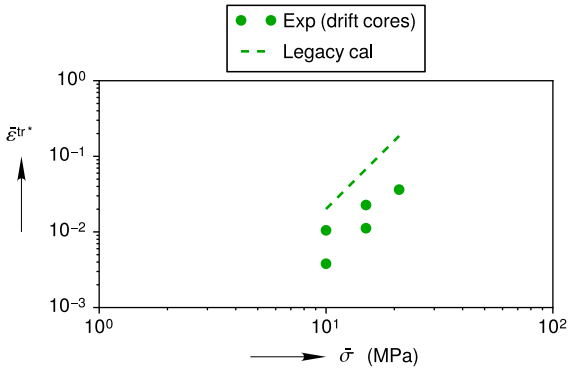
Coulomb Friction
$t_t = \eta\, t_n$

$\eta = 0.4 \rightarrow 0.2$

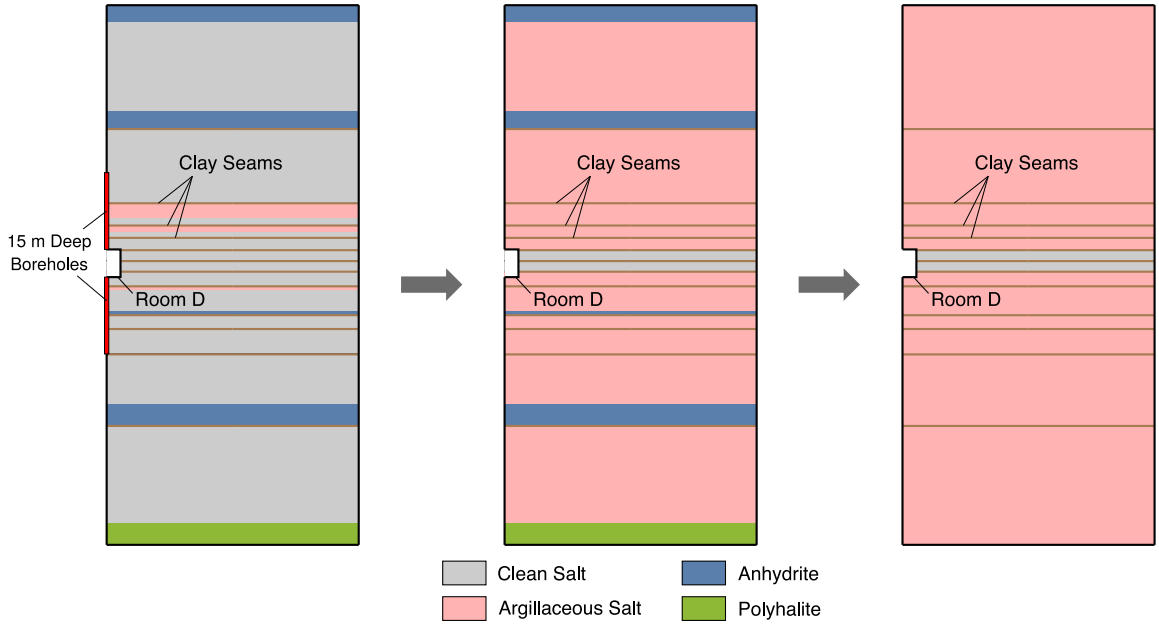
(b) Reduced the clay seam friction coefficient



(c) Increased the transient strain limit for clean salt



(d) Increased the transient strain limit for argillaceous salt



(e) Replaced nearly all clean salt with argillaceous salt. Then replaced all anhydrite (and polyhalite) with argillaceous salt

Fig. 9. Summary of the six significant modifications made in Ref. 6. (For interpretation of the references to color in this figure legend, the reader is referred to the web version of this article.)

et al.[6] justified the switch to the Tresca equivalent stress by inspecting measurements on hollow cylinders of Avery Island rock salt subjected to axial compression, internal pressurization, and external pressurization. The details of these hollow cylinder tests were later published in Ref. 52.

2. Munson et al.[6] reduced the coefficient of friction at the clay seams from 0.4 to 0.2 (see Fig. 9(b)), based on engineering judgement. They candidly stated that the coefficient of friction was "a free parameter" of the model because, although clay

seams at the WIPP were known to slide, clay seam behavior had not been experimentally characterized.

3. Munson et al.[6] altered the clean salt M–D model calibration. They justified altering the original calibration[21,22] based on new creep tests in Senseny[53] and new, unpublished, creep tests that were later documented in Senseny[54]. The new axisymmetric creep tests were preferred over the old tests because Senseny was careful to retain the "loading strains" accumulated while applying axisymmetric stresses at the start of the experiments. In addition, three ERDA-9-D specimens from Ref. 54 were thought to be close approximations to virgin salt because they came from borehole cores rather than drift cores. The drift core specimens in Ref. 53 were extracted months, if not years, after the drifts were excavated. The salt surrounding the drift experienced a significant amount of deformation between drift excavation and core extraction. This "excavation hardening" was thought to cause the $\bar{\varepsilon}^{\mathrm{tr}*}$ values measured on drift core specimens to be lower than virgin values. Thus, Munson et al.[6] chose $K_1 = 6.275 \times 10^5$ for the clean salt, which placed the dashed line at the upper edge of the clean salt experimental data in Fig. 9(c).
4. Munson et al.[6] created a new argillaceous salt M–D model calibration, because Senseny[53] also found that the argillaceous salt specimens crept more than the clean salt specimens. For the argillaceous salt, they chose $K_1 = 2.470 \times 10^6$, which placed the dashed line well above the five data points in Fig. 9(d). To justify the argillaceous K_1, Munson et al.[6] state that they did not have any fresh, argillaceous, borehole specimens from the Room D horizon to limit the value of K_1. In other words, the argillaceous K_1 was treated as another "free parameter" of the model.
5. Munson et al.[6] changed nearly all the clean salt in the 1983 reference stratigraphy to argillaceous salt, as demonstrated in the Fig. 9(e) center schematic. Only the salt strata between clay I and clay G were left as clean salt. To justify the change, they state that boreholes were drilled 15 m into the roof and floor of Room D, and both cores appeared to be argillaceous to the eye. No composition measurements or mechanical tests were made to confirm this assertion. Furthermore, they simply assumed that all salt beyond the aforementioned 15 m boreholes was argillaceous.
6. Munson et al.[6] chose not to model the anhydrite or polyhalite layers "[b]ecause these layers are either sufficiently thin to be insignificant in the calculational response or are sufficiently removed from the room being simulated to be quite uninfluential in the calculational response". Munson et al.[6] did not specify what they replaced the anhydrite and polyhalite layers with, but Munson and DeVries[55] states that Munson et al.[6] "substituted argillaceous salt layers for anhydrite layers". (Presumably the polyhalite layer was also replaced with argillaceous salt.) This new stratigraphy is depicted in Fig. 9(e) rightmost schematic.

Munson et al.[6] also made three minor changes. The first two were constitutive model modifications: they added an exponent of 2 to $\left(1 - \bar{\varepsilon}^{\mathrm{tr}}/\bar{\varepsilon}^{\mathrm{tr}*}\right)^2$ in Eq. (13) and added the $\exp(c_i T)$ factor to Eq. (17). These two changes seem reasonably justified by laboratory experiments. The third change prohibited sliding at the three clay seams furthest from the room (clay A, B, and M).

A simulation with these changes was run using SPECTROM-32,[56] a two-dimensional, small-strain, finite element code, and the results are shown in Fig. 10. The results were described as follows: "In view of the complexity of this calculation, the agreement between calculation and measurement is, we believe, exceptional. These results simulate the measured data much more exactly than any previous reference calculation. The agreement between calculated and measured vertical closure is so close, about 2%, in magnitude and form that little can be said. However, there remains enough uncertainty in the exact values of the argillaceous transient strain limit and the clay seam coefficient of friction that the closeness of the calculation to the measured closure is better than could be expected." Note that the underline of the last sentence was copied verbatim from Ref. 6. The report ends with, "In summary, the results of this work suggest a relatively large stride has been taken in the development of the predictive technology for the structural response of salt."

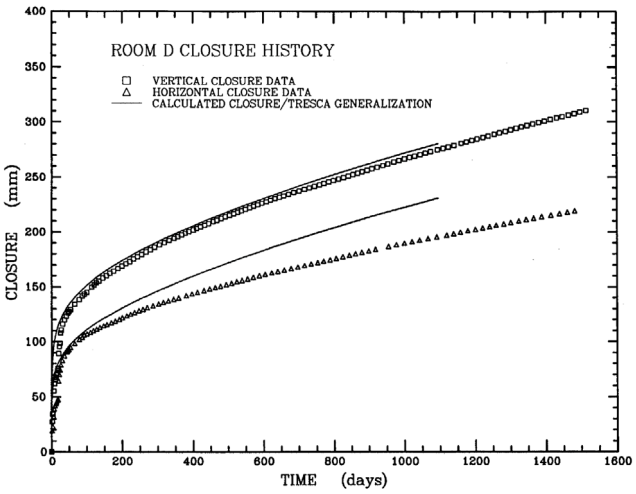


Fig. 10. Simulation predictions of Room D horizontal and vertical closure after the modifications in summarized in Fig. 9.[6]

2.2.4. Further room closure simulations by Munson and co-workers

A series of subsequent technical reports and conference papers by Munson and co-workers continued to use many of the changes proposed in Ref. 6, but with further modifications. For example, Munson et al.[57,58] re-included the anhydrite layers in their Room B and Room A series simulations, after neglecting them in the Room D simulation. This choice does not seem justified given that Room D, B, and A series are at the same elevation in the WIPP stratigraphy. Other simulations of Room G, the South Drift, and Room Q closure also included the anhydrite layers, but they utilized $K_1 = 1.783 \times 10^6$ instead of $K_1 = 2.470 \times 10^6$ for the argillaceous salt without detailing reasons for the change.[55,59] Changes such as these are not unexpected during model development, yet Munson[7] did not discuss the differences between the model setups when he presented the closure simulation results in his capstone paper. He presented the Room D, B, A series, G and Q simulations as if all included the anhydrite layers and all used $K_1 = 1.783 \times 10^6$ for the argillaceous salt. He also did not mention whether all simulations used comparable numerical settings, such as finite element size and type. Finally, he did not discuss the other speculative changes in Ref. 6, such as converting nearly all the clean salt to argillaceous salt and changing μ_c from 0.4 to 0.2.

2.2.5. Stone's[60] simulations

Munson's model was changed yet further before being used for official WIPP room closure predictions. Stone[60] simplified the stratigraphy by replacing all the anhydrite and polyhalite layers, except marker bed 139 and anhydrite "a", with argillaceous salt, and by removing all clay seams (see Fig. 11). These changes presumably made running a large number of simulations using 1990's computing technology more tractable. (See Ref. 20, A-47 through A-119 for justification of these changes.) In addition, the transient strain limit coefficient was returned to $K_1 = 2.470 \times 10^6$.

Stone[60] used this geomechanical model to simulate the closure of disposal rooms filled with waste containers and varying amounts of gas due to cellulose degradation and metal corrosion. These simulations generated what is referred to as the "porosity response surface",

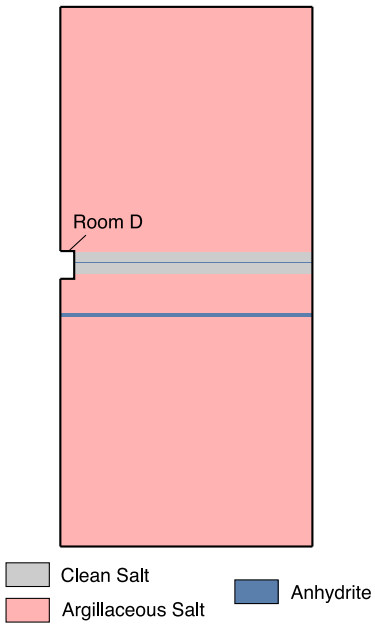


Fig. 11. Stone[60] stratigraphy applied to Room D. (For interpretation of the references to color in this figure legend, the reader is referred to the web version of this article.)

which describes the porosity of a disposal room as a function of time and gas generation rate. This porosity response surface was utilized to predict the gas storage volume within a disposal room and the room's permeability to fluid flow for the WIPP Compliance Certification Application.

3. Reinvestigation

Cautiously tuning a model to match underground structural measurements can be acceptable if a single tuned parameter set can capture more than one underground measurement, and if the tuning is clearly disclosed each time the model is used in the future. These two conditions, however, are not always met, as Section 2.2 demonstrates. Concerns about the Munson et al.[6] numerical settings, neglect of the anhydrite layers, reassignment of clean salt into argillaceous salt, and treatment of argillaceous salt transient creep led to the reinvestigation described in this section. In view of these concerns, this reinvestigation seeks to predict unheated room closure at the WIPP using numerically converged models that are calibrated as much as possible against laboratory measurements.

Section 3.1 covers our initial Room D simulations, Section 3.2 details several new calibrations of the M–D model, Section 3.3 describes the calibrations' effect on the Room D closure predictions, Section 3.4 presents some domain size convergence studies, and Section 3.5 compares simulations of Room D, G, and Q using a Stone[60] type model to the model developed herein. All new simulations were run using Sierra/SolidMechanics[36]. For convenience from here forward, the mesh, boundary conditions, material model calibrations, etc. used by Munson et al.[6] will be referred to as the legacy mesh, legacy boundary conditions, legacy calibrations, etc. Table 3a lists all the reinvestigation simulations, each with a unique simulation identifier (ID). The table details which room was being simulated; the name of the M–D model calibration; any deviations from the M–D calibration; the anhydrite flow potential dilatation angle ω (see Appendix B); the stratigraphy identifier (Strat. ID) (see Table 3b); the domain size D (see Section 3.4); the boundary conditions (BCs); the element type (MQ = mean quadrature, SD = selective deviatoric); the maximum relative residual $\hat{R}_{\max}$; the finite element width H near the room; and the time step size growth rate γ. These last four numerical settings are defined more precisely in Appendix A.1. The anhydrite/polyhalite were modeled using the anhydrite and polyhalite models described in Appendix B. If an anhydrite/polyhalite layer was not included in a given stratigraphy, it was modeled as argillaceous salt. Any clay seams not included in a given stratigraphy were tied (glued).

The following sub-sections present a number of model improvements, but two further improvements were omitted. First, although the actual rooms included rounded room corners (see Fig. 3), the corners were left square for the simulations herein. Rounded corners only modestly reduced the horizontal and vertical closure by 4% and 3%, respectively, at $t = 3.7$ yr,[35] but, the finite elements within the rounded corners became severely distorted when the walls came close to touching the roof and floor after several decades of room closure, which caused solver convergence issues. Second, modeling the multi-pass excavation sequence in Room D was considered, yet rejected, based on a study by Arguello et al.[61] They compared Room D closure predictions after instantaneous excavation against those after the multi-pass, three-dimensional, excavation process actually employed in the Room D experiment, using the secondary creep law from the 1983 reference.[41] They found substantially different closures during the multi-pass excavation, but only slight differences remained after $t = 90$ days, suggesting the instantaneous excavation may be appropriate for the long-term response of a room. Repeating this multi-pass excavation study with tighter numerical settings and more sophisticated salt material models could be worthwhile at a future date, but all simulations herein began with instantaneous room excavation for simplicity.

3.1. Initial study

The first step of the initial study was to recreate the legacy closure simulation as closely as possible using Sierra/SolidMechanics[36]. As before, the simulation utilized the legacy boundary conditions shown in Fig. 7, the Munson et al.[6] stratigraphy depicted in the rightmost schematic in Fig. 9(e), sliding on clay seams D through L, a clay seam friction coefficient $\mu_c = 0.2$, the legacy M–D model calibrations listed in Table 1, $\rho = 2300$ kg/m^3, $g = 9.79$ m/s^2, and $T = 300$ K over the whole model. Salt cannot sustain a deviatoric stress over the long-term, so all material points were initialized with a lithostatic stress state that varied linearly from p_{top} to p_{bot}. The room was treated as a void that appeared virtually instantaneously at time $t = 0$. Munson et al.[6] did not specify any numerical details, so a number of educated guesses were made, as detailed in Appendix A.1.

Results from the legacy simulation (Simulation 0, manually digitized from Fig. 10) and the recreated legacy simulation (Simulation 1) are compared in Fig. 12, where the closures δ_x and δ_z are respectively normalized by the room width L_x and height L_z. The experimental measurements in Fig. 12 correspond to the central Room D mining sequence closure station (Station −1.4 m). The recreated vertical closure is quite close to the legacy vertical closure, but the recreated horizontal closure is somewhat low compared to the legacy horizontal closure. The small horizontal closure difference may be due to the way that SPECTROM-32 and Sierra/SolidMechanics handle sliding at the clay seams. Morgan et al.[62] performed a benchmarking exercise between different finite element codes, and traced back discrepancies between SANCHO and SPECTROM-32 to the contact and sliding algorithms. Regardless, the agreement between the legacy results and the legacy recreated results is quite good considering that about 30 years separate the two simulations.

The second step of the initial study was to update the numerics to today's computational standards. As detailed in Appendix A.2, the finite element mesh was improved, a more accurate element type was selected, and convergence studies helped select the following numerical settings: $\hat{R}_{\max} = 10^{-5}$, $H = L_x/48$, and $\gamma = 2\%$. The impact of more accurately solving the initial boundary value problem is seen by comparing the legacy recreated simulation (Simulation 1) with the

Table 3
Simulation and stratigraphy lists.

(a) Simulation list

		M–D calibration		Anhyd.	Domain			Numerical settings			
Sim ID	Room	Name	Deviations	ω	Strat. ID	D	BCs	Element	$\hat{R}_{\max}$	H	γ
1	D	Legacy	–	–	2c	~ 50 m	Fig. 7	MQ	10^{-3}	$L_x/12$	5%
2a	D	Legacy	–	0.423	2a	~ 50 m	Fig. 18	SD	10^{-3}	$L_x/48$	2%
2b	D	Legacy	–	0.423	2a	~ 50 m	Fig. 18	SD	10^{-4}	$L_x/48$	2%
2c	D	Legacy	–	0.423	2a	~ 50 m	Fig. 18	SD	10^{-5}	$L_x/48$	2%
2d	D	Legacy	–	0.423	2a	~ 50 m	Fig. 18	SD	10^{-6}	$L_x/48$	2%
2e	D	Legacy	–	0.423	2a	400 m	Fig. 18	SD	10^{-4}	$L_x/48$	2%
2f	D	Legacy	–	0.423	2a	400 m	Fig. 18	SD	10^{-5}	$L_x/48$	2%
2g	D	Legacy	–	0.423	2a	400 m	Fig. 18	SD	10^{-6}	$L_x/48$	2%
2h	D	Legacy	–	0.423	2a	400 m	Fig. 18	SD	10^{-7}	$L_x/48$	2%
2i	D	Legacy	–	0.423	2a	400 m	Fig. 18	SD	10^{-7}	$L_x/6$	2%
2j	D	Legacy	–	0.423	2a	400 m	Fig. 18	SD	10^{-7}	$L_x/12$	2%
2k	D	Legacy	–	0.423	2a	400 m	Fig. 18	SD	10^{-7}	$L_x/24$	2%
2h	D	Legacy	–	0.423	2a	400 m	Fig. 18	SD	10^{-7}	$L_x/48$	2%
2l	D	Legacy	–	0.423	2a	400 m	Fig. 18	SD	10^{-7}	$L_x/96$	2%
2m	D	Legacy	–	0.423	2a	400 m	Fig. 18	SD	10^{-7}	$L_x/48$	8%
2n	D	Legacy	–	0.423	2a	400 m	Fig. 18	SD	10^{-7}	$L_x/48$	4%
2	D	Legacy	–	–	2c	~ 50 m	Fig. 7	SD	10^{-5}	$L_x/48$	2%
3	D	Legacy	–	–	2c	~ 50 m	Fig. 18	SD	10^{-5}	$L_x/48$	2%
4	D	Legacy	–	–	2b	~ 50 m	Fig. 18	SD	10^{-5}	$L_x/48$	2%
5a	D	Legacy	–	0	2a	~ 50 m	Fig. 18	SD	10^{-5}	$L_x/48$	2%
5b	D	Legacy	–	0.106	2a	~ 50 m	Fig. 18	SD	10^{-5}	$L_x/48$	2%
5c	D	Legacy	–	0.211	2a	~ 50 m	Fig. 18	SD	10^{-5}	$L_x/48$	2%
5d	D	Legacy	–	0.423	2a	~ 50 m	Fig. 18	SD	10^{-5}	$L_x/48$	2%
5	D	Legacy	–	0.423	2a	~ 50 m	Fig. 18	SD	10^{-5}	$L_x/48$	2%
6	D	Legacy	–	0.423	1	~ 50 m	Fig. 18	SD	10^{-5}	$L_x/48$	2%
7	D	1B	–	0.423	4	~ 50 m	Fig. 18	SD	10^{-5}	$L_x/48$	2%
8	D	1B	Moduli reduced 12.5×	0.423	4	~ 50 m	Fig. 18	SD	10^{-5}	$L_x/48$	2%
9	D	2B	$K_0 = 0$	0.423	4	~ 50 m	Fig. 18	SD	10^{-5}	$L_x/48$	2%
10	D	2B	–	0.423	4	~ 50 m	Fig. 18	SD	10^{-5}	$L_x/48$	2%
11	D	3B	–	0.423	4	~ 50 m	Fig. 18	SD	10^{-5}	$L_x/48$	2%
12	D	3B	$a = 4$	0.423	4	~ 50 m	Fig. 18	SD	10^{-5}	$L_x/48$	2%
13	D	Legacy	–	0.423	2a	100 m	Fig. 18	SD	2.2×10^{-6}	$L_x/48$	2%
14	D	Legacy	–	0.423	2a	200 m	Fig. 18	SD	4.6×10^{-7}	$L_x/48$	2%
15	D	Legacy	–	0.423	2a	400 m	Fig. 18	SD	10^{-7}	$L_x/48$	2%
16	D	3B	–	0.423	4	100 m	Fig. 18	SD	2.2×10^{-6}	$L_x/48$	2%
17	D	3B	–	0.423	4	200 m	Fig. 18	SD	4.6×10^{-7}	$L_x/48$	2%
18	D	3B	–	0.423	4	400 m	Fig. 18	SD	10^{-7}	$L_x/48$	2%
19	D	Legacy	–	0.423	3	400 m	Fig. 18	MQ	10^{-7}	$L_x/12$	2%
20	G	Legacy	–	0.423	3	400 m	Fig. 18	MQ	10^{-7}	$L_x/12$	2%
21	Q	Legacy	–	0.423	3	400 m	Fig. 18	MQ	10^{-7}	$\pi L_r/10$	2%
22	G	3B	–	0.423	4	200 m	Fig. 18	SD	4.6×10^{-7}	$L_x/54$	2%
23	Q	3B	–	0.423	4	200 m	Fig. 18	SD	4.6×10^{-7}	$\pi L_r/38$	2%

(b) Stratigraphy list

Strat. ID	Reference	Deviations from reference	Schematic
1	Ref. 41 (1983 Reference)	–	Fig. 6 and leftmost in Fig. 9(e)
2a	Ref. 6	Included Clay A, Clay B, Clay M, MB 134, MB 136, MB 138, MB 139, MB 140, MB 141, and anhydrite "a"	Center in Fig. 9(e)
2b	Ref. 6	Included Clay A, Clay B, and Clay M	Rightmost in Fig. 9(e)
2c	Ref. 6	–	Rightmost in Fig. 9(e)
3	Ref. 60	–	Fig. 11
4	Herein	–	Fig. 18

improved numerics simulation (Simulation 2) in Fig. 12. The horizontal and vertical closure at $t = 7.8$ yr increased by 1.38× and 1.34×, respectively, such that the improved numerics simulation no longer agrees well with the experimental measurements of Room D's closure.

The third step involved two minor changes. First, the vertical boundary conditions in Fig. 7 (the pressure at the bottom of the domain and the fixed upper right anhydrite layer) seemed unnecessarily complex, so they were simplified to the boundary conditions shown in Fig. 18. Second, Munson et al.[6] prohibited sliding at Clay A, B, and M, but it seemed prudent to let the mechanics determine which seams slide, so all the clay seams called out in the 1983 reference stratigraphy[41] were allowed to slide. Fig. 12 shows these two changes (Simulation 3 and 4) had nearly imperceptible impacts on the closure histories.

The fourth step of the initial study put the anhydrite and polyhalite back into the stratigraphy, reversing the second stratigraphy change in Fig. 9(e). As shown in Appendix B.2, initial attempts to use the legacy anhydrite model resulted in strain localizations and solver convergence issues. These issues were resolved by changing the anhydrite flow rule from non-associative to associative, which, in itself, appeared to have a negligible impact on the closure predictions (see Fig. B.32). Putting the anhydrite (and polyhalite) back in the stratigraphy, on the other hand, had a substantial impact (compare Simulation 4 to 5 in Fig. 12). The horizontal and vertical closure reduced by factors of 0.71× and 0.70× at $t = 7.8$ yr, respectively, which refutes the assumption in Ref. 6 that the anhydrite and polyhalite layers are negligible. Ironically, adding the anhydrite and polyhalite approximately canceled out the impact of resolving the numerics (compare the Simulation 1 and 5 closure predictions in Fig. 12).

The fifth and final step of the initial study changed the stratigraphy back to the 1983 reference stratigraphy, reversing the first stratigraphy change in Fig. 9(e). The resulting room closure predictions (Simulation

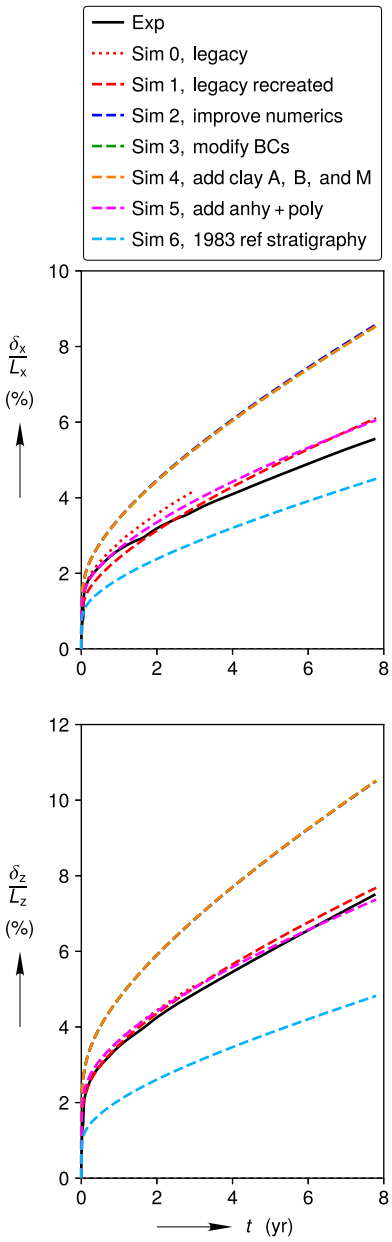


Fig. 12. Simulation predictions and experimental measurements of Room D horizontal and vertical closure histories. Note that the closure histories from Simulations 2, 3, and 4 almost exactly overlap. (For interpretation of the references to color in this figure legend, the reader is referred to the web version of this article.)

6 in Fig. 12) under-predict the measured δ_x/L_x and δ_z/L_z values by 1.23× and 1.56× at $t = 7.8$ yr, respectively. This under-prediction shows that Munson et al.'s[6] ability to capture Room D's closure partially depended on their poorly supported claim that nearly all clean salt was argillaceous salt. Their ability to capture Room D's closure also depended on their speculative M–D model calibrations, as will be shown in Sections 3.2 and 3.3. Note that the remainder of this paper will compare new simulations against Simulation 5, rather than Simulation 6, because Simulation 5 is likely what Munson would have preferred to simulate if the computational power had been available at the time.

3.2. New Munson–Dawson model calibrations

Sandia and RE/SPEC performed a large number of geomechanical laboratory tests on WIPP salt in the 1980s and 1990s. (See Ref. 16 for a summary of the RE/SPEC tests.) These tests served as the basis for the M–D model legacy calibrations in Table 1. The Joint Project III partners considered calibrating their models against these legacy tests as well, but they eventually decided to conduct their own series of tests on WIPP salt for several reasons. Measurement and control technologies have improved since the 1990s, as have experimental procedures for determining model parameters. Most importantly, the legacy strength tests did not include measurements of sample dilation, which are required to calibrate the damage and healing processes in the German models.

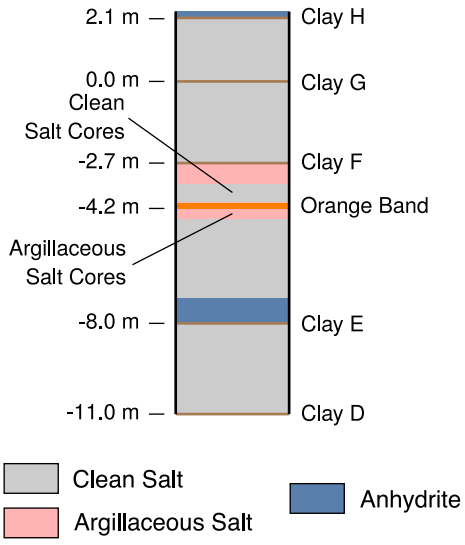


Fig. 13. Core extraction sites with respect to the Deal et al.[63] stratigraphy. (For interpretation of the references to color in this figure legend, the reader is referred to the web version of this article.)

3.2.1. Extraction of 2013 cores

To accommodate the new experiments, Sandia commissioned the drilling of new cores from December 2012 through May 2013.[64] The cores were extracted from the north wall of the N780 Drift, within about 30 m of the intersection with the E140 drift, and along the east rib of the E140 drift, between the N780 and N1100 drifts. This location is marked as the "2013 Core Extraction Site" in Fig. 2. The vertical locations of the drill holes on the wall were selected consistent with the stratigraphy in Figs. 2–2 and 2–3 of Ref. 63. As shown in Fig. 13, the clean salt cores came from above the orange band (Mapping Unit 3 in Ref. 63), and the argillaceous cores came from below the orange band (Mapping Unit 0 in Ref. 63). The shallowest point on any core came from 0.7 m into the rib, and the deepest came from 4.9 m into the rib. The cores were 300 mm in diameter and typically about 600 mm long.

Unfortunately, the Deal et al.[63] stratigraphy around the orange band does not match the 1983 reference stratigraphy[41] or the Munson et al.[6] stratigraphy. (Both the 1983 reference and Munson et al.[6] stratigraphy did not include the orange band, probably to simplify geomechanical modeling.) The Deal et al.[63] stratigraphy is generally similar to the 1983 reference stratigraphy, as can be seen by comparing Figs. 6 and 13, but the 1983 reference stratigraphy designates the salt above and below the orange band as clean. The Munson et al.[6] stratigraphy designates far more salt strata as argillaceous than the Deal et al.[63] stratigraphy, as can be seen by comparing Fig. 13 and the far right schematic in Fig. 9(e). Accordingly, Munson et al.[6] stratigraphy designates the salt above and below the orange band as argillaceous.

Nevertheless, the clean salt above the orange band and argillaceous salt below the orange band are distinct types of salt, even if the differences are not dramatic. A consulting geologist[65] studied the cores

and reported, "The cores from "clean" halite consist of mainly light orange halite up to ≈ 3 cm (≈ 1 inch) [grain] diameter, lesser gray halite, and local very coarse (up to 10 cm; 4 inches [grain diameter]) clear halite. There is little to no discernible clay in the orange halite, and sulfate is estimated to be less than 0.5% by volume. Gray halite locally includes up to 2–3% sulfate with minor clay. Non-halite minerals are unevenly distributed and are principally intercrystalline blebs and films. ... Cores from "argillaceous" halite consist of zones or intervals of (a) relatively fine (< 5 mm; 0.4 inch) light brown or slightly orange halite and (b) coarser (up to 2.5 cm; 1 inch) halite that is more translucent and lighter in color than the fine halite. Overall, the non-halite components in the "argillaceous" halite appear to average ≈ 1% but are higher in coarser halite. The clay proportion dominates in the coarser halite intervals, and sulfate dominates the fine halite intervals. Clay is not uniformly distributed. Some occurs as distinctive irregular blebs between crystals, but clay also forms thin (e.g. 2–3 mm; 0.08-–0.12 inch), irregular, curved, discontinuous stringers". In addition, the Institut für Gebirgsmechanik (IfG) in Germany found the argillaceous salt had, on average, roughly twice the water content of the clean salt by measuring the weight change after flue-curing specimens at 105 °C for 24 h.[26, Fig. 7,28, Fig. 4.2–5]. They presumed the extra water in the argillaceous salt was bound to the clay minerals.

To prepare the cores for shipping, they were placed in wax coated cardboard tubes while still in the underground. The core fit tightly into the tubes with a roughly 2 mm gap around the core annulus. The tube ends were filled with foam packing material, a fitted plastic end cap, and plywood disks to hold the plastic end cap in place. This packaging occurred generally within a week of core extraction and the tubes were wrapped in plastic when shipped. Thus, although the core was not hermetically sealed, it was not exposed to a large volume of dry air.

The cores were sent to the IfG and the Technical University of Clausthal (TUC) in Germany, where the shipment arrived in excellent condition. Salzer et al.[26],Düsterloh et al.[27],Günther et al.[28],Herchen et al.[66] give the details on the petro-physical tests, creep tests, strength tests, and permeability tests they performed. This paper focuses on the IfG's creep tests because the M–D model is most easily calibrated against damage-free creep tests, and the IfG performed 24 creep tests, while the TUC performed only two creep tests. Results from the two TUC creep tests, other TUC creep tests on WIPP core extracted in 2001, and reasons for omitting these TUC creep tests from the M–D model calibration can be found in Ref. 35, Appendix A.5, A.6, and A.7.

3.2.2. Details of the IfG axisymmetric compression creep tests

The axisymmetric creep tests were similar to the example test described in Section 2.1.2. The IfG sub-cored cylindrical test specimens from the 300 mm diameter WIPP cores. After finishing on a lathe, the nominal undeformed specimen diameter and length were $D_0 = 40$ mm and $L_0 = 80$ mm, respectively. By comparison, the grain size in the IfG creep specimens ranged from 2 to 28 mm, with an arithmetic average of 10 mm.[67] The axial compressive displacement u was measured during each test in order to calculate the log strain as $\varepsilon_{zz} = \ln(1 + u/L_0)$. The specimen temperature T was held fixed for each test. The radial Cauchy stress was also held fixed at $\sigma_{rr} = 20$ MPa in order to ensure the specimen remained beneath the dilatancy boundary (remained damage-free) for all applied axial stresses. (See Refs. 26–28, 66 for measurements of the dilatancy boundary.) The axial Cauchy stress σ_{zz}, on the other hand, was only piecewise constant, as indicated by the $\bar{\sigma} = \sigma_{zz} - \sigma_{rr}$ history at the top of Fig. 14. During each constant $\sigma_{zz} = W/A$ stage, the IfG adjusted the axial force W to compensate for the change in cross-sectional area A. To compute A, they assumed the specimen underwent isochoric, affine, deformations such that $A = A_0/(1 - u/L_0)$, where $A_0 = \pi D_0^2/4$.

The IfG tests involved three $\bar{\sigma}$ stages. Each test began with a hydrostatic $\sigma_{rr} = \sigma_{\theta\theta} = \sigma_{zz} = 20$ MPa pressure stage for the first 10 days ($t_{-1} \le t \le t_0$). At the end of the hydrostatic consolidation period, the IfG did not unload or return to room temperature to find the new stress

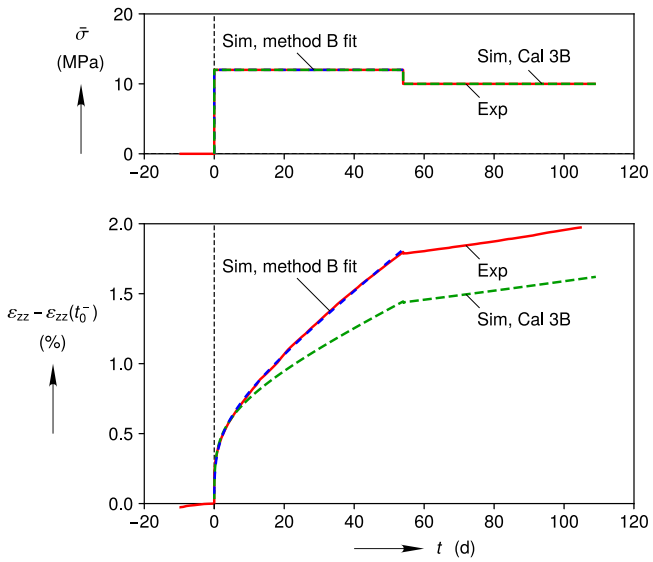


Fig. 14. Stress and strain histories for a axisymmetric compression creep experiment at $T = 60$ °C compared against two simulations.

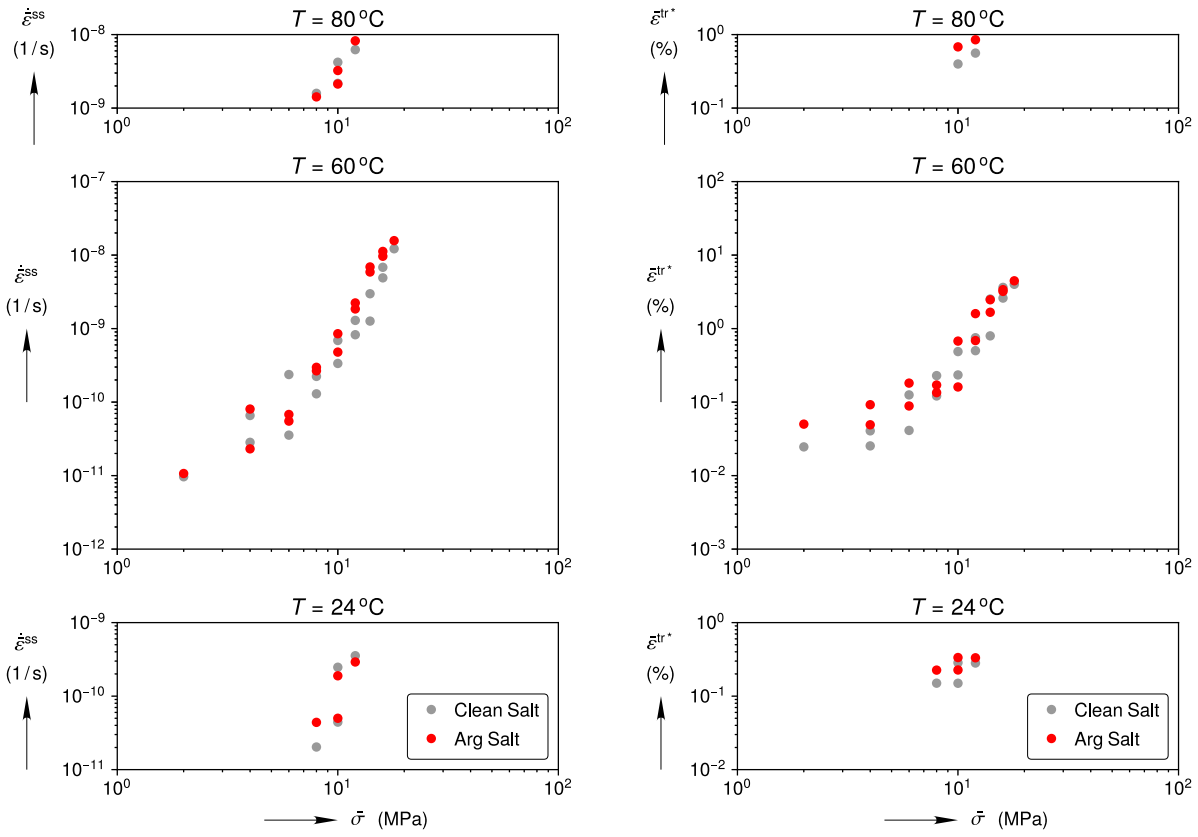
free length. This uncertainty in the stress free length has been removed by plotting $\varepsilon_{zz} - \varepsilon_{zz}(t_0^-)$ instead of ε_{zz}. At $t_0 = 0$, the axial stress σ_{zz} was raised to obtain a non-zero $\bar{\sigma}$. At $t_1 \approx 50$ days, σ_{zz} was changed again by $\Delta\sigma_{zz}(t_1) = \Delta\bar{\sigma}(t_1) = -2$ MPa, which led to a small elastic unloading $\Delta\varepsilon_{zz}(t_1)$, followed by some recovery and a new steady-state strain rate. (The elastic unloading $\Delta\varepsilon_{zz}(t_1)$ is almost imperceptible in Fig. 14 because the creep strain is comparatively large for $\bar{\sigma} = 12$ MPa.) This 2 MPa drop was part of a scheme developed to more accurately bound the steady-state strain rate $\dot{\bar{\varepsilon}}^{ss}$ using reasonable test durations by approaching $\dot{\bar{\varepsilon}}^{ss}$ from "above" and from "below". (See Ref. 68, Section 4 for further details.)

Careful examination revealed $\Delta\varepsilon_{zz}(t_1)$ was consistently too large in the low $\bar{\sigma}$ tests compared to the expected strain jump due to elastic unloading $\Delta\sigma_{zz}(t_1)/E$. This discrepancy was later traced back to a small amount of unwanted axial compliance in the load frame,[69] but it was corrected by calculating the elastic strain due to $\Delta\sigma_{zz}(t_0)$ and $\Delta\sigma_{zz}(t_1)$ using the effective Young's modulus $E^{eff} = \Delta\sigma_{zz}(t_1)/\Delta\varepsilon_{zz}(t_1)$ instead of E to ensure accurate determination of $\bar{\varepsilon}^{tr*}$. See Appendix A.3 of Ref. 35 for further details.

Hydrostatic pressure causes consolidation, which should return the specimen to a more virgin state by healing micro-cracks due to excavating and handling the salt. Although the practice is becoming standard, hydrostatic consolidation was not performed during most legacy experiments on WIPP salt, and the application time can vary from one laboratory to another, even today. The axial strain rate $\dot{\varepsilon}_{zz}$ at the end of this consolidation stage was negligible compared to $\dot{\varepsilon}_{zz}$ for creep stages where $\bar{\sigma} \ge 8$ MPa, but it was often the same order as $\dot{\varepsilon}_{zz}$ for 2 MPa $\le \bar{\sigma} \le 8$ MPa. (The hydrostatic response during $t < t_0$ can be seen for each IfG test in Appendix A.4 of Ref. 35.) In future experiments, the IfG plans to try different techniques to obtain a negligibly small $\dot{\varepsilon}_{zz}$ before applying these smaller $\bar{\sigma}$ values. For now, we simply assume the consolidation strain rate $\dot{\varepsilon}_{con}$ continues to slow down over the course of the creep stages, such that $\dot{\varepsilon}_{con}$ is negligible compared to $\dot{\bar{\varepsilon}}^{ss}$ and ε_{con} is negligible compared to $\bar{\varepsilon}^{tr*}$.

3.2.3. Analysis of IfG axisymmetric compression creep tests

The typical procedure to calibrate the thermo-viscoplastic portion of the M–D model involves two steps. First, one extracts $\dot{\bar{\varepsilon}}^{ss}$, $\bar{\varepsilon}^{tr*}$, and κ values from creep tests at a variety of stresses $\bar{\sigma}$ and temperatures T. Second, one fits model parameters in Eqs. (10), (11), (14) and (17)



(a) Steady-state strain rate (b) Transient strain limit

Fig. 15. Clean salt creep and argillaceous salt creep compared. All data points were obtained from the IfG experiments using fitting method A. (For interpretation of the references to color in this figure legend, the reader is referred to the web version of this article.)

to the collection of $\dot{\bar{\varepsilon}}^{ss}$, $\bar{\varepsilon}^{tr*}$, and κ values. This subsection is concerned with the first step.

Reedlunn[35, Section 3.3] analyzed the IfG creep experiments using two different methods. For the hardening stage ($\bar{\varepsilon}^{tr} < \bar{\varepsilon}^{tr*}$, $t_0 \le t < t_1$), method A measured $\dot{\bar{\varepsilon}}^{ss}$ and $\bar{\varepsilon}^{tr*}$ directly from each creep response curve, while method B fit the MD model to each creep response curve to extract $\dot{\bar{\varepsilon}}^{ss}$, $\bar{\varepsilon}^{tr*}$, and κ_h during hardening. See Figs. 1 and 14 for typical examples of method A and method B, respectively, during the hardening stage. For the recovery stage ($\bar{\varepsilon}^{tr} > \bar{\varepsilon}^{tr*}$, $t_1 \le t < t_2$), both methods measured $\dot{\bar{\varepsilon}}^{ss}$ and $\bar{\varepsilon}^{tr*}$ directly from each creep response curve and did not attempt to extract κ_r values. See Ref. 35, Appendix A.3 for plots of each test, the corresponding model fits, and a table listing all the extracted values. Although both methods produced similar results[35, Fig. 3.6 and 4.1], method A is "model agnostic", making it slightly better for test-to-test comparisons, while method B does not require the creep measurements to fully reach steady-state, making it slightly better for model calibration.

Weighting factors w between 0 and 1 were also assigned by judging the quality of each ε_{zz} versus t curve. Smooth, classical looking, creep curves that appeared close to the steady-state region were assigned $w = 1$, while irregular curves that appeared far from the steady-state region were assigned lower w values. These qualitative weighting factors, which are listed in Table A.2 of Ref. 35, were used in the M–D model recalibrations in Section 3.2.4.

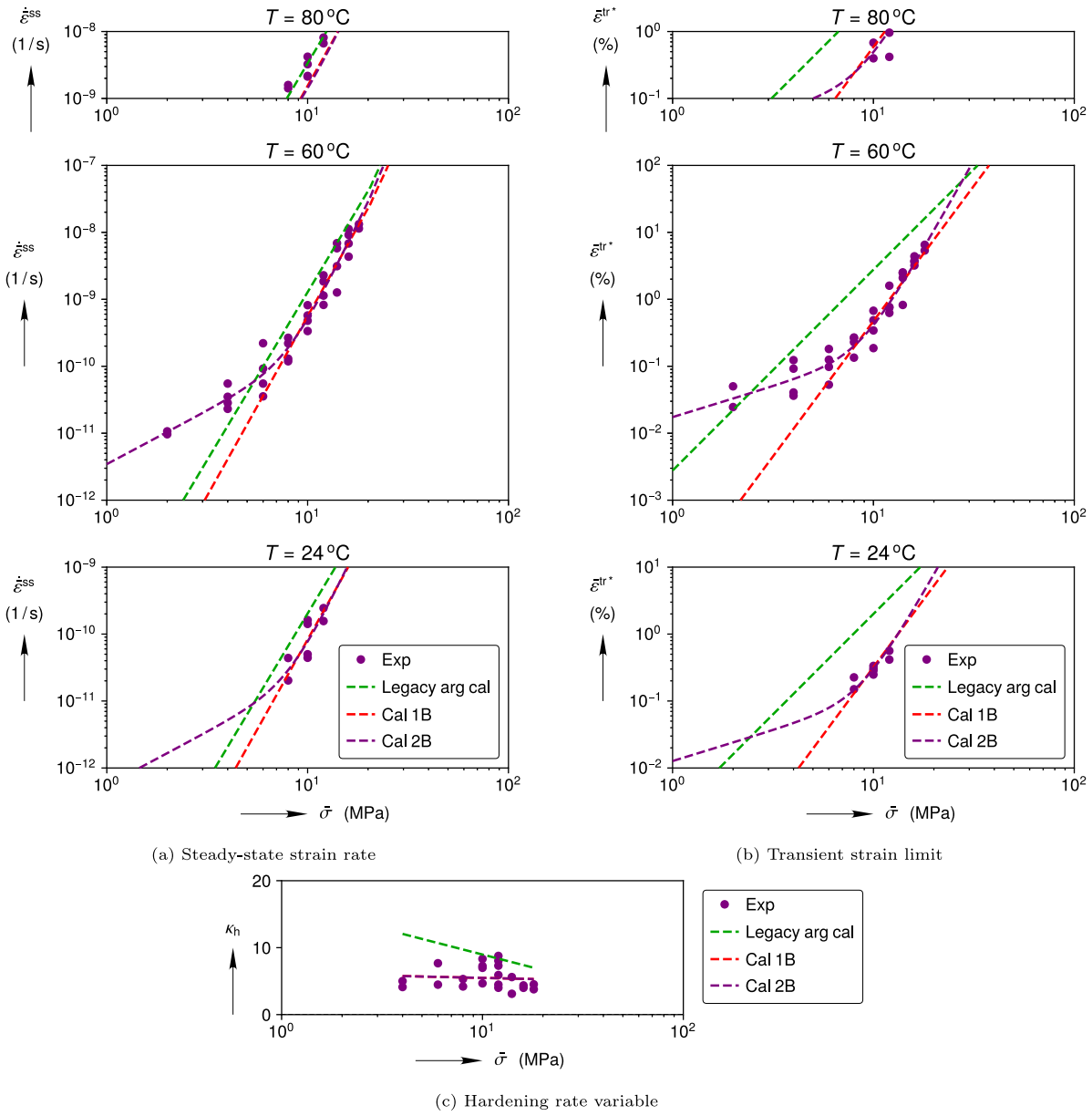
The log–log plots in Fig. 15 show there is almost no difference in the creep behaviors of clean and argillaceous specimens. Fitting method A was utilized here to avoid convolving the creep measurements with the specific form of the M–D model. The majority of the experiments were performed at $T = 60$ °C, but four experiments were performed at 24 °C, and four experiments were performed at 80 °C. (Recall that each IfG experiment applied two values of $\bar{\sigma}$, so four experiments become eight markers in Fig. 15.) A statistical analysis might be able to detect a very slight difference between the clean and argillaceous creep behavior, but it is not large enough to bother distinguishing between the two. Note that Düsterloh et al.[27] performed an independent analysis of the same creep experiments and also concluded that the argillaceous and clean creep responses are virtually the same. Although some uncertainty remains about the creep behavior of clean vs. argillaceous salt (see Section 4.1.4 of Ref. 35), the M–D model calibrations in the following section will not distinguish between the two salt types.

3.2.4. Calibrations 1B and 2B

This section covers the second part of calibrating the M–D model's thermo-viscoplastic response. Model parameters that control the temperature and equivalent stress dependence were recalibrated to the $\dot{\bar{\varepsilon}}^{ss}$, $\bar{\varepsilon}^{tr*}$, and κ_h values extracted using method B in the previous section.

Although this paper is only concerned with the room temperature viscoplastic response of salt, the IfG conducted creep tests at 25, 60, and 80 °C, with most of them at 60 °C. This means the temperature dependence had to still be calibrated to properly capture the room temperature behavior. As discussed in Section 2.1.1, $\dot{\bar{\varepsilon}}^{ss}_0$ and $\dot{\bar{\varepsilon}}^{ss}_2$ dominate at room temperature, but $\dot{\bar{\varepsilon}}^{ss}_1$ begins to play a role at moderately higher temperatures. (The third steady-state mechanism was inactive here because $\bar{\sigma}$ was below Munson et al.'s[6] stress limit for dislocation slip $\bar{\sigma}_0 = 20.57$ MPa in all IfG tests.) The IfG test temperature range was not wide enough to precisely locate where $\dot{\bar{\varepsilon}}^{ss}_1$ began to activate, but a plot of $\ln(\dot{\bar{\varepsilon}}^{ss})$ vs. $1/T$ for the legacy clean salt calibration indicated that $\dot{\bar{\varepsilon}}^{ss}_1$ began to play a role at 80 °C. (Plots of $\ln(\dot{\bar{\varepsilon}}^{ss})$ and $\ln(\bar{\varepsilon}^{tr*})$ vs. $1/T$ can be found in Ref. 23, Fig. 5.1 and 5.2.) Thus, it was safe to assume that $\dot{\bar{\varepsilon}}^{ss}_0$ and $\dot{\bar{\varepsilon}}^{ss}_2$ dominate between 25 and 60 °C.

The first calibration, Calibration 1B, started with the clean salt Legacy Calibration and then modified parameters to fit certain creep



(a) Steady-state strain rate

(b) Transient strain limit

(c) Hardening rate variable

Fig. 16. Three different M–D model calibrations compared against experiments. Experimental data points were obtained using fitting method B. (For interpretation of the references to color in this figure legend, the reader is referred to the web version of this article.)

experiments. Only the low temperature ($T \leq 60$ °C) and medium stress (8 MPa $\leq \bar{\sigma} \leq$ 18 MPa) experiments in Figs. 16(a) and 16(b) were utilized to fit $\dot{\varepsilon}^{\mathrm{ss}}$ and $\bar{\varepsilon}^{\mathrm{tr}*}$. The low stress creep behavior was neglected for Calibration 1B, as that was added to the M–D model only recently. The Nelder–Mead optimization algorithm[70] implemented in Scipy[71] was used to select new values of A_2, Q_2, and n_2 by minimizing the following objective function

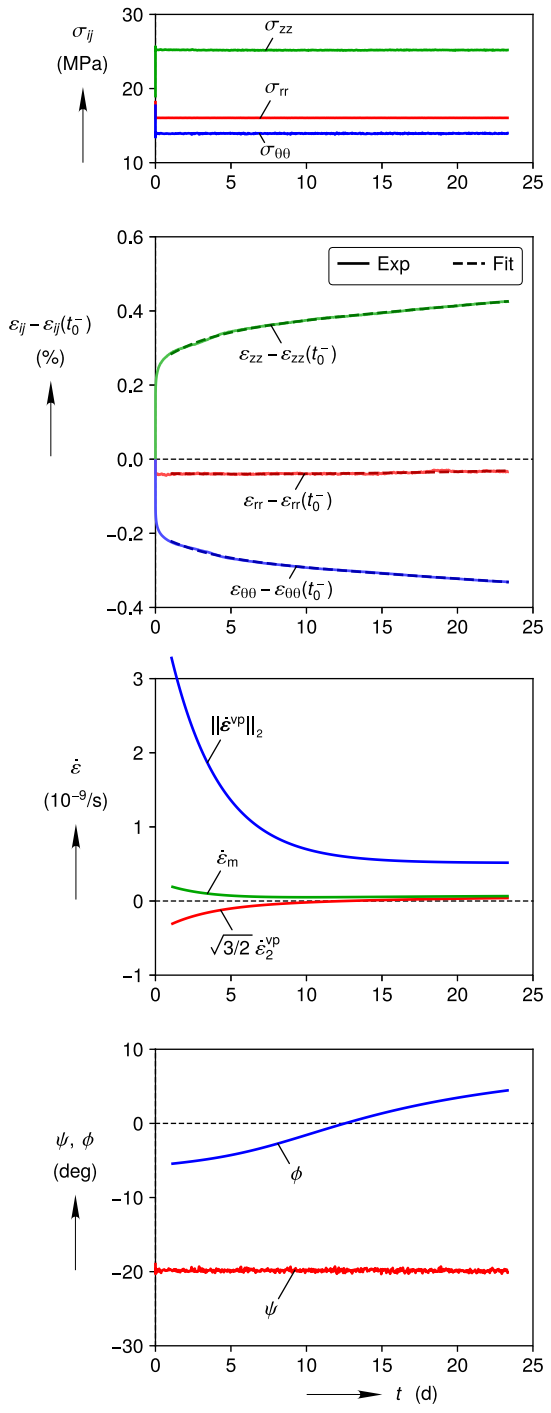
$$r = \sum_{j=1}^{J} \left[w^{(j)} \left(\ln \dot{\varepsilon}^{\mathrm{ss}(j)}_{\mathrm{exp}} - \ln \dot{\varepsilon}^{\mathrm{ss}(j)}_{\mathrm{sim}} \right) + w^{(j)} \left(\log_{10} \dot{\varepsilon}^{\mathrm{ss}(j)}_{\mathrm{exp}} - \log_{10} \dot{\varepsilon}^{\mathrm{ss}(j)}_{\mathrm{sim}} \right) \right]^2, \quad (19)$$

where $\dot{\varepsilon}^{\mathrm{ss}(j)}_{\mathrm{exp}}$ and $\dot{\varepsilon}^{\mathrm{ss}(j)}_{\mathrm{sim}}$ are the experimental measurement and simulated value, respectively, of $\dot{\varepsilon}^{\mathrm{ss}}$ in test segment j, and $w^{(j)}$ is the weighting factor for test segment j (see Section 3.2.3). A similar procedure was utilized to determine K_1, c_1, and m_1. The parameters α_{h} and β_{h} that control κ_{h} were calibrated a little differently, though. The transient rate variable κ_{h} does not depend on temperature, and the experimental values in Fig. 16(c) do not exhibit a discernible kink at low equivalent stresses. Consequently, all the IfG tests were used to select α_{h} and β_{h}. The objective function used to optimize the parameters was

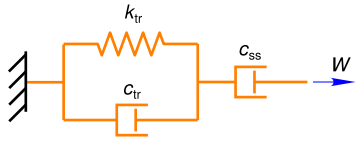
$$r = \sum_{j=1}^{J} \left[w^{(j)} \left(\kappa^{(j)}_{\mathrm{h_{exp}}} - \kappa^{(j)}_{\mathrm{h_{sim}}} \right) \right]^2, \quad (20)$$

where $\kappa^{(j)}_{\mathrm{h_{exp}}}$ and $\kappa^{(j)}_{\mathrm{h_{sim}}}$ are the experimental measurement and simulated value, respectively, of κ_{h} in test segment j. The resulting Calibration 1B parameters can be found in Table 1.

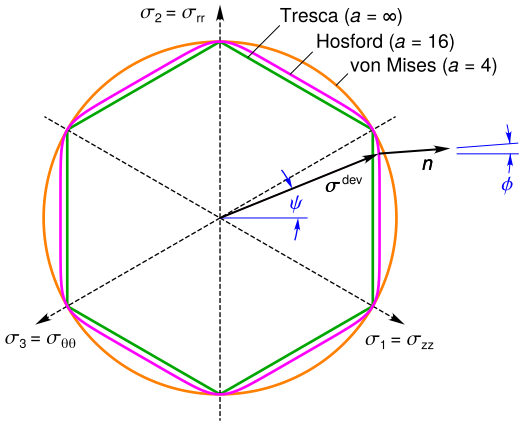
The Calibration 1B fit is graphically depicted in Fig. 16. The argillaceous salt Legacy Calibration is shown for comparison, as opposed to the clean salt Legacy Calibration, because the salt in the rightmost schematic in Fig. 9(e) is mostly argillaceous. As expected, Calibration 1B does not represent the experimental data where $T > 60$ °C or $\bar{\sigma} < 8$ MPa, but it does represent the rest of the experimental data well. The steady-state strain rate slope $n_2 = 5.353$ in Fig. 16(a) is slightly steeper than the legacy $n_2 = 5.0$ and the height of the line is lower. At $\bar{\sigma} = 10$ MPa and $T = 24$ °C, Calibration 1B predicts a 2.4× smaller steady-state creep rate than the Legacy calibration. Most striking, though, is the large difference between Calibration 1B and



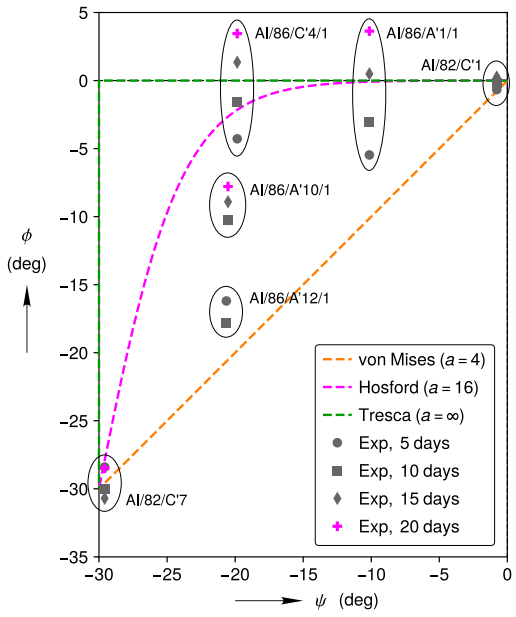
(a) Analysis of hollow cylinder experiment AI/86/C'4/1



(b) Jeffreys element



(c) Hosford surfaces in the π-plane



(d) Hosford exponent a fit

Fig. 17. Determination of the Hosford exponent a. (For interpretation of the references to color in this figure legend, the reader is referred to the web version of this article.)

the Legacy Calibration in Fig. 16(b). At $\bar{\sigma} = 10$ MPa and $T = 24$ °C, Calibration 1B predicts a 6.2× smaller transient strain limit. Lastly, the slope magnitude and height of the Calibration 1B κ_h line, which is identical to the Calibration 2B κ_h line, in Fig. 16(c) are considerably less than those of the argillaceous salt Legacy Calibration.

The second calibration, Calibration 2B, started with Calibration 1B and modified parameters to also fit the $\dot{\bar{\varepsilon}}^{ss}$ and $\bar{\varepsilon}^{tr*}$ measurements at $\bar{\sigma} <$ 8 MPa. In the absence of measurements to determine the temperature sensitivity parameters Q_0 and c_0, they were assumed to be the same as Q_2 and c_1, respectively. Otherwise, the values of A_0, n_0, A_2, $Q_2 = Q_0$, n_2, K_0, m_0, K_1, $c_1 = c_0$, and m_1 were fit in a manner similar to that described above for Calibration 1B. The parameters α_h and β_h were not adjusted. The optimized parameters are listed in Table 1 and the fit is plotted in Fig. 16. The Calibration 2B curves are very similar to those of Calibration 1B for $\bar{\sigma} \geq 8$ MPa, but Calibration 2B predicts far larger $\dot{\bar{\varepsilon}}^{ss}$ and $\bar{\varepsilon}^{tr*}$ for $\bar{\sigma} < 8$ MPa. Calibration 2B's $\dot{\bar{\varepsilon}}^{ss}$ is 6.5× and 24× larger than those predicted by the Legacy Calibration and Calibration 1B, respectively, at $\bar{\sigma} = 3$ MPa and $T = 24$ °C. At the same stress and temperature, Calibration 2B's $\bar{\varepsilon}^{tr*}$ is 1.5× smaller and 14×

larger than that predicted by the Legacy Calibration and Calibration 1B, respectively.

3.2.5. Calibration 3B

The MD model originally used a von Mises equivalent stress, without any facets or sharp corners, but the equivalent stress measure was changed to Tresca by Munson et al.[6] based on the "true triaxial" hollow cylinder experiments of Mellegard et al.[52]. Herein, these same hollow cylinder experiments are re-analyzed and used to fit the Hosford exponent a in Eq. (5).

The Mellegard et al.[52] hollow cylinders were fabricated out of cores extracted from the 150 m level at the International Salt Company Mine in Avery Island, Louisiana. Ideally, the cores would have been extracted from the WIPP site, but something as fundamental as the equivalent stress measure probably should not change from location to location, so the Avery Island cores were considered suitable. The 330 mm diameter cores were machined into 610 mm long hollow cylinders with a 254 mm inside diameter and a 305 mm outside diameter. This corresponds to a 25.4 mm wall thickness and a 5.5 mean radius-to-wall thickness ratio. The mean wall thickness-to-grain size ratio was approximately 3.5. They concluded that 3.5 grains through the thickness was adequate based on inspecting the deformation at several points around the circumference after the experiments.

During the experiments, the internal, external, and axial pressures were independently controlled to reach certain principal stresses, while the internal diameter, external diameter, and axial length were each measured to quantify the resulting principal strains. (See Ref. 52, pg. 19 for the expressions used to calculate the stresses and strains.) Mellegard et al.[52] felt the cylinder wall was thin enough to neglect stress and strain gradients through the thickness and, hence, analyze their results as true triaxial compression at a material point. The same assumption is utilized herein. Each experiment started with a hydrostatic pressure of 18.33 MPa for three days. At $t = t_0 = 0$, the Cauchy radial stress σ_{rr}, hoop stress $\sigma_{\theta\theta}$, and axial stress σ_{zz} were changed to independent values and held constant in time (see, for example, the top plot in Fig. 17(a)). The stress values were chosen to achieve a certain von Mises stress $\bar{\sigma}_{vm}$ and Lode angle ψ, which is defined as

$$\sin\psi = \frac{\sqrt{3/2}\,\sigma_2^{dev}}{\|\boldsymbol{\sigma}^{dev}\|_2}, \tag{21}$$

where $\|\boldsymbol{x}\|_2 = \sqrt{\boldsymbol{x} : \boldsymbol{x}}$ is the L_2 (Euclidean) norm of a generic symmetric second order tensor $\boldsymbol{x}$, $\boldsymbol{\sigma}^{dev} = \boldsymbol{\sigma} - \sigma_m \boldsymbol{I}$ is the deviatoric Cauchy stress tensor, $\sigma_m = \mathrm{tr}(\boldsymbol{\sigma})/3$ is the mean Cauchy stress, and σ_2^{dev} is the intermediate principal deviatoric Cauchy stress. (This Lode angle definition is shown in Fig. 17(c).) The change in radial log strain $\varepsilon_{rr} - \varepsilon_{rr}(t_0^-)$, hoop log strain $\varepsilon_{\theta\theta} - \varepsilon_{\theta\theta}(t_0^-)$, and axial log strain $\varepsilon_{zz} - \varepsilon_{zz}(t_0^-)$ resulting from the change in stress at t_0 were measured and reported (see second from top plot in Fig. 17(a)).

Mellegard et al.[52] may have considered using the variation in the strain rate with respect to ψ to distinguish between the von Mises and Tresca flow potentials. The cores, however, were extracted from two different sites at Avery Island, and one site exhibited significantly higher strain rates than the other site, even for the same ψ. Instead, Mellegard et al.[52] elected to use the angle ϕ of the viscoplastic strain rate $\dot{\boldsymbol{\varepsilon}}^{vp}$ to distinguish between the two flow potentials. The angle ϕ is defined as

$$\sin\phi = \frac{\sqrt{3/2}\,\dot{\varepsilon}_2^{vp}}{\|\dot{\boldsymbol{\varepsilon}}^{vp}\|_2} \tag{22}$$

where $\dot{\boldsymbol{\varepsilon}}^{vp}$ is the viscoplastic logarithmic strain rate tensor and $\dot{\varepsilon}_2^{vp}$ is the intermediate principal viscoplastic logarithmic strain rate. As previously mentioned, the flow rule (Eq. (6)) causes $\dot{\boldsymbol{\varepsilon}}^{vp}$ to be coaxial with the flow potential normal $\boldsymbol{n} = \partial\bar{\sigma}/\partial\boldsymbol{\sigma}$, therefore the angle ϕ is also the angle of $\boldsymbol{n}$. Consider Fig. 17(c) and the dashed lines in Fig. 17(d) (ignore the experimental data for now). For a von Mises flow potential, $\boldsymbol{n}$ is always coaxial with the deviatoric stress $\boldsymbol{\sigma}^{dev}$, such that $\psi = \phi$. For a Tresca flow potential, $\phi = 0°$ for $-30° < \psi < 30°$, and $\phi = \pm 30°$ for $\psi = \pm 30°$. For something in-between von Mises and Tresca, ϕ varies nonlinearly for $-30° < \psi < 30°$. Mellegard et al.[52] ran seven experiments with different values of ψ, ranging from axisymmetric compression ($\psi = -30°$) to pure shear with a superposed hydrostatic stress ($\psi = 0°$). They measured $\dot{\boldsymbol{\varepsilon}}^{vp}$ at the end of each experiment, and calculated seven (ψ, ϕ) value pairs, which led them to conclude the Tresca equivalent stress fit the results better than the von Mises equivalent stress.

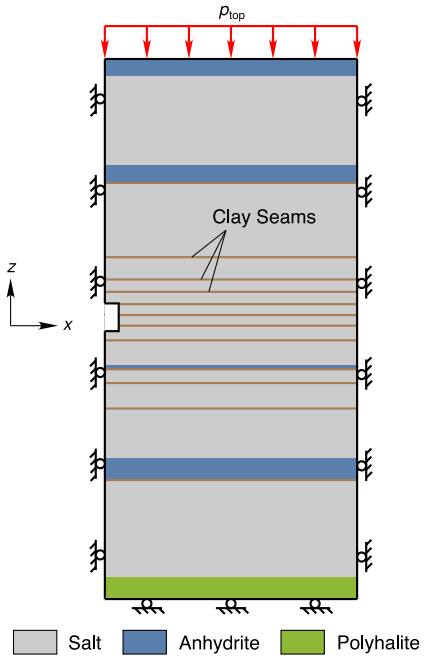
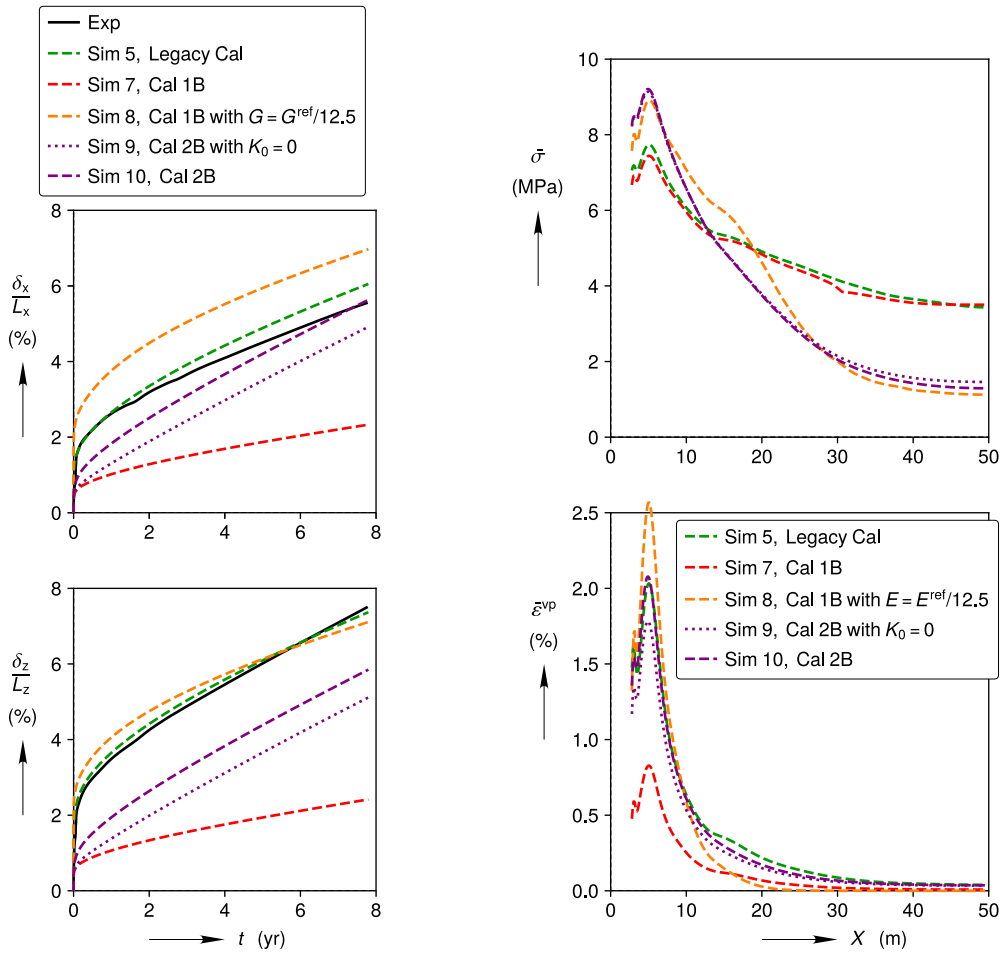


Fig. 18. New stratigraphy and boundary conditions. (For interpretation of the references to color in this figure legend, the reader is referred to the web version of this article.)

Herein, the (ψ, ϕ) value pairs were calculated again from six of the seven experiments in order to fit a. (Experiment AI/86/C′3/1 was discarded due to issues with controlling the stresses.) The analysis of AI/86/C'4/1 is shown in Fig. 17(a) to help visualize the following discussion, but similar plots can be found in Ref. 23, Appendix D for all seven experiments. The Lode angle ψ was calculated as a function of t by substituting the raw values of the principal deviatoric stresses into Eq. (21). Next, each $\varepsilon_{ij} - \varepsilon_{ij}(t_0^-)$ vs. t curve was fit with a simple function to provide a smooth curve for temporal derivatives. The simple function was constructed from a Jeffreys element[72, Section 2.2]. A Jeffreys element (see Fig. 17(b)) consists of a spring (spring constant k_{tr}) in parallel with a dashpot (dashpot constant c_{tr}) for the transient response, which are both in series with a second dashpot (dashpot constant c_{ss}) for the steady-state response. These elements respond to a step change in load W with a displacement $u(t)$ of the form

$$u(t) = p_0 \left[1 - \exp\left(-\frac{t - p_1}{p_2}\right)\right] + p_3\,(t - p_1), \tag{23}$$

where $p_0 = W/k_{tr}$, p_1 is the time when W is applied, $p_2 = c_{tr}/k_{tr}$, and $p_3 = W/c_{ss}$. Eq. (23) was fit to each $(\varepsilon_{ij} - \varepsilon_{ij}(t_0^-))$ vs. t curve, neglecting the first day of creep, by varying the parameters p_j. As shown in the second from top plot in Fig. 17(a), Eq. (23) fit the curves quite well. The fits were then differentiated with respect to time to obtain $\dot{\varepsilon}$. Provided sufficient confining pressure had been applied, the mean strain rate $\dot{\varepsilon}_m = \mathrm{tr}(\dot{\boldsymbol{\varepsilon}})/3$ during creep of rock salt should have ideally been zero. The mean strain rate was small compared to $\|\dot{\boldsymbol{\varepsilon}}\|_2$, but not small compared to $\dot{\varepsilon}_2^{vp}$, as shown in Fig. 17(a). This non-zero



(a) Horizontal and vertical room closure

(b) Stress and strain into wall at $t = 7.8$ yr

Fig. 19. Simulation predictions of Room D's horizontal closure, vertical closure, equivalent stress distribution, and equivalent viscoplastic strain distribution for various M–D model calibrations, ranging from the Legacy Calibration to Calibration 2B. (For interpretation of the references to color in this figure legend, the reader is referred to the web version of this article.)

mean strain rate was assumed to be due to measurement error, so the viscoplastic strain rate tensor $\dot{\boldsymbol{\varepsilon}}^{vp}$ was forced to be isochoric by subtracting off the mean strain rate:

$$\dot{\boldsymbol{\varepsilon}}^{vp} = \dot{\boldsymbol{\varepsilon}} - \dot{\varepsilon}_m \boldsymbol{I}. \tag{24}$$

Once $\dot{\boldsymbol{\varepsilon}}^{vp}$ was computed, ϕ was calculated using Eq. (22).

The values of ψ and ϕ are plotted at five day intervals for each experiment in Fig. 17(d). Multiple values from a given experiment are grouped together and labeled with the experiment ID to aid the reader's eye. The results are reasonably similar to those in Ref. 52, except that one can now see how ϕ evolves with t, instead of a single value per experiment. Unfortunately, a significant amount of variation exists at $\psi = 10°$ and 20°. The numerator $\dot{\varepsilon}_2^{vp}$ in Eq. (22) corresponds to $\dot{\varepsilon}_{rr}$ in these experiments, and ε_{rr} is difficult to accurately measure because it involves the difference between the inner and outer diameter of the hollow cylinder. Furthermore, in experiment AI/86/A′12/1, the magnitude of $\dot{\varepsilon}_{rr}$ mysteriously increased (instead of slowly decreasing) at $t = 12.5$ days (see Fig. D.2b of Ref. 23). Mellegard et al.[52] noted this anomaly, but they did not determine the cause. Experiment AI/86/A′12/1 ended at $t = 16.9$ days.

Despite these issues, the authors were not aware of a better experimental data set to calibrate a against, so it was used for Calibration 3B. For a given value of a, the angle of the Hosford flow potential normal $\boldsymbol{n}$ was computed using

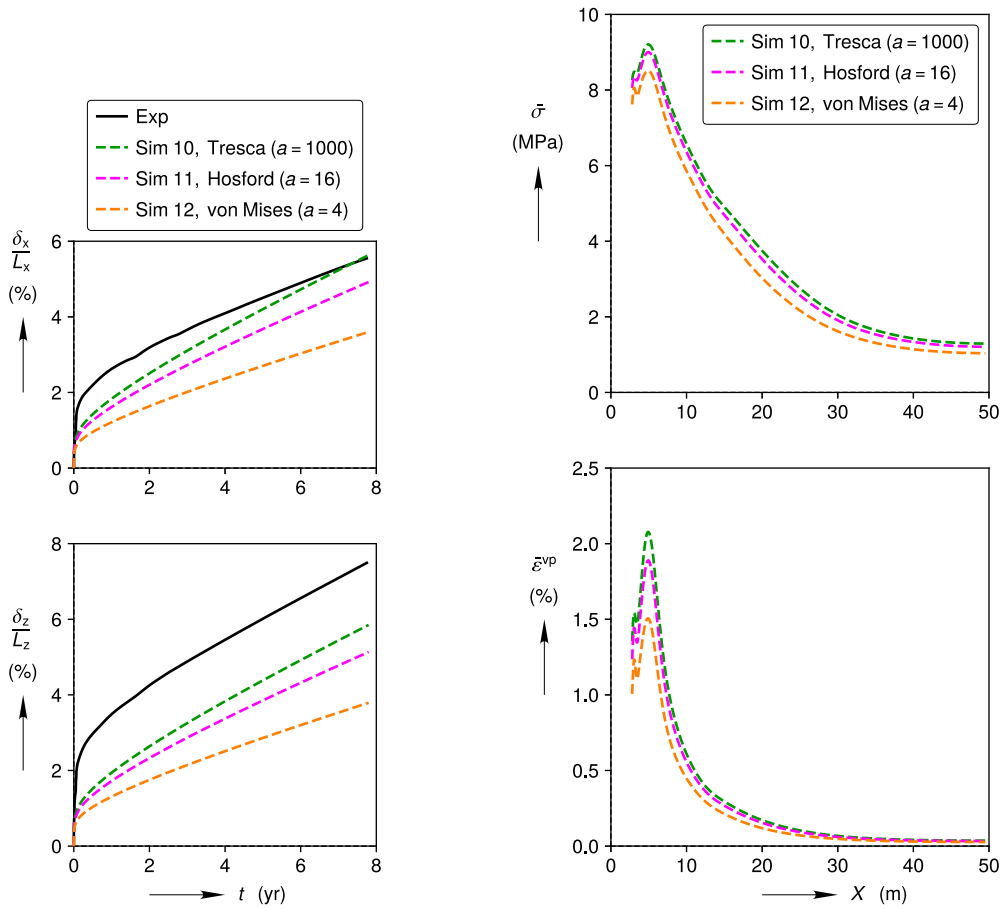
$$\sin\phi = \frac{\sqrt{3/2}\, n_2}{\|\boldsymbol{n}\|_2}. \tag{25}$$

A least squares fit of a against the $t = 20$ day experimental data set, which does not include AI/86/A′12/1, resulted in $a = 16$. The $a = 16$ surface is plotted in Figs. 17(c) and 17(d) for reference.

3.3. Effect of M-D model calibrations

This section investigates how the three new M–D model calibrations impact predictions of Room D's closure. To be consistent with the new calibrations, Fig. 18 depicts a new stratigraphy that does not distinguish between clean and argillaceous salt. This stratigraphy was utilized in all the Calibration 1B, 2B, and 3B simulations, including those whose results are plotted in Figs. 19 and 20. Fig. 19 considers a step-by-step evolution from the M–D model Legacy Calibrations to Calibration 2B, while Fig. 20 shows the impact of the Hosford exponent. Both figures depict predictions of room closure against the experimental measurements, and also depict $\bar{\sigma}$ and $\bar{\varepsilon}^{vp}$ at room mid-height versus X at the end of the simulations ($t = 7.8$ yr) to help explain the room closure predictions. Plots of $\bar{\sigma}$ and $\bar{\varepsilon}^{vp}$ versus Z show similar trends, but they are not shown because the intersecting anhydrite and clay seam strata make those curves less easy to read. Note, uppercase $\{X, Y, Z\}$ are used to indicate the position in the reference (undeformed) configuration, as opposed to the position $\{x, y, z\}$ in the current (deformed) configuration.

The differences between the Legacy Calibration and Calibration 1B room closure predictions in Fig. 19(a) show the dramatic impact of



(a) Horizontal and vertical room closure

(b) Stress and strain into wall at $t = 7.8$ yr

Fig. 20. Simulation predictions of Room D's horizontal closure, vertical closure, equivalent stress distribution, and equivalent viscoplastic strain distribution for various Hosford exponents. (For interpretation of the references to color in this figure legend, the reader is referred to the web version of this article.)

recalibrating $\dot{\bar{\varepsilon}}^{ss}$ and $\bar{\varepsilon}^{tr*}$ against the IfG medium stress creep experiments. Switching to Calibration 1B (Simulation 5 to 7) reduced δ_x/L_x and δ_z/L_z by 0.38× and 0.33×, respectively, at $t = 7.8$ yr. Fig. 19(b) shows that Calibration 1B predicts far less $\bar{\varepsilon}^{vp}$ than the Legacy Calibrations, yet the two calibrations yield similar $\bar{\sigma}$ vs. X distributions. The reader may recall a similar under-prediction of room closure with the reference moduli in Fig. 8. The similarities between the Calibration 1B predictions and the reference moduli predictions probably is not a coincidence, since both material models were faithfully calibrated against medium stress creep experiments, without any speculative parameter adjustments. To investigate further, Calibration 1B's shear modulus was reduced from $G = G^{ref} = 12.4$ GPa to $G = G^{ref}/12.5 = 0.992$ GPa, similar to the reduced moduli predictions in Fig. 8. (In addition, A_i was divided by 12.5^{n_i}, q was divided by 12.5, $\beta_h \log_{10}(12.5)$ was added to α_h, and K_i was divided by 12.5^{m_i} to compensate for the G in the denominator in Eqs. (10), (11), (14) and (17).) Fig. 19(a) shows this shear modulus reduction produces a large increase in room closure (compare the predictions of Simulation 7 to 8), just as seen in Fig. 8, and substantially alters the $\bar{\sigma}$ and $\bar{\varepsilon}^{vp}$ distributions in Fig. 19(b).

Fortunately, one does not need to resort to non-physical shear modulus reductions anymore, because including the creep behavior at low stresses vastly improves the room closure predictions in Fig. 19(a). Simulation 9 utilizes the low stress steady-state strain rate behavior, without the low stress transient strain behavior, while Simulation 10 includes both effects. The low stress steady-state strain rate dramatically increases the closure rates at $t = 7.8$ yr by 3.1×, while the low stress transient strain has a smaller, yet significant, effect on closures accumulated during $0 < t \leq 2$ yr. Interestingly, the $\bar{\sigma}$ and $\bar{\varepsilon}^{vp}$

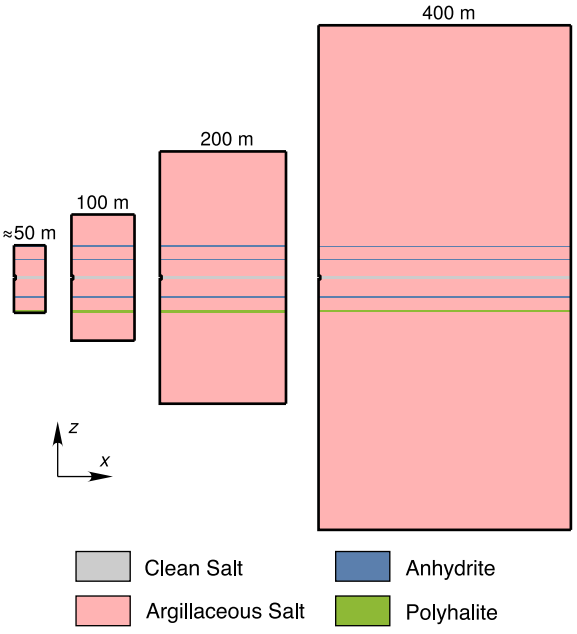
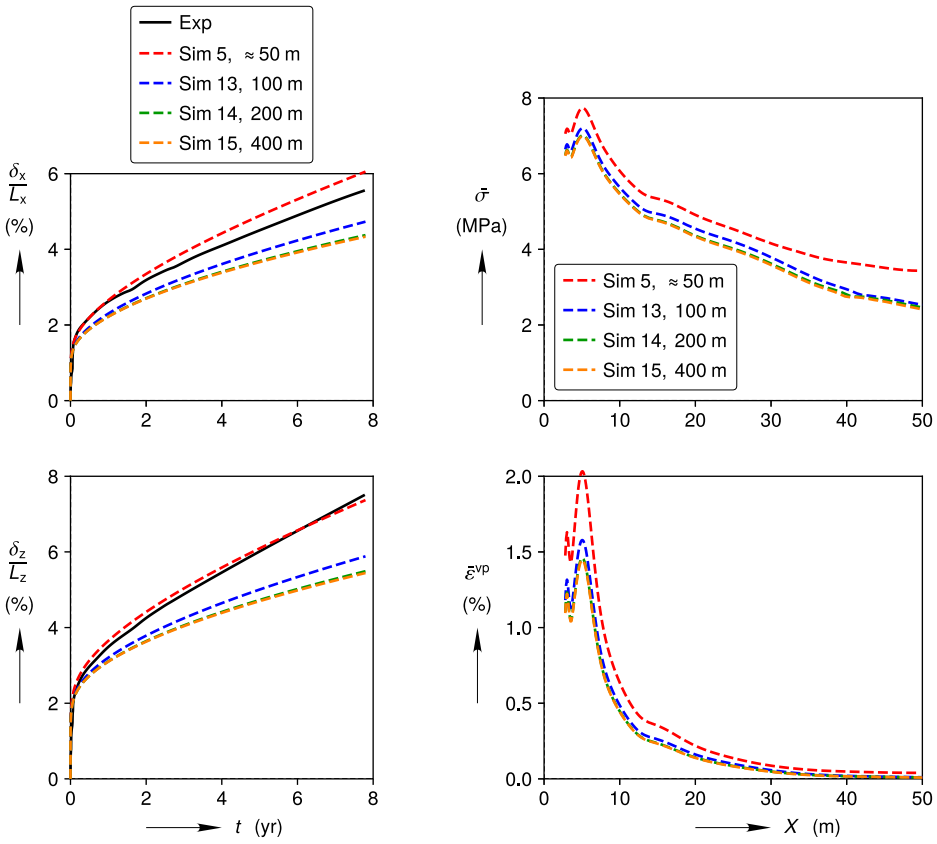


Fig. 21. Domain sizes for Legacy Calibration domain size study. (The Calibration 3B domain size study in Fig. 23 utilized the same domains, except the Calibration 3B study did not distinguish between clean salt and argillaceous salt.) (For interpretation of the references to color in this figure legend, the reader is referred to the web version of this article.)



(a) Horizontal and vertical room closure

(b) Stress and strain into wall at $t = 7.8$ yr

Fig. 22. Simulation predictions of Room D's horizontal closure, vertical closure, equivalent stress distribution, and equivalent viscoplastic strain distribution for various domain sizes using the Legacy Calibrations. (For interpretation of the references to color in this figure legend, the reader is referred to the web version of this article.)

distributions in Fig. 19(b) with the low stress behavior (Simulations 9 and 10) look quite similar to those with the reduced shear modulus (Simulation 8): the far-field $\bar{\sigma}$ at $X = 50$ m is relatively low, the near-field $\bar{\sigma}$ at $X = 5$ m is relatively high, and the near-field $\bar{\varepsilon}^{vp}$ is relatively large. In a certain sense, reducing the shear modulus by 12.5× may not have been as ill-conceived an idea as once thought. On the other hand, the physically-based low stress creep behavior is obviously the preferred approach now that ample experimental evidence exists to support it.

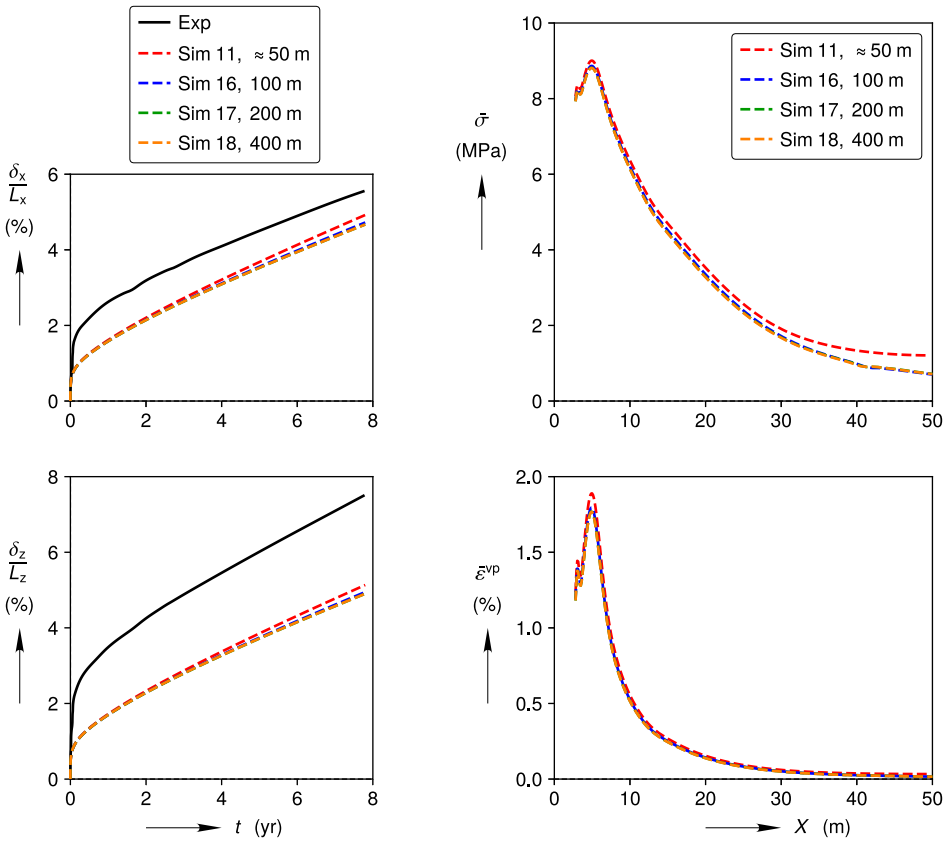
The sensitivity of room closure to the Hosford exponent a is shown in Fig. 20(a). As one might expect from Eqs. (10), (11) and (17), transitioning from the Tresca stress to the von Mises stress causes smaller $\bar{\sigma}$ and smaller $\bar{\varepsilon}^{vp}$, which results in smaller room closure predictions. Of the three cases considered in Fig. 20(a), the Calibration 3B value of $a = 16$ (Simulation 11) appears to give the best closure rate predictions, although all cases under-predict the amount of closure during $0 < t \leq 50$ days.

3.4. Domain size

Fig. 19(b) showed that including the low stress creep behavior reduces the far-field $\bar{\sigma}$, which turns out to have ramifications for domain size convergence. Thus far, the top, bottom, left, and right domain boundaries have been $D \approx 50$ m (see Section 2.2.2 for exact values) away from the center of Room D. These domain boundaries were established in the 1980's, but they may be too close. To find the minimum domain size that does not affect the room closure predictions, simulations were performed with $D = 100$ m, 200 m, and 400 m domain sizes (see Fig. 21), while adjusting p_{top} and the initial lithostatic stress according to the uniform rock density of $\rho = 2800$ kg/m^3. The Legacy Calibration domain size study assumed the rock above and below the original $D \approx 50$ m boundaries was entirely argillaceous salt, as shown in Fig. 21, while the Calibration 3B domain size study assumed the same rock was simply salt, since Calibration 3B does not distinguish between clean and argillaceous salt. The actual geology beyond the $D \approx 50$ m domain includes salt, anhydrite, polyhalite, and clay seams, but salt is still the most common rock.[73,74] Appendix A.2 details how the maximum relative residual $\hat{R}_{max}$ was selected as D was varied.

The Legacy Calibration room closure predictions in Fig. 22(a) are significantly more sensitive to D than the Calibration 3B room closure predictions in Fig. 23(a). The Legacy Calibration room closure predictions with $D \approx 50$ m (Simulation 5), closely agree with the experimental measurements in Fig. 22(a), but increasing the domain size to $D = 400$ m (Simulation 15) causes the closure and closure rate to converge to significantly smaller values. This result shows the closeness of the Legacy Calibration $D \approx 50$ m predictions to the measurements was just a coincidence. Conversely, increasing the domain size from $D \approx 50$ m to 400 m causes the Calibration 3B room closure predictions in Fig. 23(a) to converge to only slightly smaller values. The difference in domain size sensitivity can be explained by the $\bar{\sigma}$ distributions. Increasing the domain size to $D = 400$ m causes $\bar{\sigma}$ to approach zero at $X = 400$ m for both calibrations, as expected, but the low stress creep behavior in Calibration 3B leads to much lower $\bar{\sigma}$ values at $X = 50$ m in Fig. 23(b) than with the Legacy Calibrations in Fig. 22(b). In other words, having the boundaries too close to the room artificially increases $\bar{\sigma}$, which leads to artificially greater room closure, but these artificial increases are much less significant if $\bar{\sigma}$ is already close to zero at the boundary.

The preceding domain size convergence study treated Room D as completely isolated, but, as shown in Fig. 4(a), Room A3 is only 85.3 m away on Room D's left side. Including the Room A series in this domain



(a) Horizontal and vertical room closure

(b) Stress and strain into wall at $t = 7.8$ yr

Fig. 23. Simulation predictions of Room D's horizontal closure, vertical closure, equivalent stress distribution, and equivalent viscoplastic strain distribution for various domain sizes using Calibration 3B. (For interpretation of the references to color in this figure legend, the reader is referred to the web version of this article.)

size convergence study was considered, but ultimately abandoned for three reasons. First, the Room A series was heated, which would have added considerable complexity to the simulations. Second, if the Room A series substantially altered Room D's closure, one would expect a discernible change in the measured Room D δ_x/L_x and δ_z/L_z histories when Room A1, A2, and A3 excavations began ($t = 0.49$, 0.28, and 0.57 yr in Fig. 23(a), respectively)[45] or when the heaters were turned on ($t = 1.53$ yr in Fig. 23(a))[45], yet such a change is not plainly evident at these times in Fig. 23(a). Third, the Calibration 3B room closure predictions are relatively insensitive to D for $D \geq 50$ m, so treating Room D as isolated may be a reasonable model simplification when the low stress creep behavior is included.

3.5. Further comparisons

The predicted Room D horizontal and vertical closure rates match the measured closure rates reasonably well in Fig. 23(a), but Room D is only one experiment, so Rooms G and Q (see Section 2.2.1) were simulated as well. Rooms G and Q, unlike Room D, can be considered truly isolated because the nearest drifts were more than 200 m away during these experiments (see Fig. 2). The Room G and Room Q models were quite similar to the Simulation 17 (Room D) model, utilizing M–D model calibration 3B, $D = 200$ m, all clay seams, and the new stratigraphy in Fig. 18. The Room G corners were sharp ($L_r = 0$), similar to the Room D model, while the Room Q cross-section was circular ($L_r = L_x/2 = L_z/2$). Details of the Room G and Q numerical setups can be found in Appendix A.4.

In addition, simulations of Room D, G, and Q were performed using a Stone[60] type model setup. Recall from Section 2.2.5 that Stone's[60] simulations utilized the legacy M–D model calibrations, ignored all clay seams, and replaced all anhydrite and polyhalite, except marker bed 139 and anhydrite "a", with argillaceous salt. Also recall that Stone's[60] simulations generated the official WIPP porosity response surface. The Stone[60] type Room D, G, and Q simulations in this paper utilized $D = 400$ m, based on the results in Fig. 22, and an associated flow rule for the anhydrite. Details of the Stone[60] type numerical setup be found in Appendix A.3.

The comparisons between the predicted and measured Room D, G, and Q closures are shown in Fig. 24. The experimental measurements correspond to mining sequence Station −1.4 m, −1.0 m, and −3.7 m in Room D, G, and Q, respectively. In all three cases, the Stone[60] type simulations (Simulations 19, 20, and 21) more closely capture the closure histories during $0 < t < 1$ month, but the simulations that utilize the current model setup developed herein (Simulations 17, 22, and 23) capture the closure rates for $t > 1$ month more accurately. Averaged across the three rooms at $t = 5.7$ yr, switching to the current model caused the $\dot{\delta}_x / L_x$ under-prediction to reduce from 2.24× to 0.87× (a 1.15× over-prediction) and the $\dot{\delta}_z / L_z$ under-prediction to reduce from 2.72× to 1.08×.

The closure rate improvements from the Ref. 60 type model setup to the current model setup are substantial for two reasons. First, accurate predictions of long-term closure rates are far more important than predictions of the short-term closures because these models are typically used to extrapolate forward by tens to hundreds of years. Second, the current model setup has a stronger scientific foundation, meaning it will more likely capture the closure rates at other WIPP locations, and the general modeling approach should be more applicable at a different salt repository.

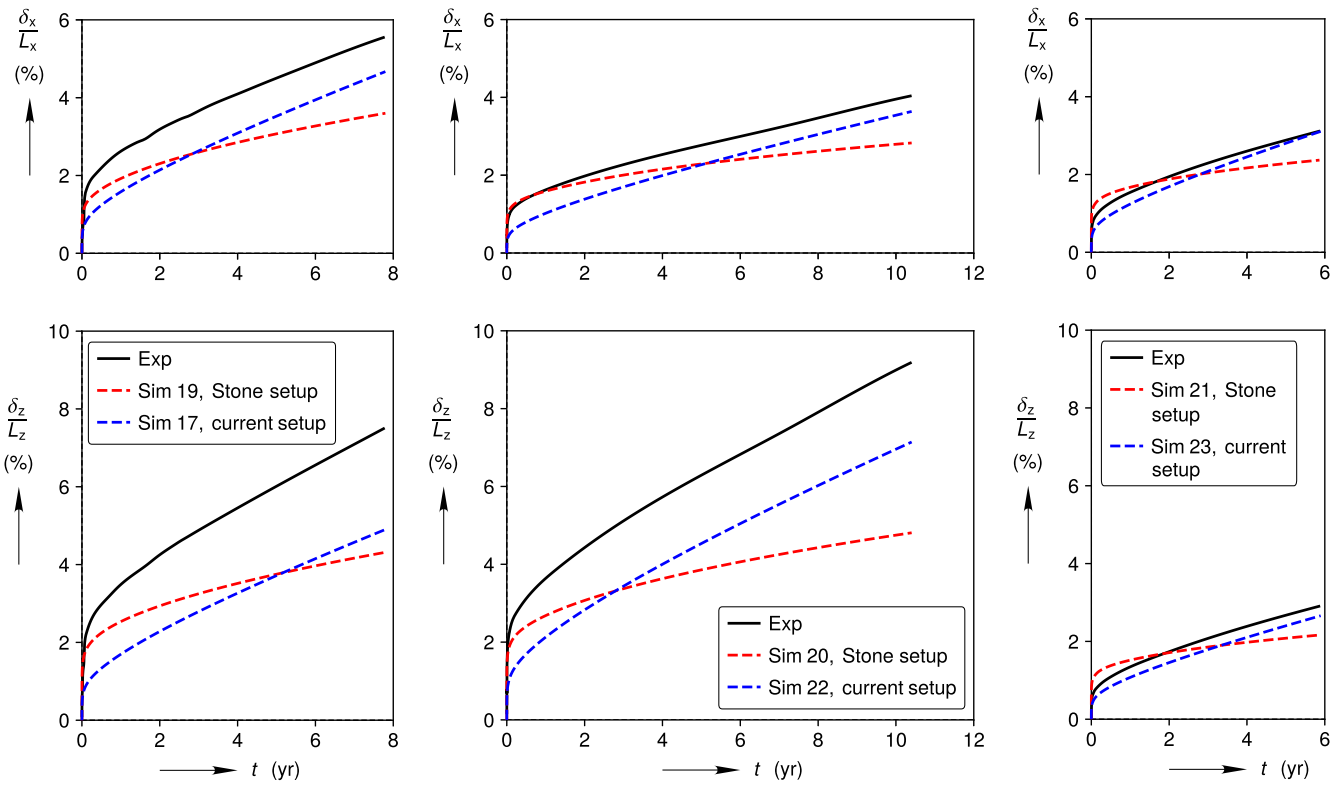


Fig. 24. Simulation predictions of Room D, G, and Q horizontal and vertical closure compared against experimental measurements. (For interpretation of the references to color in this figure legend, the reader is referred to the web version of this article.)

4. Summary

Accurate geomechanical models of room closure are important for salt repository design, operations, and long-term performance. During the 1980's and 1990's, Munson and co-workers developed geomechanical models and compared their predictions against several WIPP room closure experiments, including Room D. The models produced closures that agreed quite well with the experimental measurements, but the models involved speculative modifications, they were not always consistent with one another, and the numerical details were not documented. These adjustments and inconsistencies were disclosed when the models were first presented, but they were not mentioned in Munson's capstone paper.[7]

Concerns about the Munson models for room closure prompted the reinvestigation in this paper. After approximately recreating Munson's legacy Room D simulation, the numerical settings were tightened based on convergence studies, which increased the closure predictions by about 1.36× at $t = 7.8$ yr. Next, reintroducing the anhydrite (and polyhalite) layers reduced the closure predictions by roughly 0.70× at $t = 7.8$ yr, which, coincidentally, brought the predictions back into alignment with the Room D measurements. Faithfully recalibrating the M–D model, however, against a battery of new medium stress ($8 < \bar{\sigma} \leq 18$ MPa) creep experiments on WIPP salt caused a Room D simulation to under-predict the horizontal and vertical closure rates by 2.34× and 3.10×, respectively, at $t = 5.7$ yr. Recalibrating the M–D model further against new low stress ($\bar{\sigma} < 8$ MPa) creep experiments and true triaxial creep experiments, produced closure predictions that miss the transient closure during $0 < t \leq 0.2$ yr, but reasonably capture Room D's closure rates for $0.2 < t \leq 7.8$ yr. A subsequent domain size convergence study showed that the low stress creep behavior in the latest M–D model calibration made it far less sensitive to the domain size than the legacy M–D model calibration. Finally, simulations of Room D, G, and Q led to a 1.15× over-prediction of horizontal closure rates and a 1.08× under-prediction of vertical closure rates at $t = 5.7$ yr, averaged across the three rooms.

Despite these favorable predictions of room closure rates, several areas of uncertainty remain. Salt constitutive model improvements, such as adding damage, improving the transient hardening behavior, improving the low stress creep measurements, and a more thorough understanding of argillaceous and clean salt behavior, could alter the closure predictions. Non-salt improvements, such as developing a clay seam model based on direct experimental measurements (rather than qualitative observations and engineering judgement) and improving the anhydrite model, could also affect the closure predictions. Further areas for refinement could be revealed by simulating the multi-pass excavation process, nearby parallel drifts, or more complex three-dimensional stress states at drift intersections.

On the other hand, complex structural simulations almost always include some level of uncertainty. The model arrived at herein is based on laboratory test data, underground observations, and forthright assumptions where necessary. It produces closure rate predictions that compare favorably against three relevant underground experiments, and appears sufficiently predictive for careful engineering use.

Declaration of competing interest

The authors declare that they have no known competing financial interests or personal relationships that could have appeared to influence the work reported in this paper.

Acknowledgments

The authors gratefully acknowledge the assistance of several individuals. First, James Bean, Courtney Herrick, Michael Schuhen, William Scherzinger, Edmundo Corona, Brian Lester, and Steven Sobolik at Sandia gave advice on implementing material models, tips for running simulations, and information about the WIPP. Second, former Sandians, Harold Morgan and Charles Stone, provided historical context for the studies from the 1980's and 1990's. Third, Kirby Mellegard, Kerry DeVries, Stuart Buchholz, and Leo Van Sambeek at

RE/SPEC gave thoughtful suggestions during an informal review. Last, but not least, the authors acknowledge our German Colleagues from Joint Project III: Andreas Hampel, Klaus Salzer, Ralf-Michael Günther, Christoph Lüdeling, Karl-Heinz Lux, Kai Herchen, Joachim Stahlmann, Andreas Gährken, Christian Missal, Savas Yildirim, Kurt Staudtmeister, Alexandra Pudewills, Till Popp, Uwe Düsterloh, and Dirk Naumann. They generously ran experiments, shared their knowledge, and hosted us on our visits to Germany.

Sandia National Laboratories is a multi-mission laboratory managed and operated by National Technology and Engineering Solutions of Sandia, LLC., a wholly owned subsidiary of Honeywell International, Inc., for the U.S. Department of Energy's National Nuclear Security Administration under contract DE-NA0003525. This research is funded by WIPP programs administered by the Office of Environmental Management (EM) of the U.S. Department of Energy. This paper describes objective technical results and analysis. Any subjective views or opinions that might be expressed in the paper do not necessarily represent the views of the U.S. Department of Energy or the United States Government.

Appendix A. Numerical setups

The numerical setups for the simulations in Table 3a are discussed in this section. Appendix A.1 starts by detailing the numerical settings used to recreate the legacy simulation of Room D (Simulation 1). Appendix A.2 discusses a series of changes to improve the numerical robustness and accuracy of the Room D closure simulations. Appendix A.3 presents the numerical setup for the Stone[60] type simulations of Rooms D, G, and Q. Appendix A.4 covers the improved numerical setup for the Room G and Q simulations.

A.1. Numerical setup for recreated legacy room D simulations

Munson et al.[6] neglected to mention any of their numerical settings, so a number of educated guesses were made for Simulation 1. The finite element mesh was made to match the Room B pretest mesh in Ref. 75, Fig. 7 with an element width of $H = L_x/12$ near the room, as shown in Fig. A.25(a). The mesh was a single layer of hexahedral elements because Sierra/SolidMechanics[36] does not have two-dimensional plane strain elements. As such, the y displacements (into the page) of the front and back surfaces of the single layer were held to zero. The layer's y thickness was 5.5/48 m, which would be irrelevant, except it determines the magnitude of the forces along the domain boundaries. Sierra/SolidMechanics's[36] computationally inexpensive, mean quadrature (MQ) element, with an hourglass stiffness of 0.005, was utilized throughout the domain because Stone[60] used this element and hourglass stiffness in his SANTOS simulations. An implicit multi-level solver[36] was used to solve the discretized equilibrium equations. The inner loop utilized a conjugate gradient solver for the equilibrium equations, with the contact interactions held fixed. The outer loop utilized a kinematic enforcement algorithm to resolve the contact interactions, with the nodal displacements outside of the contact zone held fixed. Sierra/SolidMechanics[36] accepted a solver solution as converged if

$$\frac{\sqrt{\boldsymbol{R}\cdot\boldsymbol{R}}}{\sqrt{\boldsymbol{F}^{\mathrm{r}}\cdot\boldsymbol{F}^{\mathrm{r}}}} = \hat{R} \le \hat{R}_{\max}. \tag{A.1}$$

where $\boldsymbol{R}$ is the residual from the discretized equilibrium equations, $\boldsymbol{F}^{\mathrm{r}}$ is the reaction force vector at nodes whose displacements were prescribed, and $\hat{R}_{\max}$ is the user specified maximum value of the relative residual norm $\hat{R}$. The tolerance on the outer loop relative residual norm was $\hat{R}_{\max} = 10^{-3}$. The initial time step at $t = 0$ was $\Delta t = 10^{-6}$ s, but this was allowed to grow as much as $\gamma = 5\%$ per time step.

A.2. Improvements to Room D numerical setup

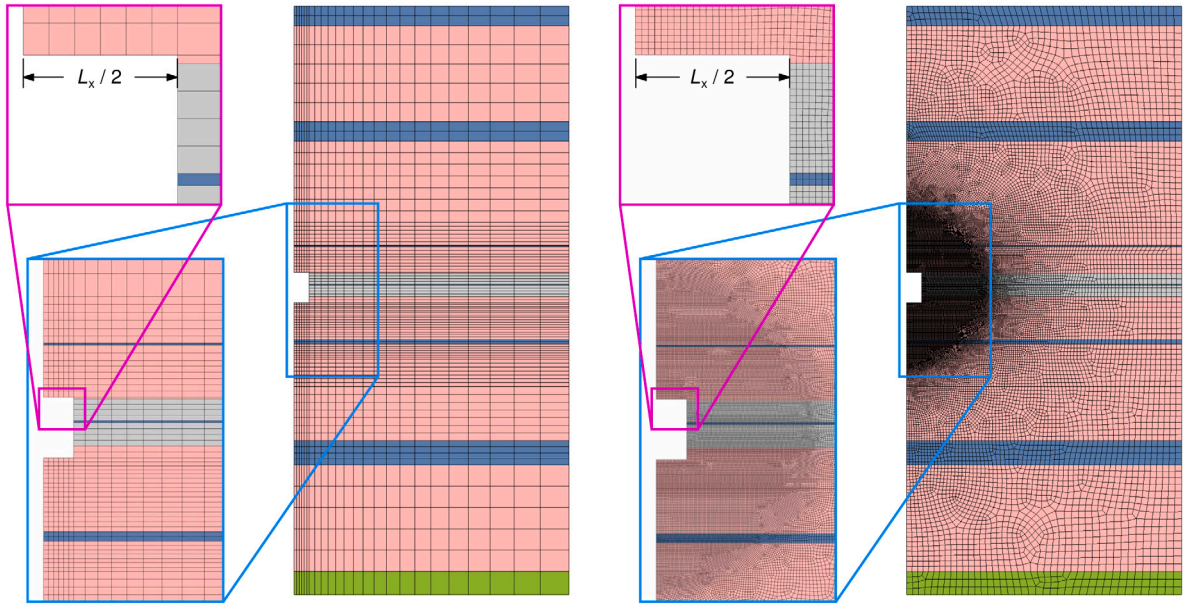
Two strings of numerical improvements to the Room D numerical setup were pursued. The first string of improvements stem from a preliminary study in Section 2.2 of Ref. 35. The second string of studies involved convergence studies to pick numerical settings that would produce the desired level of accuracy without unnecessary computational cost.

The first string of improvements were the following.

1. The element formulation was changed from the MQ element to the selective deviatoric (SD) element, with the deviatoric parameter set to 1 and strongly objective strain incrementation. The MQ element is faster because it under-integrates the element response, yet one must select an hourglass stiffness, similar to a single integration point element. The hourglass forces approach zero with sufficient mesh refinement, but they can be significant with coarse meshes. The SD element, on the other hand, is more accurate because it fully integrates the deviatoric response, while still under-integrating the volumetric response to avoid pressure locking, similar to a Q1P0 element. Typically, the SD element is not much slower for implicitly solved problems because integrating the element response is relatively quick compared to solving the linearized equilibrium equations.
2. The mesh was completely rebuilt using Cubit's Python scripting environment.[76] A comparison of the legacy mesh and the new mesh after the convergence studies is shown in Fig. A.25. The new mesh in Fig. A.25(b) clearly has more elements, especially near the room, and coarsens to larger elements further from the room.
3. The contact enforcement algorithm was changed from the Kinematic algorithm to the Augmented Lagrange (AL) algorithm in Sierra/SolidMechanics. The Kinematic algorithm guarantees that bodies do not interpenetrate, and iterates on the position of the interface to balance the forces until $\hat{R} \le \hat{R}_{\max}$ has been met. The AL algorithm guarantees force equilibrium across the contact interface and iterates on the force magnitude to reduce the interpenetration until $\hat{R} \le \hat{R}_{\max}$ has been met. The AL algorithm is currently the default contact enforcement algorithm in Sierra/SolidMechanics because it is typically more robust.
4. The recreated legacy simulation (Simulation 1) instantaneously excavated the room as a void at $t = 0$, which caused the stress surrounding the room to jump from lithostatic to highly deviatoric in a single time step. When this approach was tried on finer meshes, the conjugate gradient solver sometimes would not converge. To avoid this issue, the instantaneous excavation was spread out over multiple time steps by applying a time-varying fluid pressure to the surfaces of the room. At $t = -10$ ms, the fluid pressure varied linearly from the top to the bottom of the room according to the lithostatic pressure that existed prior to excavating the room. Then the fluid density was ramped down to zero between $t = -10$ ms and $t = 0$. For $t > 0$, the fluid pressure was held to zero. A small time step of $\Delta t = 1$ ms was required during the fluid pressure ramp down, but it was reset to $\Delta t = 1$ s at $t = 0$.

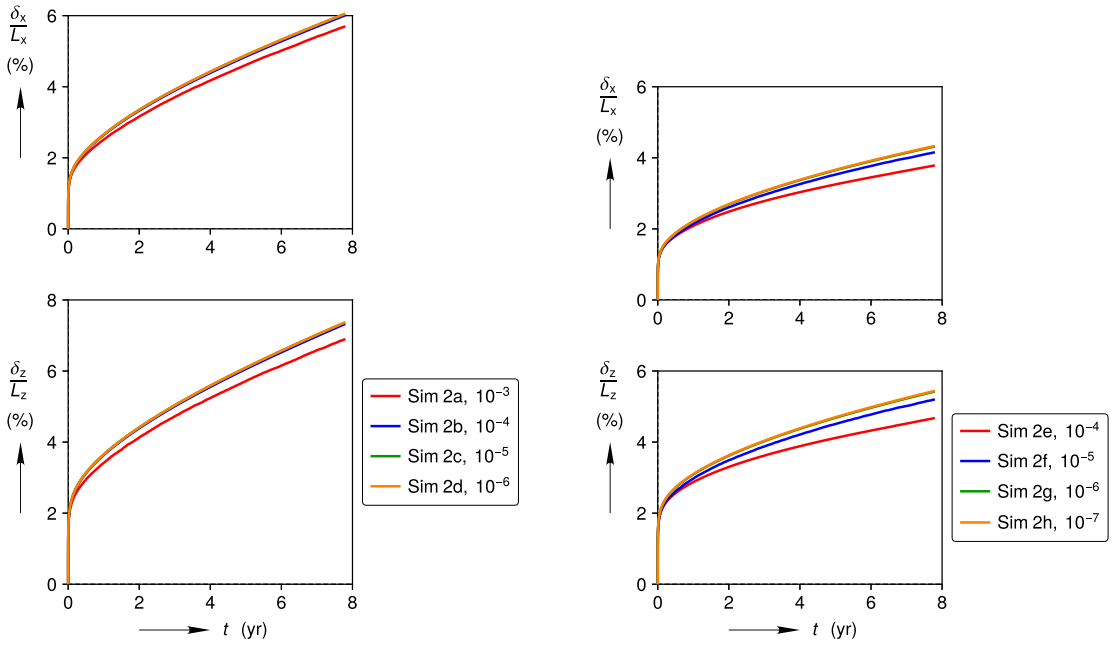
Section 2.2 of Ref. 35 found that changing the contact algorithm and adding the fluid pressure ramp down had negligible effects on the closure curves, while changing the finite element type, finite element mesh, and $\hat{R}_{\max}$ had more substantial impacts.

The second string of improvements involved convergence studies to properly select $\hat{R}_{\max}$, H, and γ. In preparation for the convergence studies, the model setup was made to reflect the setup at the end of Section 3.1. Compared to the recreated legacy simulation (Simulation 1), the anhydrite and polyhalite were added to the stratigraphy; the boundary conditions were changed to those shown in Fig. 18; and clay seams A, B, and M were allowed to slide. The numerical settings used



(a) Legacy mesh (b) New ($L_x/48$, $D \approx 50$ m) mesh

Fig. A.25. Legacy and new finite element meshes of Room D compared. Both meshes use $D \approx 50$ m and stratigraphy 2a (see Table 3b). (The anhydrite and polyhalite layers were included in 2a–2d and 5a–5d, but they were modeled as argillaceous salt in simulations 0, 1, 2, 3, and 4.)



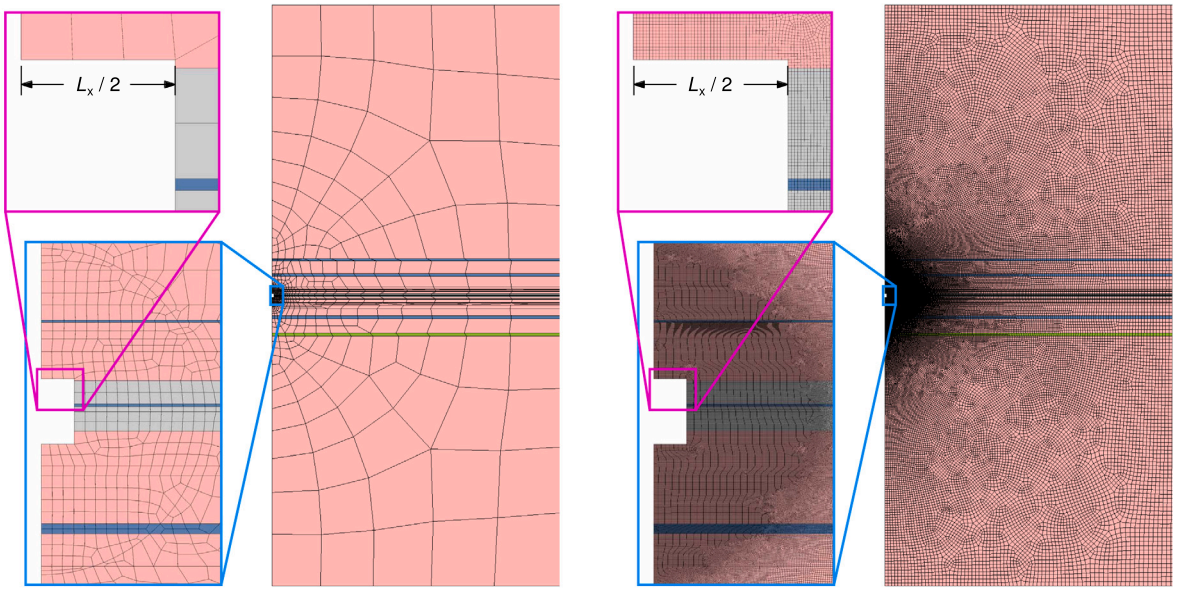
(a) $D \approx 50$ m (b) $D = 400$ m

Fig. A.26. Sensitivity of Room D closure predictions to the relative residual tolerance for two different domain sizes. (For interpretation of the references to color in this figure legend, the reader is referred to the web version of this article.)

in each convergence study simulation (Simulation 2a through 2n) can be found in Table 3a. The single element layer's y thickness was held fixed at 5.5/48 m to avoid affecting $\boldsymbol{F}^{\mathrm{r}}$.

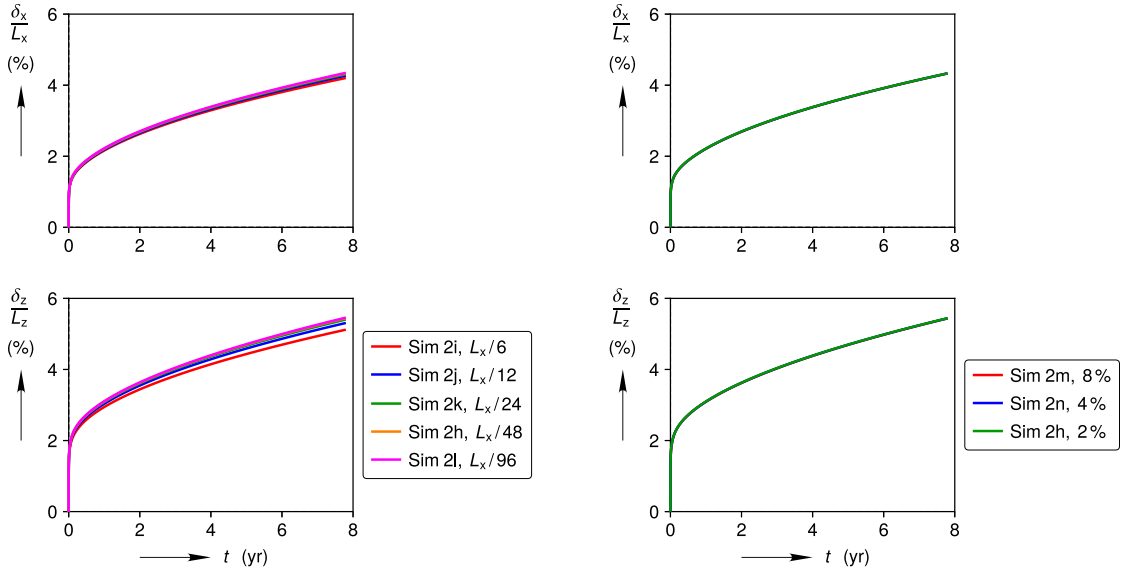
The sensitivity to $\hat{R}_{\max}$ was investigated using a $D \approx 50$ m domain and a $D = 400$ m domain. Two domain sizes were considered because $\sqrt{\boldsymbol{F}^{\mathrm{r}} \cdot \boldsymbol{F}^{\mathrm{r}}}$ in Eq. (A.1) scales with domain size, such that larger domains require a smaller value of $\hat{R}_{\max}$ to maintain the same level of accuracy.

As expected, the closure histories in Fig. A.26 converge and become insensitive to $\hat{R}_{\max}$ as $\hat{R}_{\max}$ is reduced. A value of $\hat{R}_{\max} = 10^{-5}$ was selected for all further $D \approx 50$ m simulations, while $\hat{R}_{\max} = 10^{-7}$ was chosen for further $D = 400$ m simulations. Rather than repeat these convergence studies for intermediate domain sizes, such as $D = 200$ m, the two extremes were linearly interpolated in log–log space according to $\hat{R}_{\max} = 10^{(-5-(7-5)/\log(400/50)\times\log(D/50))}$.



(a) $L_x/6$ mesh (b) $L_x/96$ mesh

Fig. A.27. Coarsest and finest meshes used in the Room D mesh convergence study. Both meshes use $D = 400$ m and stratigraphy 2a (see Table 3b) with argillaceous salt assumed beyond $D \approx 50$ m.



(a) H convergence (b) γ convergence

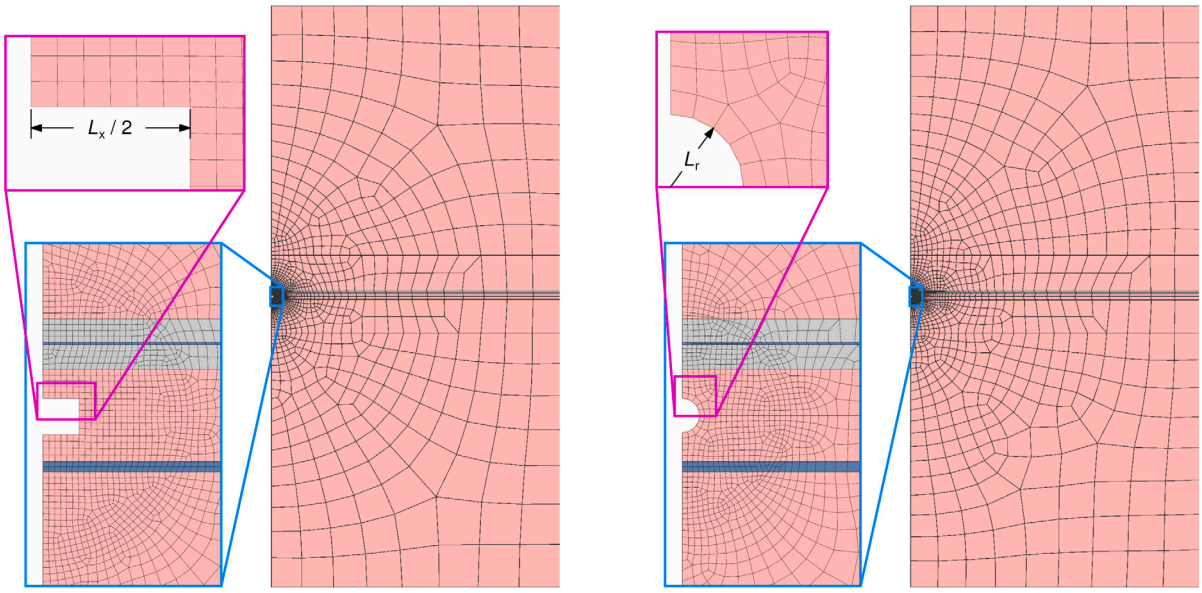
Fig. A.28. Element size convergence (a) and time step growth rate convergence (b) of Room D closure predictions. (For interpretation of the references to color in this figure legend, the reader is referred to the web version of this article.)

The sensitivity to H was studied using the $D = 400$ m domain size. Five meshes were used, ranging from 6 elements across the room width ($H = L_h/6$) to 96 elements across the room width ($H = L_h/96$). The coarsest and finest mesh are displayed in Fig. A.27 and the results of the study are shown in Fig. A.28(a). The closure histories appear to be relatively insensitive to element sizes below $H = L_x/12$, but $H = L_x/48$ was selected for all further Room D simulations to be conservative.

Finally, the sensitivity to the time step growth rate γ was also studied using the $D = 400$ m domain size. The three time step growth rates ($\gamma = 2\%$, 4%, and 8%) produced virtually identical closure histories (see Fig. A.28(b)), but $\gamma = 2\%$ was selected for further simulations because $\gamma = 2\%$ actually gave the shortest simulation run time. Although larger time steps require less steps to reach the end of a simulation, they can also require more constitutive model and global solver iterations.

A.3. Numerical setup for Stone[60] type Room D, G, and Q simulations

Stone[60] type simulations of Room D, G, and Q during the 1990's were not found in the published literature, so the numerical setup for



(a) Room G (b) Room Q

Fig. A.29. Coarse finite element meshes of Rooms G and Q. Both meshes use $D = 400$ m and the Stone[60] stratigraphy with argillaceous salt assumed beyond $D \approx 50$ m.

the Stone[60] type simulations of Room D, G, and Q in this paper (Simulations 19, 20, and 21) was simply designed to be close to the Stone[60] numerical setup. This approximation to Stone's[60] numerical setup used $\hat{R}_{\max} = 10^{-7}$, $\gamma = 2\%$, the AL contact enforcement algorithm, and the room excavation procedure described in Appendix A.2. The Stone[60] type Room G and Q finite element meshes are shown in Fig. A.29. (The Room D mesh was similar so it was omitted for brevity.) These meshes were generated by modifying the Python script for the $D = 400$ m mesh of Room D to reflect the Stone[60] stratigraphy (only MB 139 and anhydrite "a", no clay seams), the Room G and Q cross-sectional geometries, and the Room G and Q locations within the WIPP stratigraphy (see Section 2.2.1). The Room D, G, and Q element sizes near the room were $H = L_x/12$, $H = L_x/12$, and $H = \pi L_r/10$, respectively, which are reasonably similar to the element sizes near the disposal room in Stone[60], Fig. 5. The simulations utilized the MQ element with 0.005 hourglass stiffness to be consistent with Stone.[60]

A.4. Improved numerical setup for Room G and Q simulations

The improved numerical setup for the Room G and Q simulations that utilized the geomechanical model developed herein (Simulation 22 and 23) was quite similar to the improved Room D numerical setup described in Appendix A.2. For example, the setups utilized the same element type, contact formulation, room excavation procedure, $\hat{R}_{\max}$, H, and γ. The finite element meshes (see Fig. A.30) were the only numerical setup difference. These meshes were generated by modifying the Python script for the $D = 200$ m mesh of Room D to reflect the Room G and Q cross-sectional geometries and locations within the WIPP stratigraphy (see Section 2.2.1).

Appendix B. Anhydrite and polyhalite models

This section presents the anhydrite and polyhalite material models. Appendix B.1 describes the model formulation and legacy calibrations, while Appendix B.2 discusses an issue that necessitated a change to the anhydrite model.

B.1. Legacy model formulation

The anhydrite and polyhalite were modeled with a hypoelastic, perfectly plastic, Drucker–Prager model. In this model, the strain rate is decomposed as

$$\dot{\boldsymbol{\epsilon}} = \dot{\boldsymbol{\epsilon}}^{\mathrm{el}} + \dot{\boldsymbol{\epsilon}}^{\mathrm{pl}}, \tag{B.1}$$

where $\dot{\boldsymbol{\epsilon}}^{\mathrm{el}}$ and $\dot{\boldsymbol{\epsilon}}^{\mathrm{pl}}$ represent the elastic and plastic strain rates, respectively. The elastic portion of the model utilizes the same linear elasticity relations as the M–D model, i.e. Eqs. (2) and (3). The plastic portion of the model is meant to implicitly capture microscopic and macroscopic fracturing without explicit fractures. The plastic strain $\boldsymbol{\epsilon}^{\mathrm{pl}}$ evolves when the Drucker–Prager yield function $f = 0$. Let $I_1 = \mathrm{tr}(\boldsymbol{\sigma})$ be the first invariant of the stress tensor $\boldsymbol{\sigma}$, and let $J_2 = \boldsymbol{\sigma}^{\mathrm{dev}} : \boldsymbol{\sigma}^{\mathrm{dev}}/2$ be the second invariant of the deviatoric stress tensor $\boldsymbol{\sigma}^{\mathrm{dev}} = \boldsymbol{\sigma} - I_1/3\,\boldsymbol{I}$. With these definitions, the Drucker–Prager yield function f can be expressed in terms of the material constants A and C as

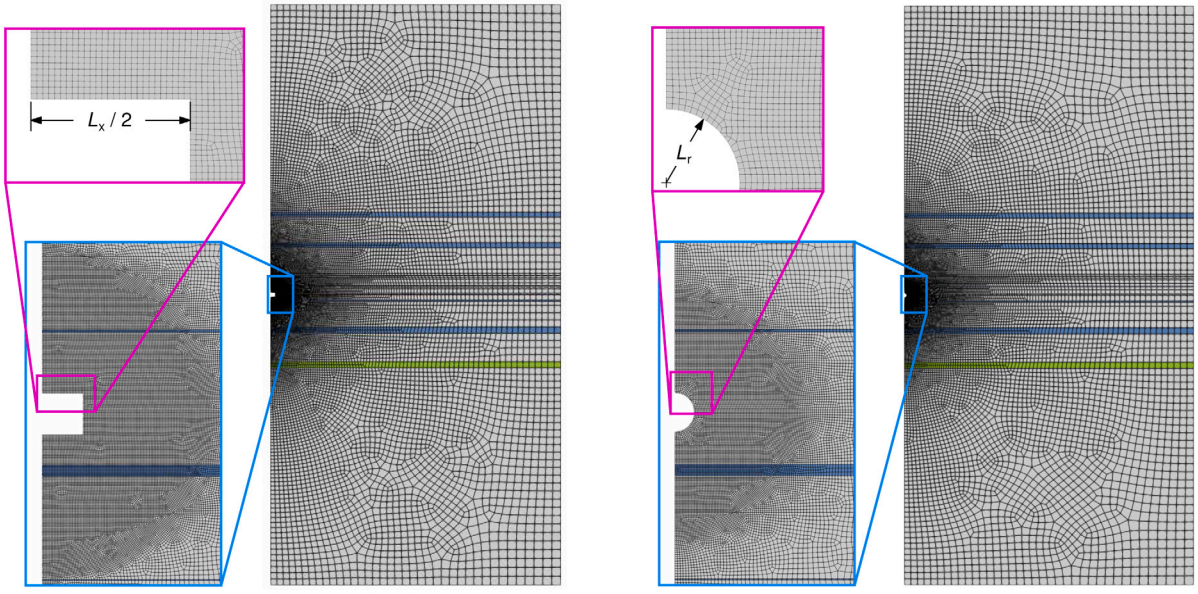
$$f = \sqrt{J_2} - A\,I_1 - C, \tag{B.2}$$

keeping in mind that tensile stresses are negative. Note that this simple yield function does not include a hardening term.

The plastic flow potential determines the ratio of the plastic flow components, in other words, the plastic flow direction. Although many publications (e.g. Refs. 50, 60, 77) utilize this Drucker–Prager model for the anhydrite and polyhalite, none appear to document the plastic flow potential. Fortunately, the SANTOS input file in Appendix A of Ref. 60 shows that the `soils_and_crushable_foams` model was utilized for the anhydrite and polyhalite. According to the SANTOS and LAMÉ manuals,[78,79] the `soils_and_crushable_foams` model uses a non-associative flow rule

$$\dot{\boldsymbol{\epsilon}}^{\mathrm{pl}} = \lambda \frac{\partial b}{\partial \boldsymbol{\sigma}}, \tag{B.3}$$

where λ is the consistency parameter and b is a von Mises flow potential ($b = \sqrt{3\,J_2}$). While the `soils_and_crushable_foams` model does not allow the user to select anything other than a von Mises flow



(a) Room G (b) Room Q

Fig. A.30. Fine finite element meshes of Rooms G and Q. Both meshes use $D = 200$ m and the new stratigraphy in Fig. 18 with salt assumed beyond $D \approx 50$ m.

Table B.4
Anhydrite and polyhalite calibrations.

Parameter	Units	Legacy Anhydrite	Anhydrite Cal 1	Legacy Polyhalite
μ	GPa	27.8	27.8	20.3
B	GPa	83.4	83.4	65.8
A	–	0.45	0.45	0.473
C	MPa	1.35	1.35	1.42
ω	rad	0	0.423	0

potential, the newer `kayenta` model[80] can use a Drucker–Prager yield function and a Drucker–Prager flow potential,

$$b = \sqrt{J_2} - \tan(\omega)\, I_1, \tag{B.4}$$

where ω is the dilation angle that controls the ratio of deviatoric to spherical plastic strain.

The legacy anhydrite and legacy polyhalite calibrations specified in Ref. 50 are listed in Table B.4 for reference. Note that $\omega = 0$ for the legacy calibrations. Table B.4 also includes a new anhydrite calibration discussed in the following subsection.

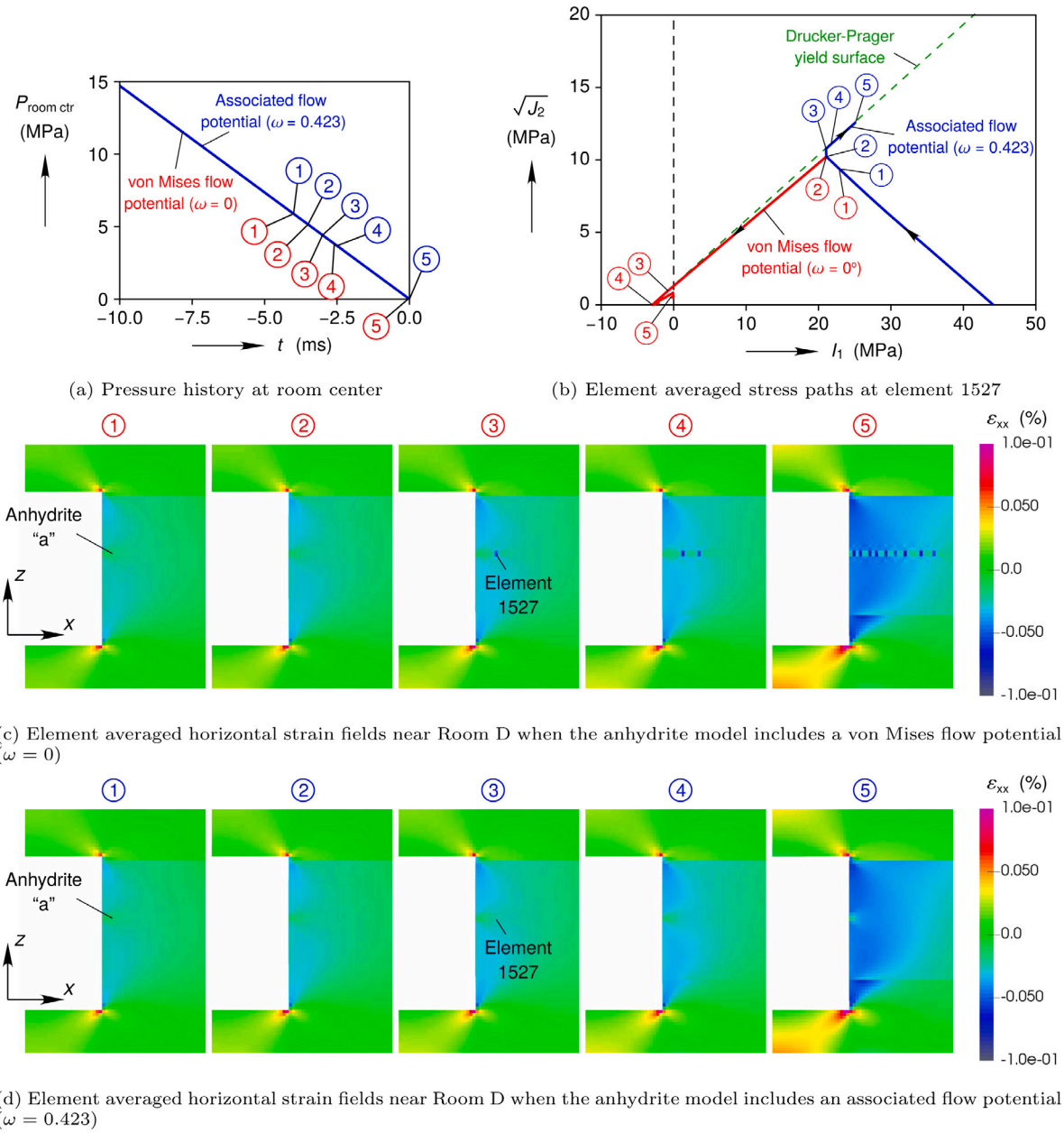
B.2. Anhydrite model issue

Adding the anhydrite strata to the stratigraphy around Room D turned out to be much more difficult than anticipated. Although Sierra/SolidMechanics's[36] conjugate gradient solver had no difficulties when the anhydrite was neglected, including the anhydrite in Simulation 5a made the solver repeatedly fail to converge during the fluid pressure ramp down (see Appendix A.2). Solver settings were adjusted, the time step was reduced, the clay seams were eliminated, the finite element mesh was refined, and hardening was added to the anhydrite model, but the solver continued to struggle. The `kayenta` model was even reduced to the legacy anhydrite model calibration in Appendix B.1, but the `kayenta` model calibration exhibited the exact same behavior. Eventually, the problem was traced back to the von Mises flow potential.

Symptoms of the von Mises flow potential issue are shown in Fig. B.31. The fluid pressure at the center of the room is plotted against time in Fig. B.31(a), and the red circled number instances correspond to the ϵ_{xx} fields near Room D in Fig. B.31(c). Note that the ϵ_{xx} fields are relative to the ϵ_{xx} field corresponding to the original lithostatic stress field at $t = -10$ ms. The faint green layer in Fig. B.31(c) is the problematic anhydrite "a" layer. From the beginning of the fluid pressure ramp down to ②, anhydrite "a" behaves as expected. Between ② and ③, however, a vertical band of high strain in anhydrite "a" appears in a single time step. Another time step produces another localization band to the right of the first one in ④. More localization bands appeared between ④ and ⑤, and the conjugate gradient solver struggled to converge thereafter. In order to understand this behavior further, the stress averaged over element 1527, which is in the first localization band in ③, was plotted in $\sqrt{J_2}$ vs. I_1 space in Fig. B.31(b). Between $t = -10$ ms and ②, element 1527 slowly moves from 44.1 MPa on the I_1 axis to nearly touch the Drucker–Prager yield surface. From ② to ③, the strain localizes in element 1527 and the stress state jumps down almost to the tip of the Drucker–Prager cone in a single time step. Element 1527 remains near the tip of the cone for the rest of the simulation. Similar observations were made with a finer ($H = L_x/96$) mesh in Section 2.2 of Ref. 35, except the strain localizations were sharper and the solver repeatedly failed to converge at $t = -1.7$ ms.

Anhydrite is a brittle material that cannot carry further stress when its strength is exceeded, so the strain localizations shown in Fig. B.31(c) may appear to be fractures, but that is not the case. The model in Appendix B.1 does not model fractures explicitly: the fractures are smeared out and modeled as a continuum. Once a material point reaches the Drucker–Prager yield surface, it is considered fractured and no further stress can develop due to the lack of hardening (perfect plasticity).

Instead of fractures, the strain localizations in Fig. B.31(c) were most likely due to a material model instability. Rudnicki and Rice[81] demonstrated that rate-independent plasticity with a non-associated



(a) Pressure history at room center

(b) Element averaged stress paths at element 1527

(c) Element averaged horizontal strain fields near Room D when the anhydrite model includes a von Mises flow potential ($\omega = 0$)

(d) Element averaged horizontal strain fields near Room D when the anhydrite model includes an associated flow potential ($\omega = 0.423$)

Fig. B.31. Results from Simulation 5a, where the anhydrite model utilized a von Mises flow potential, and Simulation 5d, where the anhydrite model utilized an associated flow potential. Switching to an associated flow potential eliminates the spurious strain localizations in ((c)). (For interpretation of the references to color in this figure legend, the reader is referred to the web version of this article.)

flow rule can suffer from non-uniqueness, which manifests as strain localizations in boundary value problems. To investigate this hypothesis herein, the anhydrite dilatation angle was set to $\omega = \arctan(A) = 0.423$, making the flow rule associative, in Simulation 5d. With an associated flow rule, the strain localizations did not appear (see Fig. B.31(d)) and the conjugate gradient solver had no trouble converging. In addition, the average stress at element 1527 reached the Drucker–Prager yield surface at (3) (see Fig. B.31(b)) and slowly moved up the surface between (3) and (5), instead of jumping down to the tip of the Drucker–Prager cone.

One might ask how did this strain localization issue only appear now? Prior to Argüello and Holland,[14] simulations of Room D only used coarse meshes, which tend to restrain strain localizations. In addition, the fine mesh simulations in Refs. 14, 82 were inspected, and they also exhibited strain localizations in the anhydrite layers. The localizations did not stop the simulations presumably because the maximum allowable relative residual was $\hat{R}_{\max} = 10^{-3}$, instead of 10^{-5}. Therefore, the localizations were probably suppressed by coarse meshes or simply went undetected until now.

Although Morgan and Krieg[50] calibrated A and C against experimental data, it appears the von Mises flow potential in the `soils_and_crushable_foams` model dictated $\omega = 0$ rather than any experimental observations. Microcracking typically causes rocks to macroscopically dilate, so $0 < \omega \leq 0.423$ are reasonable values until the anhydrite model can be improved in the future. To assist in choosing ω, Room D's closure was simulated with $\omega = 0.106$, 0.211, and 0.423

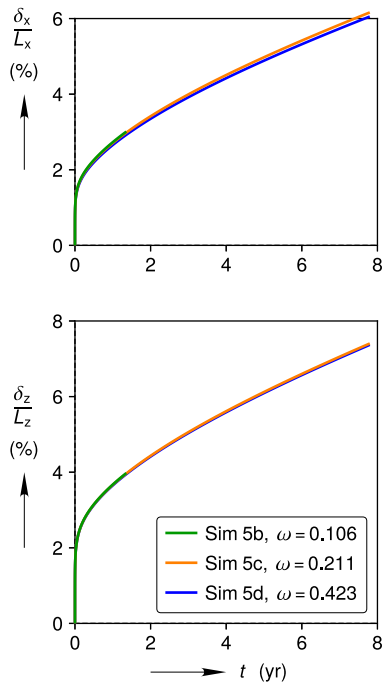


Fig. B.32. Room closure prediction sensitivity to the anhydrite dilatation angle. (For interpretation of the references to color in this figure legend, the reader is referred to the web version of this article.)

(Simulations 5b, 5c, and 5d). Only the simulation with $\omega = 0.423$ did not exhibit strain localizations. As a result, the $\omega = 0.106$ and $\omega = 0.211$ simulations reached $t = 1.36$ yr 27.7× and 3.1× slower, respectively, than the $\omega = 0.423$ simulation. As the room closure appears insensitive to ω in Fig. B.32, $\omega = 0.423$ (an associative flow rule) was chosen for anhydrite Calibration 1, as shown in Table B.4, which was used for all further simulations.

References

1. Morgan HS, Stone CM, Krieg RD. Use of field data to evaluate and improve drift response models for the Waste Isolation Pilot Plant (WIPP). In: *The 26th US Symposium on Rock Mechanics*. USRMS, American Rock Mechanics Association; 1985:769–776.
2. Morgan HS, Stone CM, Krieg RD. *An Evaluation of WIPP Structural Modeling Capabilities Based on Comparisons with South Drift Data*. Technical Report SAND85-0323; Albuquerque, NM, USA; Livermore, CA, USA: Sandia National Laboratories; 1986.
3. Munson DE, Torres T, Blankenship D. Early results from the thermal/structural in situ test series at the WIPP. In: *The 27th US Symposium on Rock Mechanics*. USRMS, American Rock Mechanics Association; 1986:923–930.
4. Munson DE, Fossum AF. Comparison between predicted and measured south drift closures at the WIPP using a transient creep model for salt. In: *The 27th US Symposium on Rock Mechanics*. USRMS, American Rock Mechanics Association; 1986:931–939.
5. Munson DE, Torres TM, Jones RL. Pseudostrain representation of multipass excavations in salt. In: *The 28th US Symposium on Rock Mechanics*. USRMS, American Rock Mechanics Association; 1987:853–862.
6. Munson DE, Fossum AF, Senseny PE. *Advances in Resolution of Discrepancies Between Predicted and Measured in Situ WIPP Room Closures*. Technical Report SAND88-2948; Albuquerque, NM, USA: Sandia National Laboratories; 1989.
7. Munson DE. Constitutive model of creep in rock salt applied to underground room closure. *Int J Rock Mech Min Sci*. 1997;34:233–247.
8. Hampel A, Herchen K, Lux KH, et al. *Verbundprojekt: Vergleich aktueller Stoffgesetze und Vorgehensweisen anhand von Modellberechnungen zum thermo-mechanischen Verhalten und zur Verheilungtoffgesetze anhand von Modellberechnungen zum thermo-mechanischen Verhalten und zur Verheilung von Steinsalz – Synthesebericht*. Technical Report BMBF-FKZ 02E10810; Projektträger Karlsruhe, Wassertechnologie und Entsorgung (PTKA-WTE), Karlsruher Institut für Technologie (KIT); 2016. http://dx.doi.org/10.2314/GBV:88655800X.
9. Ofoegbu G, Dasgupta B. *Implementation of a Creep Model in FLAC to Study the Thermomechanical Response of Salt as a Host Repository Medium–Progress Report*. Technical Report Contract No. NRC–HQ–12–C–02–0089; San Antonio: Southwest Research Institute, Center for Nuclear Waste Regulatory Analyses; 2016.
10. Ofoegbu G, Dasgupta B. *Implementation of a Creep Model in FLAC to Study the Thermomechanical Response of Salt as a Host Repository Medium–2nd Progress Report*. Technical Report Contract No. NRC–HQ–12–C–02–0089; San Antonio: Southwest Research Institute, Center for Nuclear Waste Regulatory Analyses; 2017.
11. Ofoegbu G, Dasgupta B. *Implementation of a Creep Model in FLAC to Study the Thermomechanical Response of Salt as a Host Repository Medium–3rd Progress Report*. Technical Report Contract No. NRC–HQ–12–C–02–0089; San Antonio: Southwest Research Institute, Center for Nuclear Waste Regulatory Analyses; 2018.
12. Hampel A, Günther RM, Salzer K, et al. Joint project III on the comparison of constitutive models for the mechanical behavior of rock salt: Modeling of the temperature influence on deformation at WIPP. In: Fahland S, Hammer J, Hansen FD, Heusermann S, Lux KH, Minkley WM, eds. *The Mechanical Behavior of Salt IX, BGR*. Federal Institute for Geosciences and Natural Resources; 2018:427–446.
13. Rath JS, Argüello JG. *Revisiting Historical Numerical Analyses of the Waste Isolation Pilot Plant (WIPP) Room B and D in-Situ Experiments Regarding Thermal and Structural Response*. Technical Report SAND2012-7525; Albuquerque, NM, USA: Sandia National Laboratories; 2012.
14. Argüello JG, Holland JF. Two problems to benchmark numerical codes for use in potential HLW salt repositories. In: Roberts L, Mellegard K, Hansen FD, eds. *Proc. 8th Conference on the Mechanical Behavior of Salt*. 2015:361–371.
15. Pudewills A. Modeling of hydro-mechanical behavior of rock salt in the near field of repository excavations. In: Lux KH, Minkley W, Wallner M, Hardy R, eds. *Basic and Applied Salt Mechanics*. 2007:195–200. Proc. of the Sixth Conf. on the Mech. Behavior of Salt.
16. Mellegard KD, Munson DE. *Laboratory Creep and Mechanical Tests on Salt Data Report (1975-1996)*. Technical Report SAND96-2765; Albuquerque, NM, USA: Sandia National Laboratories; 1997.
17. Chan KS, Bodner SR, Munson DE. Permeability of WIPP salt during damage evolution and healing. *Int J Damage Mech*. 2001;10:347–375.
18. Butcher BM, Mendenhall F. *A Summary of the Models Used for the Mechanical Response of Disposal Rooms in the Waste Isolation Pilot Plant with Regard to Compliance with 40 CFR 191, Subpart B*. Technical Report SAND92-0427; Albuquerque, NM, USA: Sandia National Laboratories; 1993.
19. Labreche DA, Beikmann M, Osnes J, Butcher B. *A Sensitivity Analysis of the WIPP Disposal Room Model: Phase 1*. Technical Report SAND94-0890; Albuquerque, NM, USA: Sandia National Labs; 1995.
20. Butcher BM. *A Summary of the Sources of Input Parameter Values for the Waste Isolation Pilot Plant Final Porosity Surface Calculations*. Technical Report SAND97-0796; Albuquerque, NM, USA: Sandia National Laboratories; 1997.
21. Munson DE, Dawson P. *Constitutive Model for the Low Temperature Creep of Salt (with Application to WIPP)*. Technical Report SAND79-1853; Albuquerque, NM, USA: Sandia National Laboratories; 1979.
22. Munson DE, Dawson P. *Transient Creep Model for Salt During Stress Loading and Unloading*. Technical Report SAND82-0962; Albuquerque, NM, USA: Sandia National Laboratories; 1982.
23. Reedlunn B. *Enhancements to the Munson-Dawson Model for Rock Salt*. Technical Report SAND2018-12601; Albuquerque, NM, USA: Sandia National Laboratories; 2018. http://dx.doi.org/10.2172/1481508.
24. Hosford W. A generalized isotropic yield criterion. *J Appl Mech*. 1972;39:607–609.
25. Scherzinger WM. A return mapping algorithm for isotropic and anisotropic plasticity models using a line search method. *Comput Methods Appl Mech Engrg*. 2017;317:526–553.
26. Salzer K, Günther RM, Minkley W, et al. Joint Project III on the comparison of constitutive models for the thermomechanical behavior of rock salt. II. Extensive laboratory test program with clean salt from WIPP. In: Roberts L, Mellegard KD, Hansen FD, eds. *Proc. 8th Conference on the Mechanical Behavior of Salt*. 2015:3–12.
27. Düsterloh U, Herchen K, Lux KH, et al. Joint Project III on the comparison of constitutive models for the thermomechanical behavior of rock salt. III. Extensive laboratory test program with argillaceous salt from WIPP and comparison of test results. In: Roberts L, Mellegard KD, Hansen FD, eds. *Proc. 8th Conference on the Mechanical Behavior of Salt*. 2015:13–21.
28. Günther RM, Lüdeling C, Popp T, Naumann D, Wiedemann M, Weise D. *Verbundprojekt: Vergleich aktueller stoffgesetze und Vorgehensweisen anhand von Modellberechnungen zum thermo-mechanischen Verhalten und zur Verheilung von Steinsalz; Teilvorhaben 2*. Technical Report FZK(02E10830); Leipzig, Deutschland: Institute für Gebirgsmechanik GmbH; 2016. http://dx.doi.org/10.2314/GBV:886619653.
29. Peach C, Spiers C, Trimby P. Effect of confining pressure on dilatation, recrystallization, and flow of rock salt at 150 °C. *J Geophys Res Solid Earth*. 2001;106:13315–13328.
30. Ter Heege J, De Bresser J, Spiers C. Rheological behaviour of synthetic rocksalt: The interplay between water, dynamic recrystallization and deformation mechanisms. *J Struct Geol*. 2005;27:948–963.
31. Ter Heege Jd, De Bresser J, Spiers C. Dynamic recrystallization of wet synthetic polycrystalline halite: Dependence of grain size distribution on flow stress, temperature and strain. *Tectonophysics*. 2005;396:35–57.

32. Urai J, Schléder Z, Spiers C, Kukla P. *Dynamics of Complex Intracontinental Basins: The Central European Basin System*. Berlin, Heidelberg: Springer-Verlag; 2008. 277–290. Chapter 5.2: Flow and transport properties of salt rocks.
33. Bérest P, Gharbi H, Brouard B, Brückner D, DeVries K, Hévin G, Hofer G, Spiers C, Urai J. Very slow creep tests on salt samples. *Rock Mech Rock Eng*. 2019;52:2917–2934. http://dx.doi.org/10.1007/s00603-019-01778-9.
34. Hansen FD. Micromechanics of isochoric salt deformation. In: *48th US Rock Mechanics/Geomechanics Symposium*. American Rock Mechanics Association; 2014.
35. Reedlunn B. *Reinvestigation Into Closure Predictions of Room D At the Waste Isolation Pilot Plant*. Technical Report SAND2016-9961; Albuquerque, NM, USA: Sandia National Laboratories; 2016. http://dx.doi.org/10.2172/1333709.
36. Sierra/SolidMechanics. *Sierra/SolidMechanics User's Guide*. 4.50.2 ed. Albuquerque, NM, USA; Livermore, CA, USA: Sandia National Laboratories; 2018.
37. Morgan H, Stone C. *Pretest Reference Calculation for the 6.1 Meter (20 Ft) Wide Drifts of the Geomechanical Evaluation (WIPP Room G in Situ Experiment)*. Technical Report SAND85-0893; Albuquerque, NM, USA; Livermore, CA, USA: Sandia National Laboratories; 1985.
38. Jensen A, Jones R, Lorusso E, Howard C. *Large-Scale Brine Inflow Data Report for Room Q Prior to November 25, 1991*. Technical Report SAND92-1173; Albuquerque, NM, USA: Sandia National Laboratories; 1993.
39. Carrasco R. Cutting head radius for room B and room D corners. 2015. Personal Communication.
40. Munson DE, Matalucci R, Hoag D, Blankenship D. *Construction of the Thermal/Structural Interactions in Situ Tests At the Waste Isolation Pilot Plant (WIPP)*. Technical Report SAND87-2685; Albuquerque, NM, USA; Livermore, CA, USA: Sandia National Laboratories; 1987.
41. Krieg RD. *Reference Stratigraphy and Rock Properties for the Waste Isolation Pilot Plant (WIPP) Project*. Technical Report SAND83-1908; Albuquerque, NM, USA: Sandia National Laboratories; 1984.
42. Reedlunn B, Williams LA. *Reconstruction of the Waste Isolation Pilot Plant Room D, B, G, and Q Closure Histories*. Technical Report SAND2021-6904; Albuquerque, NM, USA: Sandia National Laboratories; 2021.
43. Munson DE, Jones R, Hoag D, Ball J. *Mining Development Test (Room D): In Situ Data Report (March 1984-May 1988): Waste Isolation Pilot Plant (WIPP) Thermal/Structural Interactions Program*. Technical Report SAND88-1460; Albuquerque, NM, USA; Livermore, CA, USA: Sandia National Laboratories; 1988.
44. Munson DE, Jones R, Ball J, Clancy R, Hoag D, Petney S. *Overtest for Simulated Defense High-Level Waste (Room B): In Situ Data Report (May 1984-February 1988). Waste Isolation Pilot Plant (WIPP) Thermal/Structural Interactions Program*. Technical Report SAND89-2671; Albuquerque, NM, USA; Livermore, CA, USA: Sandia National Laboratories; 1990.
45. Munson DE, Jones RL, Northrop-Salazar CL, Woerner S. *Multipass Mining Sequence Room Closures: In Situ Data Report. Waste Isolation Pilot Plant (WIPP) Thermal/Structural Interactions Program*. Technical Report SAND87-2687; Albuquerque, NM, USA; Livermore, CA, USA: Sandia National Laboratories; 1992.
46. Munson DE, Petney SV, Christian-Frear TL, Ball JR, Jones RL, Northrop-Salazar CL. *Geomechanical Evaluation (Room G): In Situ Data Report (December 1984 - November 1990) Waste Isolation Pilot Plant (WIPP) Thermal/Structural Interactions Program*. Technical Report SAND92-0582; Albuquerque, NM, USA: Sandia National Laboratories; 1992.
47. Jensen A, Howard C, Chester C, Bower R. *Large-Scale Brine Inflow Data Report for Room Q: November 25, 1991 Through July 6, 1995*. Technical Report SAND94-1393 (Copy of 5/14/96 draft on file in the Sandia WIPP archives as WPO 37958) (ERMS237958); Albuquerque, NM, USA: Sandia National Laboratories; 1996.
48. Chavez M. Los Medanos and B-49 WIPP media. 2009. Memorandum.
49. Duran G. Destroyed digital records of room closure. 2021. Personal Communication.
50. Morgan HS, Krieg RD. Updated Drucker-Prager constants for anhydrite and polyhalite. 1984. Memorandum.
51. Stone CM, Krieg RD, Beisinger Z. *SANCHO - a Finite Element Computer Program for the Quasistatic, Large Deformation, Inelastic Response of Two-Dimensional Solids*. Technical Report SAND84-2618; Albuquerque, NM, USA: Sandia National Laboratories; 1985.
52. Mellegard KD, Callahan GD, Senseny PE. *Multiaxial Creep of Natural Rock Salt*. Technical Report SAND91-7083; Albuquerque, NM, USA: Sandia National Laboratories; 1992. RE/SPEC, Inc. Rapid City, SD, USA.
53. Senseny PE. *Triaxial Compression Creep Tests on Salt from the Waste Isolation Pilot Plant*. Technical Report SAND85-7261; Albuquerque, NM, USA; Livermore, CA, USA: Sandia National Laboratories; 1986.
54. Senseny PE. *Creep of Salt from the ERDA-9 Borehole and the WIPP Workings*. Technical Report SAND89-7098; Albuquerque, NM, USA; Livermore, CA, USA: Sandia National Laboratories; 1990.
55. Munson DE, DeVries KL. Progress in validation of structural codes for radioactive waste repository applications in bedded salt. In: *Proc. GEOVAL-90 Symposium on Validation of Geosphere Flow and Transport Models*. 1990:16–23.
56. Callahan GD, Fossum AF, Svalsta DK. *Documentation of SPECTROM-32: A Finite Element Thermomechanical Stress Analysis Program*. Rapid City, SD: RE/SPEC; 1986.
57. Munson DE, DeVries KL, Callahan GD. Comparison of calculations and in situ results for a large, heated, test room at the Waste Isolation Pilot Plant (WIPP). In: *The 31st U.S. Symposium on Rock Mechanics*. USRMS, American Rock Mechanics Association; 1990:389–396.
58. Munson DE, Jones RL, DeVries KL. Analysis of early creep closures in geomechanically connected underground rooms in salt. In: *The 32nd US Symposium on Rock Mechanics*. USRMS, American Rock Mechanics Association; 1991:881–888.
59. Munson DE, Weatherby J. Two- and three-dimensional calculations of scaled in situ tests using the M-D model of salt creep. In: *The 34th US Symposium on Rock Mechanics*. USRMS, American Rock Mechanics Association; 1993:507–510.
60. Stone CM. *Final Disposal Room Structural Response Calculations*. Technical Report SAND97-0795; Albuquerque, NM, USA; Livermore, CA, USA: Sandia National Laboratories; 1997.
61. Argüello JG, Munson DE, Preece DS. Preliminary results of the three-dimensional modeling of the WIPP Room D excavation sequence. In: *The 28th US Symposium on Rock Mechanics*. American Rock Mechanics Association; 1987:863–872.
62. Morgan HS, Wallner M, Munson DE. *Results of an International Parallel Calculations Exercise Comparing Creep Responses Predicted with Three Computer Codes for Two Excavations in Rock Salt*. Technical Report SAND87-2125; Albuquerque, NM, USA; Livermore, CA, USA: Sandia National Laboratories; 1987.
63. Deal DE, Abitz RJ, Case JB, et al. *Brine Sampling and Evaluation Program: 1988 Report*. Technical Report DOE-WIPP-89-015; Carlsbad, NM, USA: Westinghouse Electric Corp.; 1989. Waste Isolation Div.
64. Schuhen M. Origin of 2013 cores. 2016. Personal Communication.
65. Powers DW. *Reference Stratigraphy Applied to Rock Mechanics Studies for the Waste Isolation Pilot Plant: A Review-January 11, 2017*. Technical Report ERMS567705; Consulting Geologist; 2017.
66. Herchen K, Düsterloh U, Lux KH. *Verbundprojekt: Vergleich aktueller Stoffgesetze und Vorgehensweisen anhand von Modellberechnungen zum thermo-mechanischen Verhalten und zur Verheilungtoffgesetze anhand von Modellberechnungen zum thermo-mechanischen Verhalten und zur Verheilung von Steinsalz (TV 5: TUC)*. Technical Report BMBF-FKZ 02E10820; Projektträger Karlsruhe, Wassertechnologie und Entsorgung (PTKA-WTE), Karlsruher Institut für Technologie (KIT); 2016. http://dx.doi.org/10.2314/GBV:87169817X.
67. Naumann D. Grain size of IfG creep specimens from 2013 WIPP cores. 2021. Personal Communication.
68. Günther RM, Salzer K, Popp T, Lüdeling C. Steady-state creep of rock salt: Improved approaches for lab determination and modelling. *Rock Mech Rock Eng*. 2015;48:2603–2613.
69. Salzer K. Axial compliance of institut für gebirgsmechanik creep testing rigs. 2017. Personal Communication.
70. Nelder JA, Mead R. A simplex method for function minimization. *Comput J*. 1965;7:308–313.
71. Virtanen P, Gommers R, Oliphant TE, et al. SciPy 1.0: Fundamental algorithms for scientific computing in Python. *Nature Methods*. 2020;17:261–272. http://dx.doi.org/10.1038/s41592-019-0686-2.
72. Joseph DD. *Fluid Dynamics of Viscoelastic Liquids; vol. 84*. Springer Science & Business Media; 2013.
73. Jones CL. *Geologic Data for Borehole ERDA-9, Eddy County, New Mexico*. Technical Report 81-469; United States Geological Survey; 1981.
74. Holt RM, Powers D. *Geologic Mapping of the Air Intake Shaft At the Waste Isolation Pilot Plant*. Technical Report DOE/WIPP 90-051; Carlsbad, NM, United States: Westinghouse Electric Corp.; 1990. Engineering and Repository Technology Dept.
75. Morgan HS, Stone CM. *Pretest Reference Calculation for the Overtest for Simulated Defense High Level Waste (WIPP Room B in Situ Experiment)*. Technical Report SAND85-0213; Albuquerque, NM, USA; Livermore, CA, USA: Sandia National Laboratories; 1985.
76. CUBIT Team. *CUBIT Mesh Generation Environment Users Manual*. 15.0 ed. Albuquerque, NM, USA; Livermore, CA, USA: Sandia National Laboratories; 2015.
77. Munson DE, Morgan H. *Methodology for Performing Parallel Design Calculations (Nuclear Waste Repository Application)*. Technical Report SAND85-0324; Albuquerque, NM, USA: Sandia National Laboratories; 1986.
78. Stone CM. *SANTOS: A Two-Dimensional Finite Element Program for the Quasistatic, Large Deformation, Inelastic Response of Solids*. Technical Report SAND90-0543; Albuquerque, NM, USA; Livermore, CA, USA: Sandia National Laboratories; 1997.
79. Scherzinger WM, Lester BT. *Library of Advanced Materials for Engineering (LAME) 4.48*. Technical Report SAND2018-3231; Albuquerque, NM, USA; Livermore, CA, USA: Sandia National Laboratories; 2018.
80. Brannon RM, Fuller TJ, Fossum AF, Strack OE. *Kayenta: Theory and User's Guide*. Technical Report SAND2015-0803; Albuquerque, NM, USA; Livermore, CA, USA: Sandia National Laboratories; 2015.
81. Rudnicki JW, Rice J. Conditions for the localization of deformation in pressure-sensitive dilatant materials. *J Mech Phys Solids*. 1975;23:371–394.
82. Argüello JG. *Summary of FY15 Results of Benchmark Modeling Activities*. Technical Report SAND2015-6273; Albuquerque, NM, USA: Sandia National Laboratories; 2015.